

# UC Berkeley

## UC Berkeley Electronic Theses and Dissertations

### Title

New Frontiers for Physics Beyond the Standard Model

### Permalink

<https://escholarship.org/uc/item/5hh3g469>

### Author

Narayan, Vijay

### Publication Date

2020

Peer reviewed|Thesis/dissertation

New Frontiers for Physics Beyond the Standard Model

by

Vijay Narayan

A dissertation submitted in partial satisfaction of the

requirements for the degree of

Doctor of Philosophy

in

Physics

in the

Graduate Division

of the

University of California, Berkeley

Committee in charge:

Professor Surjeet Rajendran, Co-chair

Professor Lawrence J. Hall, Co-chair

Professor Yasunori Nomura

Professor Karl van Bibber

Spring 2020

New Frontiers for Physics Beyond the Standard Model

Copyright 2020  
by  
Vijay Narayan

## Abstract

New Frontiers for Physics Beyond the Standard Model

by

Vijay Narayan

Doctor of Philosophy in Physics

University of California, Berkeley

Professor Surjeet Rajendran, Co-chair

Professor Lawrence J. Hall, Co-chair

We present three distinct pathways for theory and experiment beyond the Standard Model. First, we propose an experimental design of a laboratory search for axions based on photon regeneration with superconducting RF cavities. We then study a novel production mechanism for ultralight vector dark matter in the early universe based on a parametric resonance instability. Finally, we show that white dwarfs are in fact ideal “detectors” of ultra-heavy DM over large regions of parameter space.

# Contents

|   |           |
|---|-----------|
| <b>Contents</b>   | <b>i</b>  |
| <b>1 Preface</b>  | <b>1</b>  |
| <b>2 Axion Production and Detection with Superconducting RF Cavities</b>  | <b>3</b>  |
| 2.1 Introduction . . . . .  | 3         |
| 2.2 Conceptual Overview . . . . .   | 4         |
| 2.3 Determining the Axion Signal . . . . .                                | 6         |
| 2.4 Sensitivity to Axion-Photon Coupling . . . . .                        | 13        |
| 2.5 Discussion . . . . .  | 15        |
| <b>3 Parametric Resonance Production of Ultralight Vector Dark Matter</b> | <b>17</b> |
| 3.1 Introduction . . . . .  | 17        |
| 3.2 The Model . . . . .   | 19        |
| 3.3 Parametric Resonance . . . . .  | 21        |
| 3.4 Vector Dark Matter from Parametric Resonance . . . . .                | 28        |
| 3.5 Phenomenology . . . . .   | 32        |
| 3.6 Discussion . . . . .  | 34        |
| <b>4 White Dwarfs as Dark Matter Detectors</b>                            | <b>36</b> |
| 4.1 Introduction . . . . .  | 36        |
| 4.2 White Dwarf Runaway Fusion . . . . .                                  | 38        |
| 4.3 Particle Heating of White Dwarfs . . . . .                            | 39        |
| 4.4 Dark Matter-Induced Ignition . . . . .                                | 46        |
| 4.5 Dark Matter Constraints . . . . .                                     | 50        |
| 4.6 Q-balls . . . . .   | 55        |
| 4.7 Discussion . . . . .  | 59        |
| <b>5 Type Ia Supernovae from Dark Matter Core Collapse</b>                | <b>61</b> |
| 5.1 Introduction . . . . .  | 61        |
| 5.2 Triggering thermonuclear runaway . . . . .                            | 62        |
| 5.3 Dark matter core collapse . . . . .                                   | 63        |

|   |                                       |            |
|---|---------------------------------------|------------|
| 5.4   | Black hole-induced SN . . . . .       | 75         |
| 5.5   | Annihilation-induced SN . . . . .     | 80         |
| 5.6   | Discussion . . . . .                  | 83         |
| <b>Bibliography</b>                           |                                       | <b>86</b>  |
| <b>A Estimate of the Axion-induced Fields</b> |                                       | <b>101</b> |
| <b>B A Toy Model for Screening</b>            |                                       | <b>103</b> |
| <b>C Dark Higgs Thermalization</b>            |                                       | <b>107</b> |
| <b>D Particle Stopping in a White Dwarf</b>   |                                       | <b>110</b> |
| D.1   | WD Medium . . . . .                   | 110        |
| D.2   | Nuclear Interactions . . . . .        | 110        |
| D.3   | Radiative Processes . . . . .         | 112        |
| D.4   | Elastic EM Scattering . . . . .       | 113        |
| <b>E Dark Matter Capture</b>                  |                                       | <b>117</b> |
| E.1   | Capture Rate . . . . .                | 117        |
| E.2   | Thermalization and Collapse . . . . . | 119        |

## Acknowledgments

First and foremost, I thank Surjeet Rajendran for his incredible support and candid advice during my time in graduate school. I am particularly grateful for the freedom he gave me (or “benign neglect”) to develop ideas and figure things out on my own. His perspective and style for research is something that I greatly admire and hope to carry forward in some capacity in my future endeavors. I would also like to thank Dan McKinsey, Karl van Bibber, Lawrence Hall, and Yasunori Nomura for serving on my qual and thesis committees.

Physics is a team sport: you don’t do it by yourself. I owe a tremendous debt to my other collaborators Peter Graham, Ryan Janish, Paul Riggins, Jeff Dror, and Keisuke Harigaya. I must thank Paul and Ryan for putting up with my many antics and for the countless hours spent stumbling, growing, and laughing together. Much of the work in this thesis was a product of our shared struggle and understanding. Jeff and Keisuke were my postdoc collaborators and have been like second advisors to me. I learned a tremendous amount from their expertise, and I thank them for their insights and encouragement.

Berkeley is home to many great physicists, and I have benefited tremendously from classes, interactions, and discussions with Hitoshi Murayama, Yasunori Nomura, Lawrence Hall, Kathryn Zurek, Raphael Bousso, Christian Bauer, Marjorie Shapiro, Simon Knapen, Tongyan Lin, Tom Melia, Tim Lou, Dorota Grabowska, Filip Kos, Harikrishnan Ramani, Michael Fedderke, Grant Remmen, Ning Bao, Anders Andreassen, Nicholas Rodd, and Zhengkang Zhang. I additionally thank my fellow grad students who have provided a wonderful sense of camaraderie in the department (and football field), ultimately making my stay in grad school all the more memorable: Raymond Co, Robert McGehee, Jacob Leedom, Katelin Schutz, Chien-I Chiang, Adam Levine, Jihwan Oh, Illan Halpern, Haoyu Sun, Fabio Sanches, Tanner Trickle, David Dunskey, Chi Chi An, Nico Salzetta, Emma Dowd, and Vetri Velan. Among my friends, I especially thank Jacob Leedom and David Dunskey (a.k.a. the CHAMP) for some unforgettable times discussing physics, life, and how best to close a door. Of course, I give my sincerest thanks to Anne Takizawa, Donna Sakima, Joelle Miles, and LaVern Navarro for all their help and support throughout the years. You truly make the physics community at Berkeley a special place.

Finally, words cannot express my gratitude and appreciation for my family and home away from home in the Bay Area.

# Chapter 1

## Preface

While the standard models (SM) of particle physics and cosmology provide our most complete understanding of the Universe, they leave basic questions unanswered. Most conspicuously, dark matter (DM) accounts for 85% of the observed matter density but its identity is unknown. In addition, several hints such as grand unification, UV sensitivity of the Higgs mass, the strong CP problem, and features in the CMB spectrum strongly suggest the existence of new physics. Although rich extensions of the SM have been proposed to address these problems, their resolutions are uncertain and the possibilities innumerable. For instance, the mass of DM can viably span over 80 orders of magnitude while any non-gravitational interactions of DM have yet to be determined. In light of this, it is crucial to cast a wide net in the search for new physics. It is fruitful to consider the pairing of well-motivated possibilities with the relevant tools capable of detecting them, from rapidly developing precision sensors to observations of astrophysical systems. It is also important to identify novel interpretations of existing searches as well as potential signatures not currently being looked for. This thesis focuses on the connections between plausible theoretical models and emerging experimental avenues beyond the SM, and first appeared as published works in [1, 2, 3, 4].

Physics in the far UV can generally lead to new light degrees of freedom. Axions are particularly interesting as they are naturally ultra-light and have suppressed interactions with the visible sector, perhaps solving puzzles in the SM. One way to produce and detect axions is through their electromagnetic coupling: Light Shining Through Walls (LSW) experiments make use of coherent axion-photon conversion in a static magnetic field to convert photons into axions that can traverse an optical barrier and then convert back into photons. In Chapter 2, we propose a novel design of a laboratory search for axions based on photon regeneration with superconducting RF cavities. Our particular setup uses a toroid as a region of confined static magnetic field, while production and detection cavities are positioned in regions of vanishing external field. This permits cavity operation at quality factors of  $Q \sim 10^{10} - 10^{12}$ . The limitations due to fundamental issues such as signal screening and back-reaction are discussed, and the optimal sensitivity is calculated. This experimental design can potentially probe axion-photon couplings beyond astrophysical limits, comparable and complementary to next generation optical experiments.



Recently there has been a plethora of proposals to look for ultra-light DM models using precision metrology including magnetometry, LC circuits, and atomic interferometry. These experiments are sensitive to both (pseudo)scalar and vector DM models. In general, ultra-light DM generally requires a non-thermal origin to achieve the observed density, while still behaving like a pressureless fluid at late times. In Chapter 3, we show that such a production mechanism naturally occurs for vectors whose mass originates from a dark Higgs. If the dark Higgs has a large field value after inflation, the energy in the Higgs field can be efficiently transferred to vectors through parametric resonance. Computing the resulting abundance and spectra requires careful treatment of the transverse and longitudinal components. We study these equations of motion in detail and find that the mass of the vector may be as low as  $10^{-18}$  eV, while making up the dominant DM abundance. This opens up a wide mass range of vector DM as cosmologically viable, further motivating their experimental search.

While substantial progress has been made to detect DM at or below the weak scale, the challenge in directly detecting heavy DM is its diminished number density. Thus for ultra-heavy DM, indirect signatures in astrophysical systems are a natural way forward. One such signal is that DM can trigger runaway fusion and ignite type Ia supernovae in sub-Chandrasekhar white dwarfs. In Chapter 4, we consider DM candidates that heat through the production of high-energy standard model (SM) particles, and show that such particles will efficiently thermalize the white dwarf medium and ignite supernovae. Based on the existence of long-lived white dwarfs and the observed supernovae rate, we derive new constraints on ultra-heavy DM which produce SM particles through DM-DM annihilations, DM decays, and DM-SM scattering interactions in the stellar medium. As a concrete example, we rule out supersymmetric Q-ball DM in parameter space complementary to terrestrial bounds. In Chapter 5, we further examine the ignition of supernovae by the formation and self-gravitational collapse of a DM core containing many DM particles. For non-annihilating DM, such a core collapse may lead to a mini black hole that can ignite supernovae through the emission of Hawking radiation, or possibly as a by-product of accretion. For annihilating DM, core collapse leads to an increasing annihilation rate and can ignite supernovae through a large number of rapid annihilations. These processes extend the previously derived constraints on DM to masses as low as  $10^5$  GeV. Finally, it is intriguing that the DM-induced ignition discussed in this work provide an alternative mechanism of triggering supernovae from sub-Chandrasekhar, non-binary progenitors.

## Chapter 2

# Axion Production and Detection with Superconducting RF Cavities

### 2.1 Introduction

Axions are well-motivated additions to the standard model (SM). They provide an elegant solution to the strong CP problem [5, 6, 7, 8], are a natural dark matter candidate [9, 10, 11], can relax naturalness problems [12, 13], and appear generically in theories of quantum gravity [14, 15]. Purely laboratory searches for axions are thus an important experimental front. Given that axions can naturally be very light and have suppressed interactions with the SM, a promising approach is to search for the coherent interaction of a classical axion field with electromagnetic (EM) fields [16].

Photon regeneration, or “Light Shining Through Walls” (LSW), experiments make use of axion-photon oscillations in a transverse magnetic field to convert photons into axions that can traverse an optical barrier and then convert back into detectable photons [17]. Small axion-photon conversion probabilities are overcome by the use of resonators to sustain large EM fields [18]. This is the basis of experiments such as the Any Light Particle Search (ALPS) [19, 20, 21], which employ optical cavities aligned with dipole magnets over a long baseline. LSW can also be done at radio frequencies (RF) [22, 23, 24], as in the CERN Resonant Weakly Interacting sub-eV Particle Search (CROWS) [25], by producing and detecting the axion through excited modes in matched RF cavities subject to an external magnetic field. While interesting, current constraints from LSW experiments are less stringent than those due to stellar cooling or searches for solar axions (see [26] for a review).

We propose a novel design for an axion LSW experiment using high- $Q$  superconducting RF (SRF) cavities, which can in principle reach beyond these astrophysical bounds. SRF cavities provide an opportunity for a significantly enhanced axion search due to their extremely large quality factors; however, they must be isolated from large magnetic fields in order to avoid catastrophic SRF degradation. This requires several qualitative modifications from previous setups, most notably the use of a sequestered axion-photon conversion

region containing a confined static magnetic field while production and detection cavities are positioned in regions of vanishing static field. The focus of this paper is to determine the fundamental factors that affect the sensitivity of such an experimental design—a more detailed consideration of experimental strategies is left to future work. We calculate the optimal signal strength and irreducible noise sources, and find the proposed setup capable of probing axion-photon couplings beyond astrophysical limits and with a reach comparable and complementary to next generation optical experiments.

## 2.2 Conceptual Overview

LSW searches rely on the axion EM interaction, given by the effective Lagrangian

$$-\frac{1}{4}F_{\mu\nu}F^{\mu\nu} + \frac{1}{2}(\partial_\mu a)^2 - \frac{1}{2}m_a^2 a^2 - \frac{1}{4}gaF_{\mu\nu}\tilde{F}^{\mu\nu}, \quad (2.1)$$

where  $a$  is the axion field of mass  $m_a$ ,  $\tilde{F}^{\mu\nu} = \epsilon^{\mu\nu\rho\sigma}F_{\rho\sigma}$ , and  $g$  is the axion-photon coupling. In the limit of classical fields, an axion obeys the equation of motion

$$(\square + m_a^2)a = -g\vec{E} \cdot \vec{B}, \quad (2.2)$$

and modifies Maxwell's equations:

$$\vec{\nabla} \cdot \vec{E} = -g\vec{B} \cdot \vec{\nabla}a, \quad (2.3)$$

$$\vec{\nabla} \times \vec{B} = \frac{\partial \vec{E}}{\partial t} - g\left(\vec{E} \times \vec{\nabla}a - \vec{B}\frac{\partial a}{\partial t}\right). \quad (2.4)$$

We will generally consider any light, neutral pseudoscalar  $a$  and treat  $\{m_a, g\}$  as independent parameters.

In an RF LSW experiment such as CROWS [25], a production cavity sources axions through a non-vanishing  $\vec{E} \cdot \vec{B}$ , where  $\vec{E}$  is the electric field of an excited cavity mode and  $\vec{B}$  is an external, static magnetic field. These axions propagate into a detection cavity where, again in the presence of a static magnetic field, they excite an identical frequency mode in the detection cavity. The signal power that can be extracted is [22]:

$$P_{\text{signal}} = P_{\text{input}}Q_{\text{pc}}Q_{\text{dc}}\left(\frac{gB_0}{f}\right)^4|G|^2. \quad (2.5)$$

Here  $Q_{\text{pc}}$  and  $Q_{\text{dc}}$  are the loaded quality factors of production and detection cavities,  $f \approx$  GHz is the frequency of the excited modes,  $P_{\text{input}}$  is the driving RF power delivered to the production cavity, and  $B_0$  is the static field penetrating both cavities.  $|G|$  is a form factor which depends on the arrangement of the cavities, choice of modes, etc. This is roughly constant for  $m_a \lesssim 2\pi f$ , and is exponentially suppressed for larger masses.

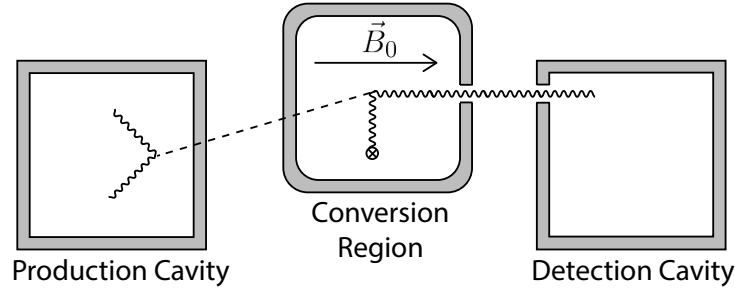


Figure 2.1: Basic elements of an axion LSW experiment using SRF cavities and a conversion region of confined static magnetic field, to be contrasted with an RF cavity experiment such as CROWS [25].

The quality factors  $Q$  of both cavities are key factors in determining the sensitivity of such an experiment. For normal conducting cavities,  $Q \sim 10^5 - 10^6$ , however advances in SRF technology have led to the development of superconducting cavities with  $Q \sim 10^{10} - 10^{12}$  which have application in particle accelerators [27]. It is worthwhile to consider whether these can be leveraged in an axion LSW search [28, 29].<sup>1</sup> A simple replacement of the RF cavities<sup>2</sup> in the above arrangement with SRF cavities does not work—an external  $B_0$  greater than the critical field  $\sim 0.2$  T, at which flux penetrates the cavity, would result in excessive dissipation and degrade  $Q$ .

This problem is avoided by placing production and detection SRF cavities in regions of vanishing static field while confining a large, static magnetic field in a distinct conversion region, depicted schematically in Fig. 2.1. The basic elements of an SRF LSW experiment as follows:

1. Axions are sourced in a production cavity free of any external field.
2. The axions then convert into photons in an isolated region of static magnetic field.
3. The resulting photons propagate out of the conversion region—that is, the axion-induced fields must not also be screened by the conductors which confine the large static field.
4. Any resulting RF signal is coupled to and amplified by an SRF detection cavity.

We discuss a possible design that is able to realize all these conditions, and in what follows we will use it to determine the optimal sensitivity of an axion SRF search.

<sup>1</sup>See [30] for a proposal to detect axions with SRF cavities that is quite distinct from ours.

<sup>2</sup>It is actually not obvious whether a larger signal is obtained by replacing both cavities or only the detection cavity, see Sec. 2.3—we choose here to study an SRF production cavity as it involves some novel considerations.

(1) A specific mode or set of modes in the production cavity is driven such that  $\vec{E} \cdot \vec{B}$  does not identically vanish.

(2) A static  $B_0$  is generated and confined by DC current-carrying superconducting wires wrapped to form a toroidal enclosure.

(3) There is a gap in this enclosure, preventing the toroid from acting as a shielding cavity for the axion-induced fields. Our use of a gapped toroid is inspired by its related use in experiments (ABRACADABRA and DM Radio) searching for dark matter axions [31, 32].

(4) The axion-induced fields are coupled to the detection cavity inductively via an outside pickup loop. Here, we must properly account for the back-reaction of the amplified signal onto the toroid. We emphasize that a realistic implementation would require a more detailed signal field read-out mechanism in order to maintain a large effective  $Q$  on the detection side.

## 2.3 Determining the Axion Signal

### SRF axion source

The axion field produced by an SRF cavity is given by (2.2), with the EM fields on the right-hand-side being those of the driven cavity modes. We focus on one frequency component  $\omega$  of this  $\vec{E} \cdot \vec{B}$ , which may arise from a single cavity mode with frequency  $\omega/2$  or from two distinct modes driven together whose frequency sum or difference is  $\omega$ :

$$a(\vec{x}, t) = -g e^{i\omega t} \int_{\text{pc}} d^3\vec{y} \frac{e^{ik_a|\vec{x}-\vec{y}|}}{4\pi|\vec{x}-\vec{y}|} \left( \vec{E} \cdot \vec{B} \right)_\omega, \quad (2.6)$$

where  $k_a = \sqrt{\omega^2 - m_a^2}$  is the axion momentum and the subscript  $\omega$  on  $\vec{E} \cdot \vec{B}$  indicates restriction to a single frequency component. The integration  $\vec{y}$  is taken over the volume of the production cavity and  $\vec{x}$  indicates any point in space, e.g., within the conversion region. The driven modes must be chosen such that  $(\vec{E} \cdot \vec{B})_\omega$  is not vanishing. This is not an issue in principle, though care must be taken in order to ensure the largest possible magnitude of the axion source (see Appendix A).

An SRF production cavity is unable to support EM fields greater than the critical field at which  $Q$  severely degrades due to flux penetration. This sets a fundamental limit on the strength of an SRF axion source which is independent of the cavity  $Q$ , the input power, or choice of modes. The limit depends only on the material properties of the chosen superconductor. For a standard niobium SRF cavity [33], the field limit is

$$(\vec{E} \cdot \vec{B})_{\text{sf}} \lesssim (0.2 \text{ T})^2. \quad (2.7)$$

By comparison, the axion source produced by an RF cavity in a large static field (as in CROWS) is

$$(\vec{E} \cdot \vec{B})_{\text{rf}} \sim (0.1 \text{ T})^2 \left( \frac{P_{\text{input}}}{100 \text{ W}} \right)^{\frac{1}{2}} \left( \frac{Q_{\text{pc}}}{10^5} \right)^{\frac{1}{2}} \left( \frac{B_0}{5 \text{ T}} \right). \quad (2.8)$$

Interestingly an SRF axion source may be similar in magnitude to that of a conventional LSW setup. The improved reach of our set-up is primarily due to the increase in  $Q$  on the detection side, and the decision to employ an SRF or RF cavity for production would depend on more detailed engineering considerations.

## Gapped toroid conversion region

An axion interacts with the  $\vec{B}_0$  within our conversion region and induces EM fields, described to leading order by effective sources

$$\rho_{\text{eff}} = -g\vec{B}_0 \cdot \vec{\nabla}a, \quad \vec{J}_{\text{eff}} = g\vec{B}_0\partial_t a \quad (2.9)$$

For a toroidal magnet, the static field is of the form  $\vec{B}_0 \sim B_0(r)\hat{\phi}$  within the volume of the toroid, and ideally vanishes everywhere outside. This is the principle advantage of using a toroid, as the SRF cavities can be located in regions of nearly vanishing static field. However it is essential that the toroid be gapped, for instance due to spaces between wire turns. A gapped toroid of this sort acts as a polarizer, confining the toroidal static field while permitting the poloidal axion-induced field to propagate outside and be detected, as shown in Fig. 2.2. Indeed, this behavior is same reason that a gapped toroid is being employed in [31, 32].

We can understand this as follows: the axion effective current  $\vec{J}_{\text{eff}}$  follows the direction of the static toroidal field  $\vec{B}_0$  and sources a poloidal field  $\vec{B}_a$ . Both fields vanish in the toroid thickness as Meissner screening currents are set up on the internal surface. The static field requires poloidal surface currents which are unaware of gaps in the toroid—they do not encounter the gaps as they circulate. For this reason, the static B-field is effectively contained within the toroid. Any leakage is due to fringe effects, which are suppressed by the small size of the gap and can be made smaller than the critical SRF threshold. On the other hand, the axion-induced field will drive toroidal currents which are aware of the gaps. An internal toroidal current must either collect charge on the edges of the gap or propagate onto the external surface of the toroid, where it sources detectable field. This field is unsuppressed by the gap size, as long as the gap has a sufficiently small parasitic capacitance (see Sec. 2.3).

We now make the approximation that all length scales in the setup (cavity sizes, separations, dimensions of the toroid, etc.) are comparable and of order  $\omega^{-1}$ . We additionally assume that the axion-induced poloidal field  $B_a$  is able to escape the toroid without suppression, as though the conducting toroid were not present. This is valid in the quasistatic limit, as we motivate in Sec. 2.3. Combining (2.6) and (2.9), we find the axion-induced field in the center of the torus has a magnitude

$$B_a = \frac{g^2 B_{\text{pc}}^2 B_0}{\omega^2} \beta \approx 10^{-26} \text{ T} \left( \frac{g \text{ GeV}}{10^{-11}} \right)^2 \left( \frac{B_{\text{pc}}}{0.2 \text{ T}} \right)^2 \left( \frac{B_0}{5 \text{ T}} \right) \left( \frac{\beta}{0.05} \right),$$

where  $B_{\text{pc}}$  is the field amplitude in the production cavity (note, we have simply taken  $E_{\text{pc}} \sim B_{\text{pc}}$  in the above estimate) and  $\omega \sim 2\pi \text{ GHz}$ .  $\beta$  is a dimensionless form factor which is a

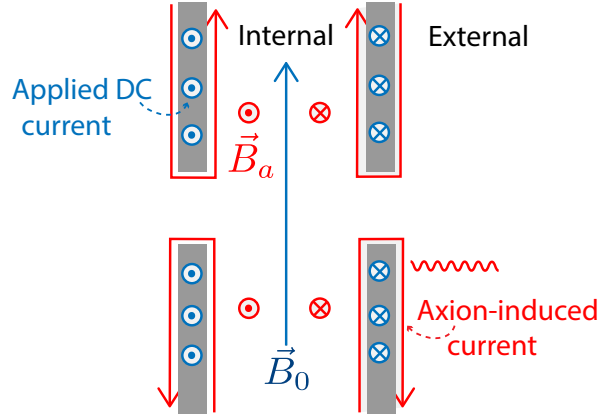


Figure 2.2: Schematic of the gapped toroid as a polarizer, zoomed on to the cross-section of a gap. The static  $\vec{B}_0$  due to applied DC current (blue) remains internal, while the axion-induced  $\vec{B}_a$  (red) causes Meissner screening currents (also red) to flow on internal and external surfaces due to the gap. The external currents give rise to detectable fields outside the toroid.

function of the cavity modes, cavity and toroid geometries, spatial variation in  $\vec{B}_0$ , etc. The size of  $\beta$  is estimated in Appendix A, and we find in principle that it can be made  $\mathcal{O}(0.1)$  in the limit  $m_a \ll \omega$ .

## Screening beyond the quasistatic limit

The reasoning presented above for the propagation of axion-induced fields outside the gapped toroid is essentially valid for quasistatic frequencies,  $R \lesssim \omega^{-1}$ , where  $R$  is the characteristic dimension of the toroid. In the low-frequency limit, the axion-induced magnetic field scales as  $B_a \propto (R\omega)$  and so we would try make our toroid as large as possible. However once  $R$  becomes larger than  $\omega^{-1}$  the axion-induced fields outside the toroid are suppressed (or *screened*), and thus an optimal design would saturate the quasistatic limit  $R \sim \omega^{-1}$ . We discuss this in detail in Appendix B; here we will briefly describe the physical reasons for this result.

Beyond the quasistatic limit, the cross-capacitance of the toroid becomes important: radiation across the center will cause currents and charges on one side of the toroid to affect those on the other side. Meissner currents flowing along the surface of the toroid are no longer approximately uniform; instead, there will be multiple sections of current flowing in opposite directions, with alternating charge buildups in between. The resulting Meissner currents and charge distribution is spatially modulated and behaves as a multipolar source. We thus expect the axion-induced fields outside the toroid to drop-off parametrically as a power-law  $B_a \propto (R\omega)^{-n}$ , due to destructive interference of out-of-phase source contributions. We show this behavior and calculate  $n > 0$  explicitly for a toy model of a thin cylindrical conductor

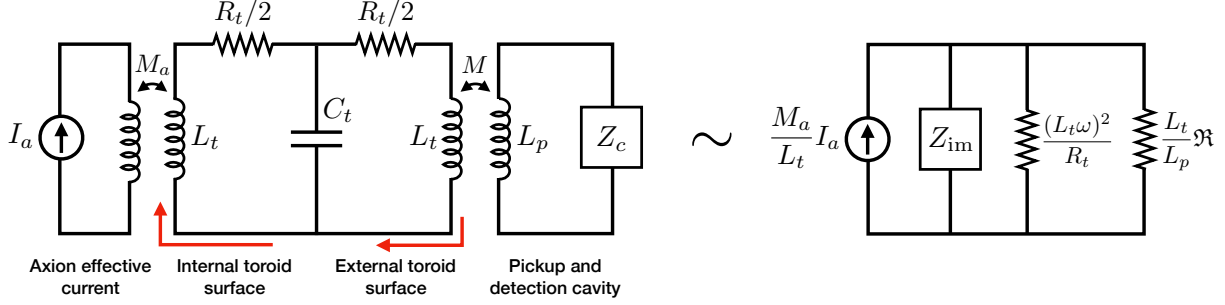


Figure 2.3: (Left) Mapping of our experimental setup onto an effective circuit model. This is parameterized by an axion effective current ( $I_a$ ) running through the toroid volume, effective mutual inductance capturing the Meissner effect ( $M_a$ ), toroid inductance ( $L_t$ ), toroid resistance ( $R_t$ ), shunting capacitance ( $C_t$ ), inductive coupling to an outside pickup loop ( $L_p$ ) through a mutual coupling ( $M$ ), and a detection cavity ( $Z_c$ ). (Right) Approximate equivalent circuit, for the purposes of computing the maximum signal power.  $\Re \propto Q$  is the detection cavity shunt resistance and  $Z_{\text{im}}$  contains all imaginary impedances.

in the high-frequency limit in Appendix B. Thus, we expect it is safe to saturate  $R \sim \omega^{-1}$  without concern that there will be a precipitous (e.g., exponential) drop in the external fields for slightly larger sizes or frequencies. Likewise, we may treat the approximation of  $\mathcal{O}(1)$  field propagation as accurate even at the boundary of the quasistatic limit.

Note that in our setup the internal toroid signal currents will also have significant spatial modulation beyond the quasistatic limit, but for a very different reason: the source axion field (2.6) itself varies on length scales of order  $\omega^{-1}$  due to the propagator factor, independent of the choice of modes. In any case, the multipolar screening described in this section is more general and results from satisfying boundary conditions on the superconducting toroid—this would be present even if the axion field were spatially uniform.

## Pickup and equivalent transducer circuit

To compute the signal strength, it is useful to describe this system with a model circuit, as in the left side of Fig. 2.3. For concreteness we assume the axion-induced EM field is coupled to the detection cavity via a pickup loop located in the central hole of the toroid. An actual design would likely require a more sophisticated read-out mechanism in order to maintain a large effective  $Q$ , however this does not alter the optimal signal power.

The model circuit is a straightforward rendering of the signal current flowing on the toroid. This current flows toroidally, distributed over the inner and outer surfaces of the toroid, as discussed in Sec. 2.3. We focus on the loop of signal current nearest to the pick-up loop, which flows around the central hole, concentric to the pick-up. This current path is represented in the model circuit by the red arrows in Fig. 2.3, and it includes segments on



both the inner and outer toroid surface. The magnitude of toroid current is determined by the Meissner boundary conditions. It thus receives contributions from the magnetic fields produced by both the axion effect current and any current in the pick-up loop, the latter being a back-reaction which sets the maximal power that may be drawn from the pick-up loop.

The axion effective current in the volume of the toroid is represented by  $I_a$ , and its coupling to the inner toroid surface current by an effective mutual inductance  $M_a$ . The self inductance of the toroid current path is  $L_t \sim R$ , with  $R$  the toroid radius. We choose  $M_a \sim R$ , which ensures that the current driven in the model circuit due to  $I_a$  agrees with that required by the Meissner effect. The current induced on the inner surface of the toroid can pass to the outer surface, where it couples to a pickup loop of inductance  $L_p$  through a mutual inductance  $M$  and then feeds into a cavity of impedance  $Z_c$ . Alternatively, the current may jump across the gaps between wires and remain on the inner surface: this is captured by the shunting capacitance  $C_t$ . As we will show,  $\omega L_t \ll (\omega C_t)^{-1}$ , and so current always prefers to circulate between the inner and outer surfaces.

The resistances  $R_t$  account for the tiny but non-zero surface losses on the toroid. It is valid to ignore  $R_t$  when determining the magnitude of axion-induced fields through. However, it is important not to ignore it entirely when considering the amplification of signal fields by the SRF cavity. The detection cavity will be rung up to contain a large current, for which the pickup loop  $L_p$  will act as an antenna and excite additional currents on the external surface of the toroid, resulting in additional dissipation via  $R_t$ . This back-reaction current is again set by the Meissner boundary conditions, which are reproduced by  $M$  and  $L_t \sim R$  in the circuit model of Fig. 2.3. Taking the pick-up loop to have radius  $r$  and contain a current  $I_p$ , it will source a field at the toroid surface  $B \sim I_p r^2 / R^3$  which requires a Meissner current  $I \sim BR \sim I_p r^2 / R^2$ . Since the mutual inductance is of order  $M \sim r^2 / R$ , the required current is indeed  $I \sim I_p M / L_t$  that derived from considering our circuit.

We now estimate the relevant model circuit parameters. The current source  $I_a$  represents the total axion effective current threading the toroid and is of order  $J_{\text{eff}} R^2$ . More precisely, it is the current that gives rise to the outside field  $B_a$ :

$$I_a \sim B_a R \sim \frac{g^2 B_{\text{pc}}^2 B_0}{\omega^3} \beta \approx 10^{-13} \text{ nA} \left( \frac{g \text{ GeV}}{10^{-11}} \right)^2 \left( \frac{B_{\text{pc}}}{0.2 \text{ T}} \right)^2 \left( \frac{B_0}{5 \text{ T}} \right) \left( \frac{\beta}{0.05} \right),$$

again with  $\omega = 2\pi \text{ GHz}$  and  $m_a \ll \omega$ .

Strictly speaking, the two toroid inductances labeled  $L_t$  may be different as they inductively couple to different objects. They are both set by the toroid size, however, so for simplicity we take them both to be

$$L_t \sim R \approx 125 \text{ nH} \left( \frac{R}{10 \text{ cm}} \right). \quad (2.10)$$

If the toroid is composed of  $N$  turns of wire, then  $C_t$  is given by

$$C_t \sim \frac{1}{N} \frac{2\pi R \cdot d}{g} \quad (2.11)$$

where  $d$  is the wire diameter and  $g = 2\pi R/N - d$  is the spacing between wires. For fixed wire diameter,  $C_t$  and the fringe fields can be made small by taking a large  $N$  and  $g \approx d$ , which yields:

$$C_t \approx 10^{-2} \text{ pF} \left( \frac{d}{\text{mm}} \right). \quad (2.12)$$

The use of superconducting wires allows  $R_t$  to be as small as few  $\text{n}\Omega$  (the minimum RF surface resistance of type II superconductors [34]), or at worst as large as  $\text{m}\Omega$  (the nominal low-temperature resistance of quenched NbTi wires [35]). We expect the resistance will be somewhat larger than  $\text{n}\Omega$ , as the wires operate in the vortex state and harbor toroidal magnetic flux tubes. These tubes interact with RF currents in the wires via the so-called Magnus force [36], and their resulting motion is a significant source of dissipation [37]. The precise value of  $R_t$  will depend on the detailed geometry of the flux tubes and the surface current. We provide a rough estimate of this resistance, but stress that in what follows we consider the consequences of any  $R_t$  within the above bounds. Since the interaction of RF currents and flux tubes is of the “Lorentz” form  $\vec{J} \times \vec{B}$ , the resistance should scale as  $\sin \theta$ , the angle between the direction of flux tubes and that of the RF current. In this system, the magnetic field inducing the flux tubes is toroidal but the axion-induced current is poloidal, and so ideally  $\theta = 0$ . However, the flux tubes will not be perfectly toroidal: static fringe fields provide a deflection of order  $\theta \sim B_f/B_0$ . ABRACADABRA has measured the fringe fields outside of their toroidal magnet to be  $10^{-6}$  of the primary field [38], which we adopt here. We assume that the deflected component of flux tubes contribute an RF resistance similar to that of trapped flux in SRF cavities, which is on the order  $\text{n}\Omega/\text{mG}$  [34]. Thus we estimate:

$$R_t \approx 100 \text{ n}\Omega \left( \frac{B_0}{5 \text{ T}} \right) \left( \frac{\theta}{10^{-6}} \right). \quad (2.13)$$

Finally, we choose to model the cavity as a parallel RLC circuit for concreteness, with capacitance  $C$ , inductance  $L$ , resistance  $\Re$ , and thus an impedance:

$$Z_c = \left( \frac{1}{\Re} + \frac{1}{i\omega L} + i\omega C \right)^{-1}. \quad (2.14)$$

This cavity has natural resonance frequency  $\omega_0^2 = (LC)^{-1}$  and quality factor  $Q = \Re/\omega_0 L \gg 1$ . We take  $\omega_0 \sim L^{-1} \sim C^{-1} \sim 2\pi \text{ GHz}$ , as set by the physical cavity size. Note that the effective shunt resistance  $\Re$  of this cavity model is very large, proportional to the inverse of the small resistivity of the cavity walls.

All the circuit parameters have so far been estimated by physical considerations, except the pickup loop inductance  $L_p$ . This is a free parameter which we tune to optimize the signal, within reasonable limitations as discussed in Sec. 2.3. We assume the mutual inductance  $M$  can be made close to optimal,  $M \approx \sqrt{L_p L_t}$ . There is also some freedom in choosing the frequency  $\omega$  sourced by the production cavity. Indeed,  $\omega$  need not be exactly equal the detection cavity’s natural frequency  $\omega_0$ , although we require that both lie in the GHz range.

## Optimal signal strength

The signal we are able to extract is given by the power dissipated in the detection cavity. Here we compute the maximum of this power, varying the pickup inductance and driving frequency. We use our model circuit for this, and employ the equivalent circuit shown on the right side of Fig. 2.3. This circuit is constructed such that, to lowest order in the small quantities  $R_t$  and  $C_t$ , the power dissipated in the resistor  $(L_t/L_p)\Re$  is the same as the power dissipated in the cavity impedance  $Z_c$ . Similarly, the power dissipated in the resistor  $(L_t\omega)^2/R_t$  is the same as the total power dissipated in the toroid resistors.

This can be demonstrated by making a series of transformations to sub-circuits of the circuit on the left side of Fig. 2.3, each of which preserves the input, output, and dissipated power of the transformed sub-circuit and results in a purely parallel topology. First, the leftmost transformer can be replaced by a rescaled current source  $I_a M_a/L_t$  and inductor  $L_t$ . Recall that  $M_a \sim L_t$ , so the rescaled current is  $\mathcal{O}(I_a)$ . Next the elements between the transformers can be rewritten to lowest order in  $R_t$  and  $C_t$  as a resistor  $(L_t\omega)^2/R_t$  and capacitor  $C_t$ . Finally, the rightmost transformer and cavity impedance can be replaced by an inductor  $L_t$  and a rescaled cavity  $(L_t/L_p)Z_c$ . The imaginary impedances are gathered into  $Z_{\text{im}}$ , which to lowest order in  $R_t$  and  $C_t$  is:

$$Z_{\text{im}} \sim \left( \frac{2}{i\omega L_t} + i\omega C_t + \frac{1}{i\omega \frac{L_t}{L_p} L} + i\omega \frac{L_p}{L_t} C \right)^{-1}. \quad (2.15)$$

The system is on resonance when  $Z_{\text{im}}^{-1} = 0$ . To lowest order in  $C_t$ , this occurs at the frequency

$$\omega_{\text{res}} \sim \omega_0 \sqrt{1 + 2 \frac{L}{L_p}}, \quad (2.16)$$

which we will choose to be our driving frequency  $\omega$ . On resonance, all current in the equivalent circuit passes through the two resistors. The power dissipated in the cavity resistor is maximized when these two resistors are equal, which occurs at a pickup loop inductance of

$$L_{\star} \sim L \frac{QR_t}{L_t \omega_0}. \quad (2.17)$$

An inductance  $L_p$  that is significantly less than  $L$  results in a resonance frequency that is far perturbed from the natural one. In a realistic experimental implementation, care would need to be taken to ensure that the loaded resonance frequency was not too far perturbed from the detection cavity's natural frequency, lest the quality factor degrade. As a heuristic implementation of this, we will demand that  $\omega \sim \omega_0$  and thus  $L_p \gtrsim L$ .

We will consider the optimal signal power in two parameter regimes. First, suppose the cavity is of higher quality than the toroid,  $\Re = Q\omega_0 L \gg 1/R_t$ . Impedance matching requires

$L_p = L_\star \gg L$ , happily yielding a resonance frequency very close to  $\omega_0$ . We then draw the *toroid-limited* power

$$P_{\max} \sim \frac{1}{8} |I_a|^2 \frac{(L_t \omega)^2}{R_t}. \quad (2.18)$$

This is the maximal power that can be extracted from the toroid as long as the driving frequency remains near  $\omega_0$ . It thus depends only on the toroid properties and frequency, and notably does not scale with  $Q$ .

In the second case, suppose that the toroid is of higher quality than the cavity,  $\Re = Q\omega_0 L \ll 1/R_t$ . We would hope to again match  $L_p$  to  $L_\star$ , however that would require  $L_p \ll L$  and we are thus prevented from impedance matching. Insisting on  $L_p \gtrsim L$ , the optimal choice is  $L_p \sim L$  for which we draw the *cavity-limited* power

$$P_{\max} \sim \frac{1}{2} |I_a|^2 Q L_t \omega_0. \quad (2.19)$$

In general, the maximum signal power is the lesser of (2.18) and (2.19), being limited by resistive losses in the toroid or cavity, respectively:

$$P_{\text{signal}} \sim |I_a|^2 (\omega L_t) \text{Min} \left[ \frac{\omega L_t}{R_t}, Q \right] \quad (2.20)$$

The relevant toroid parameter to be compared with  $Q$  is

$$\frac{\omega L_t}{R_t} \sim 10^{10} \left( \frac{100 \text{ n}\Omega}{R_t} \right). \quad (2.21)$$

Thus for  $Q \gtrsim 10^{10}$  the toroid impedance may indeed be non-negligible. The numerical similarity between  $Q$  and  $\omega L_t/R_t$  reflects the fact that both arise from the small resistivity of superconductors to RF currents. This also suggests that the experimental details which affect the losses in these systems will be important in determining which of the above regimes is realized.

## 2.4 Sensitivity to Axion-Photon Coupling

### Noise

The fundamental sources of noise in this system are thermal and quantum fluctuations of current in the toroid and detection cavity, as well as the intrinsic noise of the device which reads the amplified signal from the cavity. The thermal and quantum noise can be estimated from the circuit on the right side of Fig. 2.3. The equivalent resistances of both the cavity and toroid will source Johnson currents, behaving as additional parallel current sources. With  $L_p$  tuned as outlined in Sec. 2.3, the noise sourced by the effective cavity resistance

is always greater than or equal to that sourced by the toroid resistance, so we take a noise source  $I_T$ :

$$\langle |I_T|^2 \rangle \sim 4T_{\text{sys}} \frac{1}{\Re} \frac{L_p}{L_t} d\nu. \quad (2.22)$$

The system temperature  $T_{\text{sys}}$  is the sum of the thermal temperature  $T$  and the quantum noise temperature  $T_{\text{QM}} \sim \omega \approx 50$  mK.  $I_T$  drives fluctuations of the physical magnetic flux  $\Phi_T$  inside the detection cavity,

$$|\Phi_T| = \frac{\Re}{\omega_0} \sqrt{\frac{L_t}{L_p}} |I_T| \quad (2.23)$$

resulting in a noise spectrum of cavity flux,

$$S_\Phi^{1/2} \sim \left( 4T_{\text{sys}} \frac{QL}{\omega_0} \right)^{\frac{1}{2}} \approx \frac{\Phi_0}{\sqrt{\text{Hz}}} \left( \frac{T_{\text{sys}}}{0.1 \text{ K}} \right)^{\frac{1}{2}} \left( \frac{Q}{10^{10}} \right)^{\frac{1}{2}}$$

where  $\Phi_0$  is the fundamental magnetic flux quantum.

Consider coupling the small signal flux in the cavity to a low-noise read-out device, such as a SQUID magnetometer. The intrinsic flux noise in such devices is of order  $10^{-6} \Phi_0 / \sqrt{\text{Hz}}$  [39], much smaller than the cavity fluctuations (2.24). We thus take (2.24) as the dominant source of noise.

## Projected sensitivity

The noise power extracted from the cavity due to the fluctuations (2.22) is

$$P_{\text{noise}} = \Re \frac{L_t}{L_p} \langle |I_T|^2 \rangle \sim 4T_{\text{sys}} d\nu \quad (2.24)$$

and the signal-to-noise ratio (SNR) thus

$$\text{SNR} \sim \frac{1}{8} |I_a|^2 (\omega L_t) \text{Min} \left[ \frac{\omega L_t}{R_t}, Q \right] \frac{t_{\text{int}}}{T_{\text{sys}}} \quad (2.25)$$

where the relevant bandwidth  $d\nu$  is given by the inverse of the total integration time  $t_{\text{int}}$ .

One may be concerned that tuning  $L_p$  to as outlined in Sec. 2.3 to maximize the power draw is not truly optimal, as the best measurement will result from maximizing the SNR. The signal and noise powers extracted from the detection cavity for a general  $L_p$ , derived from the circuit on the right side of Fig. 2.3, are

$$P_{\text{signal}} \sim |I_a|^2 \frac{(L_t \omega)^2}{R_t} \left( \frac{L_\star}{L_p} \right) \left( 1 + \frac{L_\star}{L_p} \right)^{-2}, \quad (2.26)$$

$$P_{\text{noise}} \sim T_{\text{sys}} d\nu \left( 1 + \frac{L_\star}{L_p} \right)^{-1}. \quad (2.27)$$

The SNR thus nominally increases with decreasing  $L_p$ , although it saturates to the intrinsic SNR of the toroid at the impedance matched  $L_p = L_\star$ . The optimal choice of  $L_p$  is thus either  $L_\star$  or  $L$ , the same as that which draws the maximal power (2.20).

Demanding  $\text{SNR} > 5$ , the estimated reach at low axion masses  $m_a \ll \omega$  is given by:

$$g > 2 \cdot 10^{-11} \text{ GeV}^{-1} \cdot \left( \frac{\omega/2\pi}{\text{GHz}} \right) \left( \frac{B_0}{5 \text{ T}} \right)^{-\frac{1}{2}} \left( \frac{B_{\text{pc}}}{0.2 \text{ T}} \right)^{-1} \left( \frac{\beta}{0.05} \right)^{-\frac{1}{2}} \\ \left( \frac{L_t}{125 \text{ nH}} \right)^{-\frac{1}{2}} \left( \frac{R_t}{100 \text{ n}\Omega} \right)^{\frac{1}{4}} \left( \frac{t_{\text{int}}}{\text{year}} \right)^{-\frac{1}{4}} \left( \frac{T_{\text{sys}}}{0.1 \text{ K}} \right)^{\frac{1}{4}}. \quad (2.28)$$

This is independent of the detection cavity quality factor if it is sufficiently large ( $Q \geq 10^{10}$  for these parameters). The full sensitivity is show in Fig. 2.4 using:

$$\frac{\omega}{2\pi} = \text{GHz}, \quad B_{\text{pc}} = 0.2 \text{ T}, \quad B_0 = 5 \text{ T}, \quad L_t = 125 \text{ nH}, \quad t_{\text{int}} = 1 \text{ year}, \quad T_{\text{sys}} = 0.1 \text{ K},$$

and considering two cases of cavity and toroid losses:

$$(1) R_t = 100 \text{ n}\Omega \quad \text{and} \quad Q \geq 10^{10}, \quad (2) R_t = \text{n}\Omega \quad \text{and} \quad Q \geq 10^{12}.$$

We have used a form factor of  $\beta = 0.05$ , assuming  $m_a \ll \omega$  (see Appendix A). The estimated sensitivity of our SRF axion design is capable of surpassing current astrophysical limits, and is comparable to the expected reach of the next generation optical experiment, ALPS II [21].

## 2.5 Discussion

We have proposed a novel design for an LSW axion search leveraging SRF cavity technology and employing a region of isolated, static magnetic field. Our particular realization uses a gapped toroid, similar to that of [31, 32], to contain a static field while allowing the propagation of axion-induced signal fields. It would be interesting to consider other possible geometries for the conversion region, though the gapped toroid illustrates the necessary features. Our focus in this work is understanding the fundamental factors which set the sensitivity of such an experiment, namely the possible screening of the signal fields beyond the quasistatic limit and back-reaction from the non-negligible toroid impedance. We calculate the optimal signal strength, and for reasonable toroid parameters and SRF quality factors we find a sensitivity to axion-photon couplings in excess of astrophysical limits and comparable to complementary optical experiments. Notably, the optimal sensitivity is in fact independent of both production and detection cavity  $Q$  factors in the limit of large  $Q$ , and is instead determined by the properties of the conversion region.

We conclude with a few comments on experimental feasibility that have not yet been addressed. We have modeled the coupling of the detection cavity and axion-induced signal fields with an inductive pickup, yet a naive implementation of such a coupling would likely

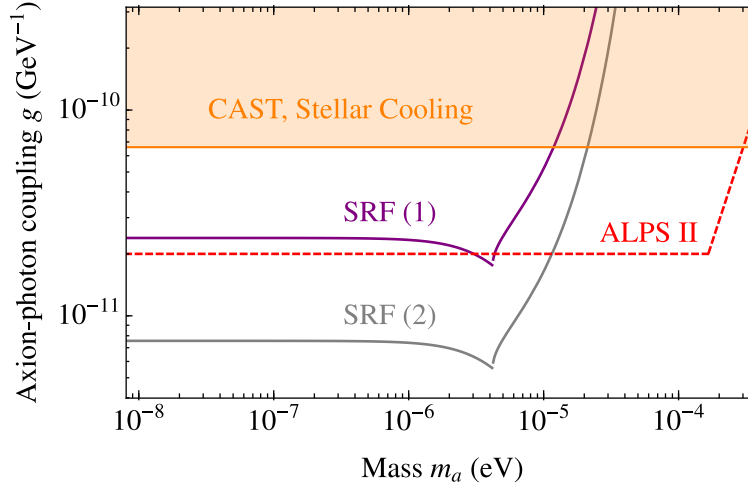


Figure 2.4: Projected sensitivity of proposed SRF LSW setup to axion-photon couplings—see text for the choices of experimental parameters. Also shown are existing solar axion (CAST) [40] and stellar cooling bounds and, for comparison, the future projected reach of the next generation optical experiment ALPS II [21].

compromise the detection  $Q$  due to losses in the pickup wire. It is critical to explore coupling mechanisms that will not degrade  $Q$ , which is complicated by the fact that the toroid operates on the extreme of the quasistatic regime and thus requires microwave engineering. There are other sources of noise not considered here which must be understood and managed in a practical implementation, such as stray external fields which require shielding and additional losses due to non-superconducting support materials used in the system. Finally, perhaps the biggest engineering challenge here is the necessity of frequency-matching the two SRF cavities to within  $1/Q \lesssim 10^{-10}$ . This demands a precise resonance monitoring and feedback mechanism to counter frequency drifts, and is a major hurdle for any photon regeneration experiment utilizing high- $Q$  cavities, such as [41].

## Chapter 3

# Parametric Resonance Production of Ultralight Vector Dark Matter

### 3.1 Introduction

The existence of dark matter (DM) is one of the observational evidences for physics beyond the Standard Model (SM). Recently, vectors ( $X_\mu$ ) have gained significant attention as an intriguing DM candidate with unique experimental signatures [42, 43, 44]. Theoretically, light vectors arise as gauge bosons of dark U(1)s, a simple extension of the SM and a common prediction of high energy theories. The origin of the vector mass is model-dependent and can either be a fundamental parameter in the full theory via the Stueckelberg mechanism, or can be generated through its coupling to an additional field which spontaneously breaks the corresponding U(1) via the Higgs mechanism. In either scenario the mass of the vector is stable under quantum corrections, motivating the possibility of vectors with ultralight masses,  $m_X \ll \text{MeV}$ , limited only to having wavelengths small enough to form galaxies,  $m_X \gtrsim 10^{-22} \text{ eV}$ .

Experimentally, light relic vectors present different opportunities depending on their coupling to the SM. The overarching challenge in experimental prospects is competing with the powerful limits from stellar cooling [44, 45] and fifth forces [46] while restricting considerations to the (approximately) conserved currents of the SM (otherwise one generically expects dominant constraints from flavor changing neutral currents [47, 48]). Nevertheless there exist many experimental proposals to search for vector DM in unexplored parameter space. Such states can be observed through their coupling to electrically charged particles that could be searched for in resonant cavities [49], LC circuits [31], dish antennas [50], absorption in direct detection experiments [51, 52, 53], and low-energy threshold detectors [54, 55, 56, 57, 58]. If the vector couples to an unscreened force such as  $B - L$  then its coupling to neutral matter can be searched for in torsion balances and atom interferometry [59], gravitational wave detectors [59, 60], and pulsar binary systems [61]. With current and proposed experiments, searches for vector DM can be undertaken over almost the entire mass range



$10^{-22} \text{ eV} \lesssim m_X \lesssim \text{MeV}$ .

While ideas to detect vector DM are plentiful, the theoretical prospects for producing ultralight vector DM are much less explored. For light vectors there are three classes of production which have been studied in the literature: freeze-in [62], misalignment [44], and inflationary fluctuations [63]. Freeze-in production is generically constrained by the bound on warm DM. Particles “frozen-in” through an interaction with the SM are produced with energy/momentum  $\sim T$ , the temperature of the thermal bath. Without additional dynamics the momentum of the relics will redshift with the expansion of the universe and hence track the SM photon temperature, limiting the produced DM mass to be above a keV to be consistent with the observation of small scale structure.

Misalignment has long been a standard non-thermal production mechanism for light bosons, first proposed for axions [9, 10, 11], and later considered for massive vectors [43, 44]. Here, a zero-momentum condensate of particles is produced as a result of the coherent oscillations of the field initially displaced from its minimum. For a generic scalar  $\phi$  the energy density in the field  $\rho_\phi \sim m_\phi^2 \phi^2$  remains constant when the Hubble scale is greater than its mass  $H \gg m_\phi$  and the field value is stuck. Crucially, this is not the case for a massive vector  $X$ : the energy density in the vector field continues to red-shift as  $\rho_X \sim m_X^2 X_\mu X^\mu \propto a^{-2}$  when  $H \gg m_X$  due to the scale factor dependence in the FRW metric on the vector norm. Thus any initial energy density in a massive vector field is exponentially diluted during a period of inflation, and the minimal misalignment production of vector DM fails. This problem is avoided if an  $\mathcal{O}(1)$  non-minimal coupling to gravity is added to make the vector conformally invariant and hence impervious to the expansion of the universe [44]. However such a special coupling quantum-mechanically destabilizes the mass of  $X$ , thus destroying one of the primary motivations for considering vector DM.

Alternatively, vector DM can be produced by the quantum fluctuations during inflation [63]. This is a very interesting possibility, as such a production has no dangerous large-scale isocurvature perturbations and appears unique to vectors. Here, the observed DM abundance is saturated for  $m_X \simeq 10^{-5} \text{ eV} (10^{14} \text{ GeV}/H_{\text{inf}})^4$ , and thus observational constraints on the Hubble scale during inflation [64] limit the production to masses greater than about  $10^{-5} \text{ eV}$ .

In this paper, we propose a new production mechanism for vector DM that occurs naturally if it obtains mass through a dark Higgs field. Generically, the production relies on a scalar field being displaced far from its minimum by the end of inflation. As the field rolls down its potential and begins to oscillate, its coupling to a vector results in a rapidly oscillating mass for the vector. This leads to non-perturbative production of  $X$  particles through a parametric resonance (PR) instability (as is the case in theories of reheating [65, 66, 67, 68], though the dynamics we consider take place solely during radiation domination). Crucially, the rate of production is much greater than that of any possible perturbative process. The produced particles then have more time to red-shift, significantly relaxing the coldness constraint and allowing for the production of ultralight DM. This is in analogy with earlier work [69] on the PR production of axion DM via dynamics of a Peccei-Quinn symmetry breaking field (for other work on non-perturbative production of relics, see [70, 71, 72, 73]).

In this paper we focus on the minimal case where the scalar field is a dark Higgs. The nature of the resonance and resulting abundance of vectors and dark Higgses is different depending on the strengths of the gauge coupling  $e$  and dark Higgs quartic coupling,  $\lambda$ . We examine both limits and find that vector DM can be produced with masses as light as  $m_X \gtrsim 10^{-18}$  eV, consistent with all constraints. This opens up most of the mass range for vector DM as cosmologically viable, and further motivates the experimental program searching for such particles.

The paper is organized as follows. In Sec. 3.2 we outline the model of interest and show the limitations of a perturbative Higgs decay in producing light vector DM. In Sec. 3.3 we review the relevant non-perturbative dynamics of PR, specifically as it applies to vector production. In Sec. 3.4 we examine the PR production of ultralight vector DM, and in Sec. 3.5 we discuss additional cosmological consequences and constraints on the mechanism. Finally, in Sec. 3.6 we conclude and discuss future directions.

## 3.2 The Model

We now present an outline of the model and detail the dynamics of an oscillating scalar field in the potential. As our starting point we consider a complex scalar field,  $\varphi$ , that will give a mass to the vector:

$$\mathcal{L} = -\frac{1}{4}X_{\mu\nu}X^{\mu\nu} + |D_\mu\varphi|^2 - V(\varphi), \quad (3.1)$$

where  $D_\mu = \partial_\mu + ieX_\mu$ ,  $e$  is the dark gauge coupling constant (we absorb the scalar charge into the definition of  $e$ ), and  $X_{\mu\nu}$  is the field strength tensor. We consider the simplest model of spontaneous symmetry breaking with a potential parameterized as

$$V(\varphi) = \lambda^2 \left( |\varphi|^2 - \frac{v^2}{2} \right)^2. \quad (3.2)$$

Expanding  $\varphi$  around the vacuum expectation value (VEV), we obtain:

$$\mathcal{L} \supset \frac{1}{2}e^2v^2 \left( 1 + \frac{\phi}{v} \right)^2 X_\mu X^\mu - V(\phi), \quad (3.3)$$

where

$$V(\phi) = \frac{1}{4}\lambda^2\phi^2 (\phi + 2v)^2. \quad (3.4)$$

The vacuum masses of  $X$  and dark Higgs boson are  $m_X = ev$  and  $m_\phi = \sqrt{2}\lambda v$ , respectively<sup>1</sup>. Furthermore, we refrain from making any assumptions about the magnitude of the vector

---

<sup>1</sup>Note that while the vector mass is radiatively stable, the scalar mass is not and naturalness would suggest a cut-off of order  $\Lambda \lesssim v \min\{1, m_\phi/m_X\}$ . Ultimately we will be interested in VEVs much larger than the weak scale, so fine-tuning in the dark Higgs sector is not a serious constraint and we will not address it further.

coupling to the SM, up to assuming the coupling is not so large that it efficiently thermalizes the two sectors (or is phenomenologically excluded in other ways).

We assume  $\phi$  starts out displaced from its minimum after inflation with an initial field value,  $\phi_0$ . The classical equation of motion for  $\phi$  is

$$\ddot{\phi} + 3H\dot{\phi} + \lambda^2(\phi^3 + 3v\phi^2 + 2v^2\phi) = 0, \quad (3.5)$$

which is valid as long as the back-reaction due to any created particles is negligible (these effects are crucial in the termination of non-perturbative particle production and will be addressed later). The field is stuck until  $H \sim m_{\text{eff}}(\phi_0)$  where  $m_{\text{eff}}(\phi) = \sqrt{V''(\phi)}$  is the effective (field-dependent) mass, at which point  $\phi$  begins oscillating about the minimum. As long as  $\phi_0 \ll M_{\text{pl}}$  (regardless of the hierarchy between  $\phi_0$  and  $v$ ) the universe is radiation-dominated at the onset of oscillations which begin at,

$$T_{\text{osc}} \simeq 0.5\sqrt{m_{\text{eff}}M_{\text{pl}}} \quad (3.6)$$

where  $M_{\text{pl}} = 2.4 \times 10^{18}$  GeV is the reduced Planck mass.

We now consider the two limits for the initial field value,  $\phi_0 \ll v$  and  $\phi_0 \gg v$ . If  $\phi_0 \ll v$ , oscillations start at  $T_{\text{osc}}$  and the solution is the well-known harmonic oscillations,  $\phi(t) = \Phi \cos(m_\phi t)$ . The amplitude of oscillations red-shifts with the scale factor  $a$  (we use the convention that  $a = 1$  at the onset of oscillation) as  $\Phi(t) = \phi_0 a^{-3/2}$ , and the energy density in coherent oscillations acts as non-relativistic matter  $\rho_\phi \propto a^{-3}$ .

Conversely, if the field value is large,  $\phi_0 \gg v$ , then the effective mass is  $m_{\text{eff}}(\phi_0) \simeq \sqrt{3}\lambda\phi_0$  with  $T_{\text{osc}} \simeq \sqrt{\lambda\phi_0 M_{\text{pl}}}$ . Due to the conformal invariance of the quartic potential, it is most convenient to switch to conformal coordinates. Furthermore, it is convenient to absorb the oscillation time into our definition suggesting the coordinate transformation  $\bar{\phi} \equiv a\phi/\phi_0$  and  $dz \equiv \lambda\phi_0 dt/a$ . The equation of motion is then simply:

$$\bar{\phi}'' + \bar{\phi}^3 = 0, \quad (3.7)$$

where we use primes to denote derivatives with respect to  $z$ . The exact solution is an elliptic cosine function with elliptic modulus of  $1/2$ ,

$$\bar{\phi}(z) = \text{cn}(z). \quad (3.8)$$

This function is usually well-approximated by the simple cosine function,  $\bar{\phi} \simeq \cos(0.85z)$ , the first term in its Lambert series expansion, but some features require keeping higher order terms and so we refrain from making this approximation. Here, the (original) field amplitude instead red-shifts as  $\Phi(t) = \phi_0 a^{-1}$  and the energy density in coherent oscillations acts like radiation  $\rho_\phi \propto a^{-4}$ .

## Perturbative Decay

The dynamics of particle production depend critically on the initial field value, and we postpone a careful treatment to Sec. 3.3. However, we generally expect non-perturbative

effects are negligible if  $\phi_0 \ll v$  and we briefly review the physics in this limit. We first compute the production of vector DM from perturbative decay of the dark Higgs—this will eventually highlight the effectiveness of parametric resonance. Coherent oscillations of the  $\phi$  field result in an yield of dark Higgs:

$$Y_\phi = \frac{\rho_\phi}{m_\phi s} \simeq \frac{0.5}{\lambda^{1/2}} \left( \frac{\phi_0}{v} \right)^2 \left( \frac{v}{M_{\text{pl}}} \right)^{3/2}, \quad (3.9)$$

where  $s$  is the entropy density. This population can decay into  $X$  if it is kinematically allowed, i.e.,  $m_\phi > 2m_X$ . Since the co-moving number density in the dark sector is conserved, the dark Higgs condensate will fully convert into a co-moving number density of vectors  $Y_X = 2Y_\phi$ . The timescale for this conversion is set by the decay rate  $\Gamma_{\phi \rightarrow XX}$ , which is dominated by the decay into longitudinal modes of  $X$ :

$$\Gamma_{\phi \rightarrow XX} \simeq \frac{m_\phi^3}{32\pi v^2}. \quad (3.10)$$

The underlying challenge with DM production via decays is that the  $X$  particles are initially highly boosted with momentum  $\mathcal{O}(m_\phi)$ . In this case, the produced vectors begin red-shifting as non-relativistic matter once the universe cools to a temperature

$$T_{\text{NR}} \simeq 0.1 \, m_X \left( \frac{M_{\text{pl}} \lambda}{v} \right)^{1/2}. \quad (3.11)$$

From here on  $T_{\text{NR}}$ , and in general the term “temperature”, refers to that of the SM thermal bath (this is distinct from a possible dark sector temperature, which may or may not even be in thermal equilibrium). As expected,  $T_{\text{NR}}$  increases with  $\lambda$  which corresponds to earlier decays. Observations of cosmological large-scale structure require that the DM be non-relativistic by around a keV and so we require  $T_{\text{NR}} \gtrsim \text{keV}$  [74, 75, 76] (precise constraints range from  $\sim 1 - 5$  keV though suffer from astrophysical uncertainties). Based on (3.9) and (3.11), we find the vector abundance equals the relic density of DM for masses:

$$m_X \simeq 10 \left( \frac{T_{\text{NR}}^3 T_{\text{eq}}}{\lambda} \right)^{1/4} \left( \frac{v}{\phi_0} \right)^{1/2}, \quad (3.12)$$

where  $T_{\text{eq}} \simeq 0.75$  eV is roughly the temperature at matter-radiation equality. Note that production of light vector DM here favors large values of  $\lambda$ , which is ultimately limited by perturbativity  $\lambda < 2\pi$  (this is in fact a stronger condition than  $\phi_0 < M_{\text{pl}}$ ). Saturating the coldness and perturbativity constraints, we conclude that it is impossible to produce vector DM with mass less than a keV using perturbative decays of the scalar field.

### 3.3 Parametric Resonance

If  $\phi_0 \gg v$ , the production rate of vectors can be much larger than the perturbative rate. Such a large initial field value is a generic expectation unless the coupling with an inflaton

strongly fixes  $\phi$  to the origin. In the classical background of an oscillating  $\phi$  field, the field  $X$  feels a large, oscillating, mass. This may lead to a period of non-perturbative, exponential production of vectors through parametric resonance (PR).<sup>2</sup> Particle production by PR is a well-studied phenomena, particularly in the context of reheating after inflation (so-called *preheating*) [65, 66, 67, 68]. However, vector production by PR has not been studied nearly as extensively as for scalars. PR production of gauge fields at the end inflation has been previously considered in [77, 78, 79], e.g. to seed primordial magnetic fields [80]. In addition, [78] and [79] also discuss the enhanced production of longitudinal modes. In this section we review the theory of PR for a vector, and show that the dynamics in our case depend delicately on the hierarchy between couplings  $e$  and  $\lambda$  and require a careful treatment of the transverse and longitudinal modes. We present the differential equation which governs the production of longitudinal modes that is distinct from the well-studied Mathieu and Lamé equations (the typical differential equations studied in the context of PR). The classes of solutions are presented in an instability chart of the exponentially growing momentum modes as a function of  $e/\lambda$ , and we compare the PR production of longitudinal and transverse modes in the different limits of interest. Ultimately we show that, as a consequence of both initial conditions set by inflation and a longitudinal mode enhancement in the coupling, the longitudinal mode dominates production for a wide range of couplings.

## Parametric Resonance for a Higgsed Vector

Using the conventional  $\text{diag}(1, -a^2, -a^2, -a^2)$  metric in an expanding universe, we can write the kinetic and mass term of  $X$  explicitly in terms of its temporal and spatial components:

$$\frac{1}{4}X_{\mu\nu}X^{\mu\nu} = \frac{1}{2} \left[ \frac{1}{a^2} |\partial_t \mathbf{X} + \nabla X_t|^2 - \frac{1}{a^4} |\nabla \times \mathbf{X}|^2 \right], \quad (3.13)$$

$$\frac{1}{2}\tilde{m}^2 X_\mu X^\mu = \frac{1}{2}\tilde{m}^2 \left( X_t^2 - \frac{1}{a^2} |\mathbf{X}|^2 \right), \quad (3.14)$$

where  $\tilde{m} \equiv m_X (1 + \phi/v)$ . Since  $X_t$  does not contain a kinetic term, it is an auxiliary field and can explicitly be integrated out using its equation of motion. Switching to  $k$ -space, we separate  $\mathbf{X}$  into its longitudinal and transverse components such that  $k \cdot \mathbf{X} = kX_L$  and  $\mathbf{k} \cdot \mathbf{X}_T = 0$ . As a result, the action for the vector field separates for the transverse and longitudinal components  $S = S_T + S_L$ :

$$S_T = \int dt \frac{a^3 d^3 k}{(2\pi)^3} \frac{1}{2a^2} \left( |\dot{\mathbf{X}}_T|^2 - (k^2/a^2 + \tilde{m}^2) |\mathbf{X}_T|^2 \right), \quad (3.15)$$

$$S_L = \int dt \frac{a^3 d^3 k}{(2\pi)^3} \frac{1}{2a^2} \left( \frac{\tilde{m}^2 a^2}{k^2 + \tilde{m}^2 a^2} \dot{X}_L^2 - \tilde{m}^2 X_L^2 \right). \quad (3.16)$$

---

<sup>2</sup>This is distinct from tachyonic resonance, which is an exponential instability that occurs for modes with a negative effective frequency-squared.

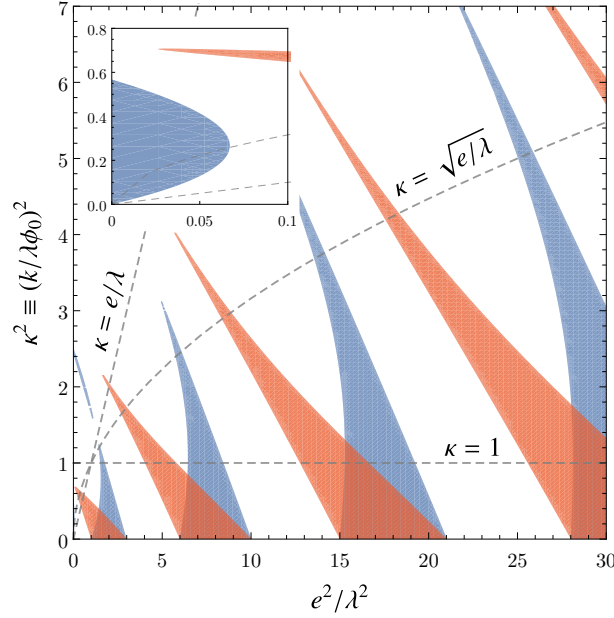


Figure 3.1: Instability charts of transverse (red) and longitudinal (blue) modes. The dashed lines represent different values of  $\kappa$ , and resonance bands above  $\kappa = e/\lambda$  correspond to relativistic production. In the inset we show the  $e/\lambda \ll 1$  limit in which the enhancement of longitudinal mode production over transverse modes is seen explicitly.

Note for here and throughout we use  $k$  to denote co-moving momentum.

We now study the PR production of the transverse and longitudinal modes. Exponentially growing modes naturally occur in specific resonance bands, and it is conventional to map out the regions of unstable momentum as a function of the couplings. The dominantly produced modes lie in the widest resonance band and generally have a large exponential instability, resulting in a rapid conversion of the energy density in the oscillating scalar field into these modes. We present the instability charts for the transverse and longitudinal modes in Fig. 3.1 and refer to it throughout—this is obtained by numerically solving the relevant equations of motions and identifying the choice of couplings that result in exponentially-growing solutions.

**Transverse Modes** It is convenient to switch to dimensionless, conformally invariant quantities: a time variable,  $dz \equiv \lambda\phi_0 dt/a$  as introduced in (3.7), a momentum  $\kappa \equiv k/\lambda\phi_0$ , and a conformal oscillating mass,  $\mu \equiv a\tilde{m}/\lambda\phi_0 = (e/\lambda)\text{cn}(z)$ . Doing so, the equation of motion for transverse modes becomes:

$$\mathbf{X}_T'' + (\kappa^2 + \mu^2(z)) \mathbf{X}_T = 0. \quad (3.17)$$

This equation is known as the Lamé equation and has been extensively studied in the literature (see e.g. [81]).<sup>3</sup> Solutions to this equation are exponentially growing for certain momentum modes  $\mathbf{X}_T \propto e^{\mu_\kappa z}$ . The characteristic exponents,  $\mu_\kappa$ , are a non-trivial function of momentum as well as the ratio of couplings. PR is often classified as either broad or narrow, based on the width of resonance bands and the size of the characteristic exponents. For the mode equation of (3.17), the resonance is broad if  $e \gg \lambda$  and narrow if  $\lambda \gg e$ . We will be interested in both these limits, which have previously been solved analytically.

In the case of  $\lambda \gg e$  the first resonance band around  $\kappa^2 \simeq 1$  dominates production while subsequent resonance bands (at larger  $\kappa$ ) become increasingly narrow. Such narrow resonances are known to have suppressed production with a small range of produced momenta and characteristic exponents,  $\Delta\kappa^2, \mu_\kappa \propto e^2/\lambda^2$ . Thus we conclude production of transverse modes is not efficient in this regime. For  $e \gg \lambda$  the resonance is instead broad and can achieve much more efficient production. Inspection of Fig. 3.1 shows that the structure of the resonance, in particular the size of  $\kappa$  in the first resonance band, depends critically on the value of  $e/\lambda$ . Interestingly, it is still the case that for  $e \gg \lambda$  there is an upper bound on the produced momentum which can be estimated analytically [81]. A necessary condition for exponential instability in the regime of broad PR is non-adiabatic change in the frequency of fluctuations. The (dimensionless) frequency felt by the transverse modes is  $\omega(t) \simeq \sqrt{\kappa^2 + (e/\lambda)^2 \text{cn}^2(z)}$ . If one defines an adiabatic parameter  $R \equiv |\omega'|/\omega^2$ , then for most of the oscillation period this is close to zero and the frequency changes adiabatically. The only time  $R > 1$  is when the background field oscillates toward zero,  $\text{cn}(z) \rightarrow 0$  and  $\kappa^2 \lesssim e/\lambda$ , which is an estimate of the upper bound on the dominantly produced momenta. In fact this bound is evident in Fig. 3.1, where the widest resonance band (red) always lies below the line  $\kappa = \sqrt{e/\lambda}$ . We thus find that the typical physical momenta produced by PR here is much less than the time-averaged mass of the vector,  $\sim e\phi_0$ , and vectors are produced non-relativistically. We compute the maximum characteristic exponent numerically for  $e \gg \lambda$  and find  $\mu_\kappa \simeq 0.2$ , in agreement with the previous literature [81].

**Longitudinal Mode** PR for the transverse modes reduce to equations that have been solved extensively in the literature. We now move to the longitudinal mode which, as we will show, dominates the production of vectors in a wide range of parameters. Starting from (3.16) and making the transformations to conformal fields, we find the equation of motion:

$$X_L'' + \frac{2\kappa^2}{\kappa^2 + \mu^2} \frac{\mu'}{\mu} X_L' + (\kappa^2 + \mu^2) X_L = 0. \quad (3.18)$$

The dynamics governed by this differential equation have not been studied in great detail in the literature. Here we present a brief analysis, and leave an extensive study for future work.

---

<sup>3</sup>As long as the scalar oscillations are well approximated by the harmonic approximation, the solutions are the same as those of the well-known Mathieu equation.



First we note that in the limit  $\kappa \rightarrow 0$ , the equation of motion (3.18) reduces to precisely that of the transverse modes:

$$X_L'' + (\kappa^2 + \mu^2)X_L \simeq 0. \quad (3.19)$$

This is expected, since at low energies the longitudinal mode can no longer be distinguished from the transverse modes and should obey the same dynamics. We also see this directly in Fig. 3.1, where the resonance bands of the two modes roughly coincide (except for very particular values of the couplings) in the limit of small momentum  $\kappa \ll 1$ .

The high energy limit is more challenging to analyze since the physics is obscured by a divergence in the friction term as the oscillating field passes through the origin. While it is in principle possible to solve the equation as is, it is simpler to introduce a field redefinition,

$$\pi \equiv \frac{\mu}{\kappa} X_L. \quad (3.20)$$

Being a linear transformation, this does not mix the different momentum modes and hence does not obscure the structure of the resonance. The resulting equation of motion is:

$$\pi'' - \frac{2\mu\mu'}{\kappa^2 + \mu^2}\pi' + \left(-\frac{\mu''}{\mu} + \frac{2\mu'^2}{\kappa^2 + \mu^2} + \kappa^2 + \mu^2\right)\pi = 0. \quad (3.21)$$

If we then take the high-energy limits,  $\kappa \gg \mu$  and  $\mu \ll 1$ , we recover a familiar form:

$$\pi'' + (\kappa^2 + \text{cn}^2(z))\pi \simeq 0. \quad (3.22)$$

This is analogous to the equation of motion for transverse modes (3.17), though crucially the amplitude of the oscillations is enhanced by a factor  $\lambda^2/e^2$ . As a result, the PR dominantly produces longitudinal modes with  $\kappa^2 \simeq 1$ , which can also be seen directly in the inset of Fig. 3.1 where there is a wide instability band (blue) for the longitudinal mode in the limit  $e/\lambda \rightarrow 0$ . This result in the high-energy limit can also be derived directly from the action of the dark Higgs  $\varphi$  using the Goldstone boson equivalence theorem. Expanding  $\varphi = (\phi + v + i\chi)/\sqrt{2}$  and switching to conformal fields, we find the same equation of motion for  $\chi$  as found for the longitudinal mode in this limit (3.22).

We are now in a position to complete the discussion of PR for the longitudinal mode as a function of the couplings. Firstly we consider the limit of  $\lambda \gg e$  (where we found the transverse modes are not efficiently produced). In this case the longitudinal mode is produced strictly in the high-energy regime  $\kappa \gg \mu$ , and the results follow the approximate form of the mode equation (3.22). Here we find the resonance is efficient for  $\kappa^2 \simeq \Delta\kappa^2 \simeq 1$  and we again have a large characteristic exponent  $\mu_\kappa \simeq 0.1$ . We emphasize that, in contrast to the transverse modes, the longitudinal mode has a marginally narrow resonance allowing it to be produced efficiently. In addition, the longitudinal modes are produced highly boosted with relativistic momenta. We now turn to the limit  $e \gg \lambda$  which is much more interesting. Although the mode equations become identical in the limit  $\kappa \ll 1$ , PR production only occurs when the vector mass is rapidly varying (i.e. when adiabaticity is violated). At this point  $\kappa$  is of order the oscillating mass  $\mu$ , and the longitudinal mode equation (3.18)



does not approximately reduce to any well-known forms (due to the non-negligible friction term). Indeed, as is evident from Fig. 3.1, there are substantial differences between the resonance structures of the longitudinal and transverse modes in this regime. While the solutions for the longitudinal mode similarly suggest an upper bound on the dominantly produced momenta, the bound may be larger than that of the transverse modes depending on the coupling. This is an intriguing feature that opens up the possibility of producing relatively boosted longitudinal modes, although we still expect that the momenta in the first resonance bands satisfy  $\kappa^2 < e/\lambda$  such that produced modes are not relativistic. Finally, we compute the typical characteristic exponent for longitudinal mode production in this limit to be  $\mu_\kappa \simeq 0.2$ .

**$\phi$  Fluctuations** In addition to vector production, an oscillating  $\phi$  field will inevitably also resonantly produce  $\phi$  fluctuations with non-zero momentum (denoted as  $\delta\phi$  to differentiate from the zero-momentum condensate which we continue to denote by  $\phi$ ) from the self-coupling,  $\lambda$ . We emphasize that these excitations are in addition to the zero-mode condensate that results from coherent oscillations and carry a particle interpretation similar to the vector fluctuations. The mode equation can be derived from (3.5) by restoring the momentum term and expanding the field as  $\phi + \delta\phi$ , keeping order linear terms in the fluctuations. The resulting equation of motion is identical to that of the transverse modes (3.17) but with the replacement  $e^2 \rightarrow 3\lambda^2$ :

$$\delta\phi'' + (\kappa^2 + 3\text{cn}(z)^2) \delta\phi = 0. \quad (3.23)$$

The PR is qualitatively similar to that of the longitudinal mode in the  $\lambda \gg e$  case (3.22). Fluctuations of  $\phi$  are dominantly produced at momentum  $\kappa^2 \simeq 1$  with a width  $\Delta\kappa^2 \simeq 1$  and (slightly smaller) characteristic exponent  $\mu_\kappa \simeq 10^{-2}$ .

**Initial Conditions** We have seen that due to parametric resonance, there is an exponential amplification of fluctuations in the fields  $X$  and  $\phi$  for certain momentum modes. However, an important effect we have yet to address are the initial conditions for the fields. Assuming a period of inflation, we can estimate the initial conditions for each field. Transverse components of the vector are conformally invariant and do not experience the expansion suggesting that they should have an initial field value given by the Bunch-Davies vacuum with a power spectrum,  $P_T(k) \sim k^2$ . The initial conditions of the longitudinal mode are more dramatic. These are created by coupling to the metric during inflation and can far exceed their transverse counterparts [63] with a power spectrum,  $P_L(k) \sim (H_{\text{inf}}k/e\phi_0)^2$  (this applies for both  $\lambda \gg e$  and  $e \gg \lambda$  and assumes the vector mass during inflation is  $e\phi_0$ ). This gives a ratio of the longitudinal to transverse mode amplitudes at the end of inflation as,

$$\frac{X_L(k)}{X_T(k)} \gtrsim \frac{H_{\text{inf}}}{e\phi_0}, \quad (3.24)$$

which is independent of  $k$ . Since we do not consider parameter space such that the vector mass is above the scale of inflation, the longitudinal mode will dominate the transverse

mode production as long as they can both be produced efficiently. The scalar fluctuations during inflation behave similarly to the longitudinal mode and will have comparable initial conditions.

## Final Relic Abundance and Momenta

The exponential production from PR does not last indefinitely. Thus far we have neglected the non-linear back reaction of these fluctuations on PR itself. There are three kinds of back reactions:

(1) The vector and scalar fluctuations grow large enough and give large mass contributions to both  $\phi$  and  $X$  that subsequently red-shift as  $\propto 1/a$ , and can lead to other interesting cosmological effects that will be discussed later. Here, we see that a changing mass acts to shift the resonance bands and can thus ruin the important Bose enhancement in final states that leads to continued exponential production for growing modes.

(2) Scattering of fluctuations with the zero-mode condensate as well as fluctuations shift the particle momenta out of resonance bands. Again, this destroys the Bose enhancement in produced fluctuations and can also shut down exponential production.

(3) The scattering also depletes the zero-mode condensate and terminates PR.

A fourth effect, due to the expansion, is not present in this theory due to its conformal nature. In practice these effects occur simultaneously and act to cease particle production when the energy density of the fluctuations becomes comparable to the original energy density in the condensate. While these effects are highly non-linear and challenging to compute, if particle production lasts long enough the condensate will completely convert into the produced  $\phi$  and  $X$  particles, regardless of the detailed processes involved. We assume that the zero-momentum field is completely depleted and does not make up any of the DM today (we expect this is a reasonable approximation due to significant scattering with produced fluctuations at the end of PR). In this sense, a full solution to the equations of motion, including back reactions, gives us the relative fraction in these two populations. We can parameterize the yields after the conclusion of PR production as:

$$Y_X = f \frac{\rho_{\phi, \text{osc}}}{E_X s(T_{\text{osc}})}, \quad Y_{\delta\phi} = (1 - f) \frac{\rho_{\phi, \text{osc}}}{E_{\delta\phi} s(T_{\text{osc}})}. \quad (3.25)$$

Here  $\rho_{\phi, \text{osc}} = \frac{1}{4} \lambda^2 \phi_0^4$ ,  $f$  is the relative fraction of the condensate co-moving energy density dumped into vectors, and  $E_i^2 = \sqrt{k_{*,i}^2 + m_i^2}$  are the co-moving energies of the particle species  $i$  ( $m_i$  denotes the time-varying mass of the particle). For simplicity, we assume particles are produced with a co-moving momenta peaked at  $k_{*,i}$  though in practice there will be small corrections associated with an  $\mathcal{O}(1)$  spread around this typical value.

Once PR stops being efficient the produced particles are in a highly non-equilibrium state with peaked momenta. These particles can still undergo collisions within the sector scattering their momenta and changing their number densities. This includes simple  $2 \rightarrow 2$  elastic scattering as well inelastic processes inducing cannibalization. Tracking the dynamics

rigorously throughout this “post-scattering” phase requires a dedicated computation putting vectors and scalars on lattices and is beyond the scope of this work. However, we can still qualitatively estimate the behavior in each limit.

For  $\lambda \gg e$ , the longitudinal mode and the fluctuations only differ by their parity and hence have comparable energy densities after decay ( $f \simeq 1/2$ ) as well as momenta  $k_* \sim \lambda\phi_0$ . In this limit, the symmetry between the longitudinal mode and the fluctuations of  $\phi$  allows us to treat them as a single fluid regardless of the details of the post-scattering phase. Furthermore, we do not expect these processes to be active even if either species becomes non-relativistic. We thus expect that the vectors and scalars should have comparable number densities and momenta at late times:

$$Y_X, Y_{\delta\phi} \rightarrow \frac{1}{2} \frac{\rho_{\phi,\text{osc}}}{\lambda\phi_0 s(T_{\text{osc}})} . \quad (3.26)$$

For  $e \gg \lambda$ , the situation is more subtle. As shown, vectors are primarily produced non-relativistically from PR (a detailed spectrum will depend on the coupling  $e/\lambda$ ), while fluctuations of  $\phi$  are produced mildly relativistically. At this point, elastic and inelastic processes are efficient in driving the sector toward a state equating the momenta and number densities of  $X$  and  $\phi$  ( $f \simeq 1/2$ ). Effective scattering during this time relies on a Bose enhancement of the final state which is spoiled at large enough momenta. We estimate that such processes cannot produce vectors with momenta larger than their mass  $e\phi_0$ , and as a result both species should eventually be up-scattered to a co-moving momenta as large as  $k_* \sim e\phi_0$ . We thus expect yields of  $X$  and  $\phi$  at late times of order:

$$Y_X, Y_{\delta\phi} \rightarrow \frac{1}{2} \frac{\rho_{\phi,\text{osc}}}{e\phi_0 s(T_{\text{osc}})} . \quad (3.27)$$

We have confirmed this expectation employing a lattice computation using LATTICEEASY [82] and approximating the vector interaction by that of a scalar field with a quartic coupling to  $\phi$ .

### 3.4 Vector Dark Matter from Parametric Resonance

The above results apply for any Higgsed vector in the early universe, and we now consider the implications of PR for the production of ultralight vector DM. For the rest of this section, we assume a large initial field value  $\phi_0 \gtrsim v$ . In practice, PR production is not instantaneous but requires sufficiently long exponential growth so we in fact have the condition  $\phi_0/v \gtrsim 10\text{--}100$ .<sup>4</sup>

There are four (a priori) independent parameters in the model:  $\{\phi_0, v, m_X, m_\phi\}$  or alternatively  $\{\phi_0, v, e, \lambda\}$ . As we have seen, the nature of PR depends on the relative strengths of the couplings in a non-trivial way. This is also true for the resulting constraints on safely

---

<sup>4</sup>A stable PR still occurs even if  $\phi_0 \lesssim v$  in the case  $\lambda \gg e$ , but this is a narrow resonance and highly inefficient.

obtaining the correct relic abundance of vector DM. Thus we look at the two simplifying limits separately:  $\lambda \gg e$  and  $e \gg \lambda$ . Here we focus on the fundamental challenge of being consistent with constraints on warm DM while producing the entire DM abundance. Additional constraints and phenomenological consequences of the vector production are examined in Sec. 3.5, which we refer to in the results of Fig. 3.2 and 3.3.

### Case 1: $\lambda \gg e$

We begin with the case where the gauge coupling is small with respect to the quartic (and hence also  $m_X \ll m_\phi$ ). In Sec. 3.3 we estimated a yield for the  $X$  and  $\phi$  fluctuations to be roughly equal at late times:

$$Y_X \simeq Y_{\delta\phi} \simeq \frac{0.01}{\lambda^{1/2}} \left( \frac{\phi_0}{M_{\text{pl}}} \right)^{3/2}. \quad (3.28)$$

In the absence of any additional interactions these yields are conserved until today. Once  $X$  and  $\phi$  become non-relativistic,  $X$  constitutes a small fraction of the energy density of the dark sector:

$$\frac{\Omega_X}{\Omega_{\text{DM}}} \simeq \frac{m_X}{m_\phi} \sim \frac{e}{\lambda}. \quad (3.29)$$

Furthermore, the typical co-moving momenta of each species is of order  $k_* \sim \lambda\phi_0$ . This is related to the physical momenta by red-shifting from the time of production. Crucially, particles are produced from PR at very early times near the start of oscillations. Due to the conformal invariance, we can effectively treat the yields (3.35) as being produced with a physical momenta  $\lambda\phi_0$  at a temperature  $T_{\text{osc}}$  even if the particles are dominantly created somewhat later (PR results in rapid, through not instantaneous, particle creation).

Given the relative energy densities between the scalar and vector, it is most natural that the dark Higgs constitutes nearly all of the DM today, with the vector being a subdominant component. In order for this scenario to be consistent with observations we require the dark Higgs be both non-relativistic by around a keV and satisfy the relic density condition. Requiring the dark Higgs yield to be the right relic abundance fixes the required initial field value:

$$\frac{\phi_0}{M_{\text{pl}}} \simeq 10 \left( \frac{\lambda T_{\text{eq}}^2}{m_\phi^2} \right)^{1/3}. \quad (3.30)$$

The temperature at which the Higgs becomes non-relativistic is given by

$$T_{\text{NR}} \simeq v \left( \frac{\lambda M_{\text{pl}}}{\phi_0} \right)^{1/2} \simeq 0.5 \left( \frac{v^2 m_\phi^2}{T_{\text{eq}}} \right)^{1/3}. \quad (3.31)$$

If the fraction of vector DM is greater than a few percent, it must also be sufficiently cold; otherwise, the relic vectors will be a hot DM subcomponent which is ruled out by the cosmic microwave background [76]. We show the viable parameter space for a vector subcomponent

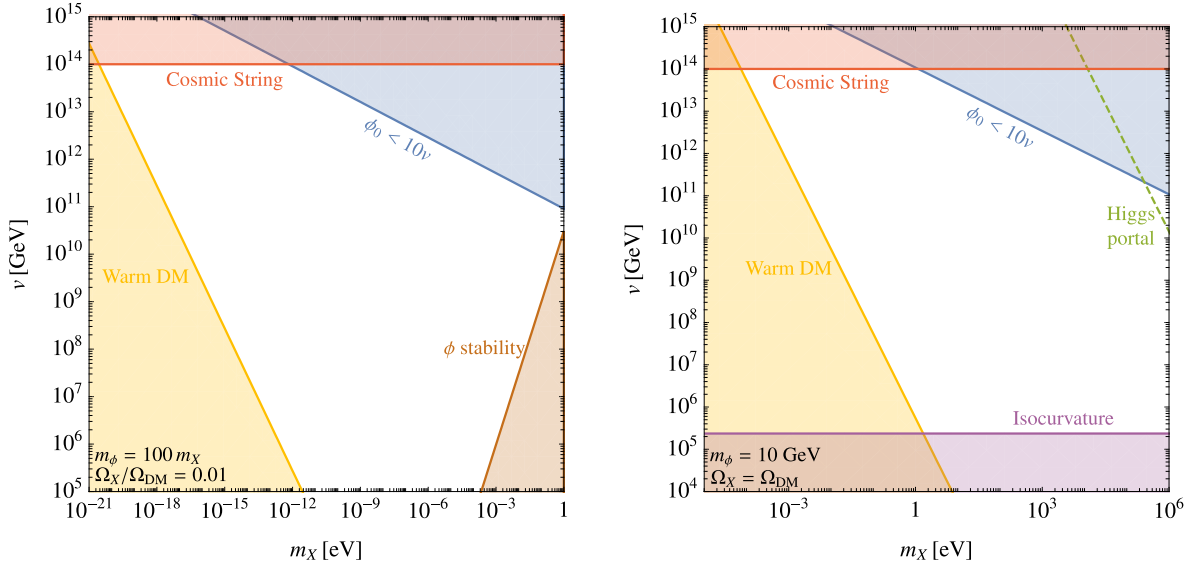


Figure 3.2: Viable parameter space for parametric resonance production of vectors in the limit  $\lambda \gg e$ . We fix the initial condensate amplitude  $\phi_0$  such that the dark sector saturates the DM relic abundance  $\Omega_X + \Omega_\phi \simeq \Omega_{\text{DM}}$ . Shown are constraints from coldness (yellow), cosmic strings (red), isocurvature (purple), late time dark Higgs decays (brown) and sufficiently long PR (blue) as described in the text. **Left:** At every point in parameter space we fix  $m_\phi \simeq 100 m_X$ . We do not incorporate any additional interactions, and the dark Higgs makes up nearly all the DM, i.e.  $\Omega_X \simeq 10^{-2} \Omega_\phi$ . **Right:** Vectors make up all of the DM, and the dark Higgs is eliminated at late times. At every point in parameter space we fix  $m_\phi = 10$  GeV and show the corresponding constraint from thermalization requirements (green) as described in Appendix C.

of DM in Fig. 3.2 (left), fixing the fraction of vector DM to be  $10^{-2}$  (with the rest made up by the dark Higgs).

Even if vectors make up a small fraction of the DM abundance, they may still be detectable. Nevertheless, it is interesting to consider the possibility that vectors make up all of the DM due to some dynamics which eliminated the dark Higgs yield at later times. In particular, it is possible to introduce additional couplings to the model that drastically alter the expected relic abundance of dark Higgses, without affecting the abundance of vectors produced from PR. (Although we might have naively suspected that the large initial yield of  $\phi$  particles could simply decay away to vectors through the perturbative process (3.10), such population of vectors constitutes an  $\mathcal{O}(1)$  hot DM component.) For now we will take it as a given that  $Y_X$  reproduces the entire observed DM density. This fixes the initial field

value:

$$\frac{\phi_0}{M_{\text{pl}}} \simeq 10 \left( \frac{\lambda T_{\text{eq}}^2}{m_X^2} \right)^{1/3}. \quad (3.32)$$

The  $X$  population becomes non-relativistic when the universe is at a temperature:

$$T_{\text{NR}} \simeq m_X \left( \frac{M_{\text{pl}}}{\lambda \phi_0} \right)^{1/2} \simeq 0.5 \left( \frac{m_X^4}{T_{\text{eq}} \lambda^2} \right)^{1/3}. \quad (3.33)$$

As before, we require  $T_{\text{NR}} \gtrsim \text{keV}$ . Note that the initial field amplitude has a maximum value consistent with the vector DM abundance and coldness constraints:

$$\phi_0 \simeq 10 M_{\text{pl}} \left( \frac{T_{\text{eq}}}{T_{\text{NR}}} \right)^{1/2} \lesssim 2 \times 10^{17} \text{ GeV}. \quad (3.34)$$

This makes the condition on oscillation during radiation-domination ( $\phi_0 < M_{\text{pl}}$ ) trivially satisfied.

We now return to the elimination of the dark Higgs yield in the above scenario. If we assume the vector constitutes all of DM as per (3.32), then to avoid the dark Higgs dominating the energy density of the universe at an intermediate time the yield should have been destroyed by the temperature  $\sim T_{\text{eq}} m_\phi / m_X$ . This is not a constraint, though a necessary condition for the above formula to hold as they assume radiation domination throughout. If, on the other hand, the universe has gone through a period of dark Higgs domination that later gets dumped into the SM this could have profound implications on small scale structure [83, 84, 85] and changes the predicted relic abundances. If we assume this matter-dominated era lasts until the dark Higgs reheats the universe to a temperature  $T_{\text{R}}$ , the resulting entropy production dilutes the yield of relic vectors  $Y_X \sim T_{\text{R}} / m_\phi$ . A concrete example of the such a cosmology occurs if the dark Higgs is able to thermalize with the SM. This generically requires the dark Higgs to have a substantial coupling to the SM, and as a result the allowed mass range of  $\phi$  will be subject to experimental constraints. The simplest interaction of the dark Higgs with the SM is a Higgs-portal coupling. As we show in Appendix C, this has severe constraints from star cooling and rare meson decays below around 5 GeV. We show the viable parameter space for vector DM production in Fig. 3.2 (right), assuming the large dark Higgs yield is eliminated at late times before dominating the energy density of the universe. Here we fix the dark Higgs mass to be  $m_\phi = 10 \text{ GeV}$  and show the requirements on dark Higgs thermalization through the Higgs portal interaction, leaving a detailed examination of the necessary conditions to Appendix C. We do not explicitly show the parameter space for vector DM production in the case of dark Higgs domination though we have checked the lower reach in  $m_X$  is ultimately the same as that in the case of no entropy production.

## Case 2: $e \gg \lambda$

We now turn to the limit where the gauge coupling is much larger than the quartic (and so  $m_X \gg m_\phi$ ). Due to the effects of post-scattering, the co-moving number densities of  $\phi$  and

$X$  at late again become comparable and are given by,

$$Y_X \simeq Y_{\delta\phi} \simeq \frac{\lambda}{e} \frac{0.01}{\lambda^{1/2}} \left( \frac{\phi_0}{M_{\text{pl}}} \right)^{3/2}. \quad (3.35)$$

This difference in mass of  $\phi$  and  $X$  leads to vectors dominating the energy density at late times, and the dark Higgs becomes a subdominant component with a fractional abundance  $\lambda/e$ . In addition, vectors are produced non-relativistically with typical co-moving momentum  $k_* \lesssim e\phi_0$ , while the dark Higgses are dominantly produced from vector fluctuations with a similar spectrum and are thus highly relativistic.

The observed DM abundance is reproduced for the initial field amplitude of

$$\frac{\phi_0}{M_{\text{pl}}} \simeq 10 \left( \frac{e^2 T_{\text{eq}}^2}{\lambda m_X^2} \right)^{1/3}. \quad (3.36)$$

The temperature at which the vectors become non-relativistic is given by:

$$T_{\text{NR}} \simeq 2m_X \left( \frac{M_{\text{pl}}\lambda}{\phi_0 e^2} \right)^{1/2} \simeq 0.5 \left( \frac{m_X^4 \lambda^2}{T_{\text{eq}} e^4} \right)^{1/3}. \quad (3.37)$$

Note that by  $T_{\text{NR}}$ , the vector mass (initially dominated by fluctuations of  $\phi$  after PR) assumes the vacuum value. Since the vector makes up most of the DM, we require the coldness constraint  $T_{\text{NR}} \gtrsim \text{keV}$ . On the other hand, if the fraction of produced dark Higgses is roughly greater than  $10^{-2}$ , then this subdominant component must also be sufficiently cold.

We show the viable parameter space for vector DM production in Fig. 3.3 for  $e/\lambda = 10$  (left) and  $e/\lambda = 10^3$  (right), with the value of  $\phi_0$  fixed at every point to achieve the correct relic abundance. For  $e/\lambda = 10$  the dark Higgs is a non-negligible subcomponent and in addition to the vectors being sufficiently cold we also require the dark Higgs is non-relativistic by a keV, while for  $e/\lambda = 10^3$  we only require that the vector population satisfies the coldness constraint (3.37). The lowest possible vector masses can be obtained by saturating  $e \rightarrow \lambda$  where we find we can produce cold DM for  $m_X \gtrsim 10^{-18} \text{ eV}$  (though saturating this limit results in the vectors being accompanied by non-negligible dark Higgs abundance).

## 3.5 Phenomenology

In this section, we summarize some distinctive features of vector production through parametric resonance which could be used to differentiate it from other non-thermal cosmologies.

**Dark Higgs** Perhaps the most prominent prediction of PR production would be searching directly for the accompanying light scalar. The detectability of the scalar depends on its model-dependent coupling (if any) to the SM, and in general no such coupling is required to produce vectors. However, if  $\lambda \gg e$  than the scalar is either a large fraction of the DM abundance today, or the scalar is destroyed by some additional mechanism (e.g. thermalization



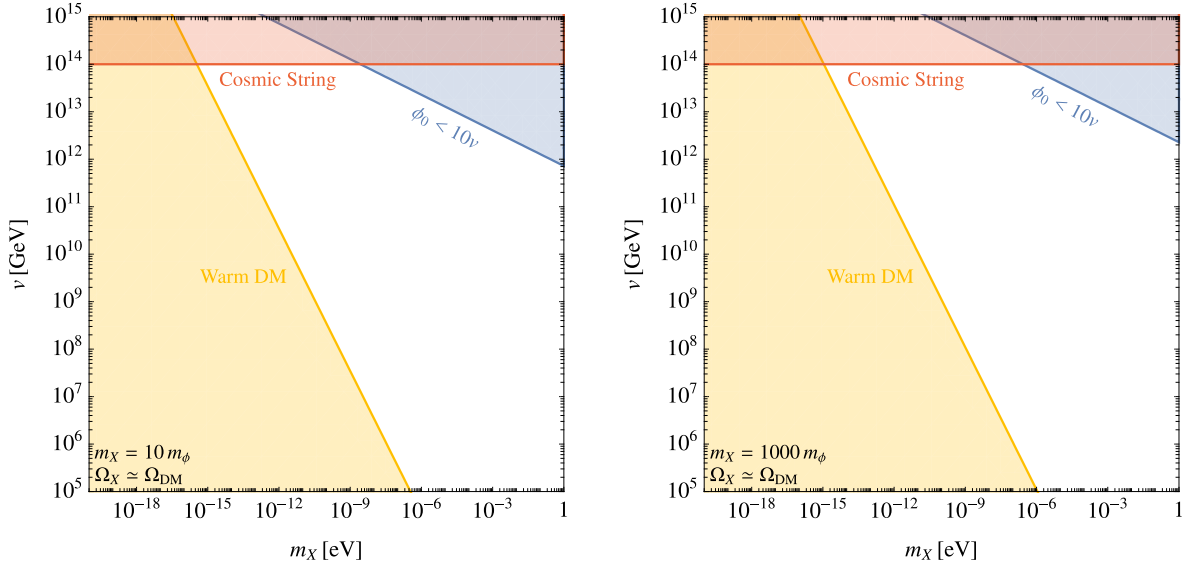


Figure 3.3: Viable parameter space for parametric resonance production of vectors in the limit  $e \gg \lambda$ . We fix the initial condensate amplitude  $\phi_0$  such that the dark sector saturates the DM relic abundance  $\Omega_X + \Omega_\phi \simeq \Omega_{\text{DM}}$ . Shown are constraints from coldness (yellow), cosmic strings (red), and sufficiently long PR (blue) as described in the text. Both plots have the vector making up nearly all the DM. **Left:** At every point in parameter space we fix  $m_X \simeq 10 m_\phi$  and thus  $\Omega_\phi \simeq 10^{-1} \Omega_X$ . **Right:** At every point in parameter space we fix  $m_X \simeq 1000 m_\phi$  and thus  $\Omega_\phi \simeq 10^{-3} \Omega_X$ .

with the SM) so that vectors make up all of the observed DM abundance. If the scalar is a non-negligible relic today then it could be searched for directly through experiments sensitive to light scalars. Furthermore, if it dominates the DM density then it could be observed as a (cosmologically slow) dark decay into the vectors from anomalous changes of equation of state of the universe [86]. The current consistency with the  $\Lambda$ CDM picture allows us to set a bound on this decay rate as given in Fig. 3.2.

Alternatively, if the dark Higgs is assumed to thermalize with the SM then the minimal required coupling to achieve thermalization sets a convenient target for experimental searches. We study these specific requirements in the context of a Higgs portal coupling in Appendix C.

**Cosmic Strings** As we have seen, PR produces large quantum fluctuations in the  $X$  and  $\phi$  fields. These fluctuations can lead to a large positive effective mass for  $\phi$  resulting in the symmetry being temporarily restored once PR terminates and a subsequent non-thermal phase transition once the mass of  $\phi$  becomes negative [87]. This has an intriguing prediction of the formation of cosmic strings [88]. Cosmic strings are one-dimensional topological de-



fects, characterized by a string tension  $\mu \sim v^2$ . After formation, it is expected that the string network quickly approaches a scaling regime, i.e., energy density in strings scales with the energy density of the universe but roughly suppressed by the factor  $G\mu$ , where  $G = 1/8\pi M_{\text{pl}}^2$  is Newton's constant. Such strings have several characteristic predictions owing to their induced large energy gradients in the universe. Perhaps the most robust detection of cosmic strings can be extracted from the cosmic microwave background, whose gravitational interaction would induce small temperature distortions leading to inhomogeneities in the temperature map [89]. Using the WMAP data with a combination of cosmological observations such strings have yet to be observed, putting a constraint  $G\mu \lesssim 10^{-7}$  [90].

An additional prediction of cosmic strings comes from gravitational radiation emitted by the string oscillations. The evolution of a scaling cosmic string network is expected to contribute to the stochastic gravitational wave background [91] as well as induce gravitational wave bursts [92]. This is contrast to global strings, which predominantly radiate massless Goldstone bosons (e.g., axion strings). The gravitational wave spectrum from a cosmic string network can be computed, under basic assumptions. The, thus far, null observation of a stochastic gravitational wave background by LIGO and pulsar timing arrays constrain  $G\mu \lesssim 10^{-11}$  [93, 94, 95], which roughly translates to a bound on the VEV  $v \lesssim 10^{14}$  GeV. Future pulsar timing array measurements are expected to have improved sensitivity with the upcoming future Square Kilometer Array [96] and provide an opportunity to probe these non-thermal phase transitions.

**Isocurvature Perturbations** Another prediction of this production mechanisms is due to the lightness of the dark Higgs, inducing isocurvature perturbations in the cosmic microwave background (CMB). During inflation, we presume  $\phi$  is stuck with an initial field amplitude obeying  $\lambda\phi_0 \lesssim H_{\text{inf}}$ , and fluctuations,  $\delta\phi \sim H_{\text{inf}}/2\pi$ . During PR the energy density of the  $\phi$  condensate is transferred to the observed DM abundance and instills these isocurvature perturbations in the DM spectrum. These perturbations can be looked for in the CMB though they have yet to be seen [64]. This can be interpreted as a bound on the Hubble scale during inflation  $H_{\text{inf}} \lesssim 3 \times 10^{-5} \phi_0$ , which in the simplest picture suggests a bound  $\lambda \lesssim 3 \times 10^{-5}$ . This puts a relevant constraint for  $\lambda \gg e$  if the dark Higgs is required to thermalize with the SM but turns out to be negligible when we do not enforce this requirement. We note that, in principle, this isocurvature perturbation can be suppressed if the Hubble induced mass of  $\phi$  is larger than  $H_{\text{inf}}$ .

## 3.6 Discussion

In this work we present a new production mechanism for vector DM in the early universe through its (possible) coupling to a dark Higgs. The mechanism relies on the non-perturbative dynamics associated with parametric resonance, thus allowing the produced vectors to be ultralight while still being consistent with the stringent constraints on warm DM.

Vector production from parametric resonance has qualitative differences from the well-studied theory of scalar production. We study the equations governing the PR production of transverse and longitudinal modes and present an instability chart. For  $\lambda \gg e$  the transverse mode production is highly inefficient while the longitudinal mode is rapidly produced (this can be understood as a consequence of the Goldstone boson equivalence theorem). Fluctuations of dark Higgses are also produced which results in a Higgs-dominated dark sector. In order for vectors to make up the entire DM abundance, additional interactions can be considered to thermalize the dark Higgs with the visible sector. We find produced vectors can be as light as  $10^{-20}$  eV if they form 1% of the energy density in DM (with the dark Higgs making up the rest). If, on the other hand, we require the dark Higgs to thermalize with the SM it is difficult to foresee a viable model without making the dark Higgs heavier than around 10 GeV (otherwise there are tight constraints on its coupling). This restricts the produced vector DM to having masses above around  $10^{-4}$  eV. In the case where  $e \gg \lambda$  both the transverse and longitudinal mode can be efficiently produced, though as a consequence of initial conditions set by inflation we still expect the longitudinal mode to dominate for a wide range of parameters. As in the previous case fluctuations of  $\phi$  are rapidly produced resulting in comparable number densities between vectors and dark Higgs, although due to the ratio of masses the DM energy density today is dominated by vectors. Ultimately, the coldness constraint restricts the viable vector DM mass to be above  $10^{-18}$  eV.

Our study of PR production of ultralight vectors was not meant to be exhaustive, and we conclude by commenting on directions we feel merit further attention. Firstly, the focus of this work was entirely on vectors which get their mass from a dark Higgs. In principle, this could easily be generalized to other types of scalars which obtain a large field value. Secondly, in this work we did not attempt a complete lattice simulation of the non-linear effects. This would be particularly important in the limit of  $e \gg \lambda$  since in this case it is possible that the coldness constraint is significantly weakened if the vectors do not get boosted to their maximum possible momenta,  $e\phi_0$ . Furthermore, it is important to note that a general feature of this framework is the necessity for tiny couplings (for the mass range in the  $e \gg \lambda$  case, gauge couplings in the viable parameter space go down to as low as  $\sim 10^{-40}$ ). While such couplings are technically natural, it would be interesting to see how viable these are in a UV model. Lastly, in this work we briefly explored the prominent phenomenological signatures of this production mechanism though it may be fruitful to consider these in more detail as well as others to differentiate PR production from other possible production mechanisms.

*Note Added:* During the preparation of this work, we became aware of [97], [98], and [99]—these all discuss possible production of light vector DM from an oscillating axion field via the tachyonic instability.

# Chapter 4

## White Dwarfs as Dark Matter Detectors

### 4.1 Introduction

Identifying the nature of dark matter (DM) remains one of the clearest paths beyond the Standard Model (SM) and it is thus fruitful to study the observable signatures of any yet-allowed DM candidate. Many direct detection experiments are designed to search for DM, e.g. [100, 101], yet these lose sensitivity to heavier DM due to its diminished number density. Even for a strongly-interacting candidate, if the DM mass is above  $\sim 10^{22}$  GeV a terrestrial detector of size  $\sim (100 \text{ m})^2$  will register fewer than one event per year. While these masses are large compared to those of fundamental particles, it is reasonable to suppose that DM may exist as composite states just as the SM produces complex structures with mass much larger than fundamental scales (e.g., you, dear reader). Currently there is a wide range of unexplored parameter space for DM candidates less than  $\sim 10^{48}$  GeV, above which the DM will have observable gravitational microlensing effects [102]. For such ultra-heavy DM, indirect signatures in astrophysical systems are a natural way forward. One such signal first proposed in [103] is that DM can trigger runaway fusion and ignite type Ia supernovae (SN) in sub-Chandrasekhar white dwarf (WD) stars.

In addition to constraining the properties of DM, this raises the intriguing possibility that DM-induced runaway fusion is responsible for a fraction of observed astrophysical transients. The progenitors of type Ia SN are not fully understood [104], and recent observations of sub-Chandrasekhar [105, 106], hostless [107], and unusual type Ia SN [108] suggest that multiple progenitor systems and ignition mechanisms are operative. Other suspected WD thermonuclear events, such as the Ca-rich transients [109], are also poorly understood. While mechanisms for these events have been proposed [110, 111, 112, 113], the situation is yet unclear and it is worthwhile to consider new sources of thermonuclear ignition.

Runaway thermonuclear fusion requires both a heating event and the lack of significant cooling which might quench the process. The WD medium is particularly suited to this as

it is dominated by degeneracy pressure and undergoes minimal thermal expansion, which is the mechanism that regulates fusion in main sequence stars. Thermal diffusion is the primary cooling process in a WD, and it can be thwarted by heating a large enough region. The properties of a localized heating necessary to trigger runaway fusion were computed in [114]. Consequently, it was realized [103] that if DM is capable of sufficiently heating a WD in this manner, it will result in a SN with sub-Chandrasekhar mass progenitor. This was used to place limits on primordial black holes which transit a WD and cause heating by dynamical friction, although the authors of [103] identify several other heating mechanisms which may be similarly constrained. Note that the idea of using observations of WDs to constrain DM properties has been pursued before, e.g. through an anomalous heating of cold WDs [115, 116] or a change in the equilibrium structure of WDs with DM cores [117]. These are quite distinct from the observational signature considered in this work, which is the DM trigger of a type Ia SN (although see [118] for a related analysis).

In this paper, we examine DM candidates which have additional non-gravitational interactions and are thus capable of heating a WD and igniting a SN through the production of SM particles. An essential ingredient in this analysis is understanding the length scales over which SM particles deposit energy in a WD medium. We find that most high energy particles thermalize rapidly, over distances shorter than or of order the critical size for fusion. Particle production is thus an effective means of igniting WDs. Constraints on these DM candidates come from either observing specific, long-lived WDs or by comparing the measured rate of type Ia SN with that expected due to DM. It is important to note that these constraints are complementary to direct searches—it is more massive DM that is likely to trigger SN, but also more massive DM that has low terrestrial flux. The WD detector excels in this regime due to its large surface area  $\sim (10^4 \text{ km})^2$ , long lifetime  $\sim \text{Gyr}$ , and high density. We demonstrate these constraints for generic classes of DM models that produce SM particles via DM-SM scattering, DM-DM collisions, or DM decays, and consider the significantly enhanced constraints for DM that is captured in the star. For these cases, we are able to place new bounds on DM interactions for masses greater than  $m_\chi \gtrsim 10^{16} \text{ GeV}$ . As a concrete example we consider ultra-heavy Q ball DM as found in supersymmetric extensions of the SM.

The rest of the paper is organized as follows. We begin in Section 4.2 by reviewing the mechanism of runaway fusion in a WD. In Section 4.3 we study the heating of a WD due to the production of high-energy SM particles. Detailed calculations of the stopping of such particles are provided in Appendix D. In Section 4.4 we parameterize the explosiveness and event rate for generic classes of DM-WD encounters, and in Section 4.5 we derive schematic constraints on such models. The details of DM capture in a WD are reserved for Appendix E. Finally we specialize to the case of Q-balls in Section 4.6, and conclude in Section 4.7.

## 4.2 White Dwarf Runaway Fusion

We first review the conditions for which a local energy deposition in a WD results in runaway fusion. Any energy deposit will eventually heat ions within some localized region—parameterize this region by its linear size  $L_0$ , total kinetic energy  $\mathcal{E}_0$  and typical temperature  $T_0$ . These scales evolve in time, but it will be useful to describe a given heating event by their initial values.

The fate of a heated region is either a nonviolent diffusion of the excess energy across the star, or a runaway fusion chain-reaction that destroys the star. The precise outcome depends on  $L_0$ ,  $\mathcal{E}_0$  and  $T_0$ . There is a critical temperature  $T_f$ , set by the energy required for ions to overcome their mutual Coulomb barrier, above which fusion occurs. For carbon burning,  $T_f \sim \text{MeV}$  [119]. Any heated region  $T_0 > T_f$  will initially support fusion, although this is not sufficient for runaway as cooling processes may rapidly lower the temperature below  $T_f$ . This cooling will not occur if the corresponding timescale is larger than the timescale at which fusion releases energy. Cooling in a WD is dominated by thermal diffusion, and the diffusion time increases as the size of the heated region. However, the timescale for heating due to fusion is independent of region size. Thus, for a region at temperature  $\gtrsim T_f$ , there is a critical size above which the heated region does not cool but instead initiates runaway. For a region at the critical fusion temperature  $T_f$ , we call this critical size the *trigger size*  $\lambda_T$ . The value of  $\lambda_T$  is highly dependent on density, and in a WD is set by the thermal diffusivity of either photons or degenerate electrons. This critical length scale has been computed numerically in [114] for a narrow range of WD densities and analytically scaled for other WD masses in [103]. As in [103], we will restrict our attention to carbon-oxygen WDs in the upper mass range  $\sim 0.85 - 1.4 M_\odot$  (these will yield the most stringent constraints on DM). This corresponds to a central number density of ions  $n_{\text{ion}} \sim 10^{30} - 10^{32} \text{ cm}^{-3}$  and a trigger size of  $\lambda_T \sim 10^{-3} - 10^{-5} \text{ cm}$ .

If a heated region is smaller than the trigger size, its thermal evolution is initially dominated by diffusion. However, this will still result in runaway fusion if the temperature is of order  $T_f$  by the time the region diffuses out to the trigger size. For our purposes it is more natural to phrase this in terms of the total energy  $\mathcal{E}_0$  deposited during a heating event. Of course, the relation between energy  $\mathcal{E}_0$  and temperature  $T_0$  depends on the rate at which WD constituents—ions, electrons, and photons—thermalize with each other within the region size  $L_0$ . Given that the different species thermalize rapidly, the excess energy required to raise the temperature to  $T_f$  in a volume  $V$  is given by a sum of their heat capacities

$$\frac{\mathcal{E}_0}{V} \gtrsim \int_0^{T_f} dT (n_{\text{ion}} + n_e^{2/3} T + T^3), \quad (4.1)$$

where  $n_e$  is the number density of electrons. Note that we use the heat capacity of a degenerate gas of electrons, since the Fermi energy  $E_F \gtrsim \text{MeV}$  for the densities we consider. The minimum energy deposit necessary to trigger runaway fusion is simply

$$\mathcal{E}_{\text{boom}} \sim \lambda_T^3 (n_{\text{ion}} T_f + n_e^{2/3} T_f^2 + T_f^4) \approx 10^{16} - 10^{23} \text{ GeV}. \quad (4.2)$$

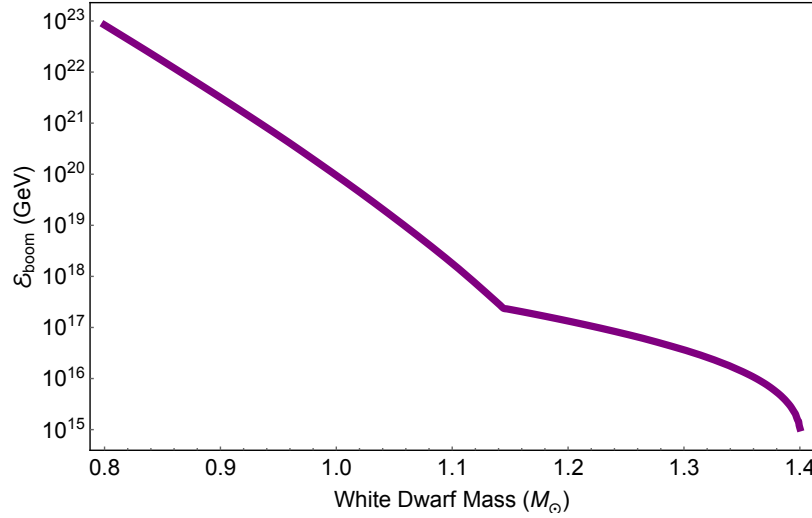


Figure 4.1: The minimum energy deposit (4.2) necessary to trigger runaway fusion, based on numerical results for  $\lambda_T$  [114] and the WD mass-density relation [120]

$\mathcal{E}_{\text{boom}}$  is shown over the range of WD masses in Figure 4.1, where we have employed a numerical formulation of the WD mass-density relation as given by [120]. Once again, for a given WD density the critical energy threshold is primarily set by  $\lambda_T$ —this length scale has been carefully computed and tabulated in [114], along with the attendant assumptions. In any case, we expect the simplified expression (4.2) to be accurate at the order of magnitude level, and we refrain from a more detailed analysis here. Thus for a heating event characterized by its  $L_0$ ,  $\mathcal{E}_0$ , and  $T_0 \gtrsim T_f$ , there is an *ignition condition*:

$$\mathcal{E}_0 \gtrsim \mathcal{E}_{\text{boom}} \cdot \max \left\{ 1, \frac{L_0}{\lambda_T} \right\}^3. \quad (4.3)$$

Any  $\mathcal{E}_0$  satisfying this condition is minimized for  $L_0$  less than the trigger size, where it is also independent of the precise value of  $L_0$ . For broader deposits, the necessary energy is parametrically larger than  $\mathcal{E}_{\text{boom}}$  by a volume ratio  $(L_0/\lambda_T)^3$ . As a result, understanding the  $L_0$  for different kinds of heating events in a WD is critical to determining whether or not they are capable of destroying the star.

### 4.3 Particle Heating of White Dwarfs

Production of high-energy SM particles in a WD will result in heating of the stellar medium. The critical quantity to understand is the length scale over which such heating occurs—this scale determines the efficiency of the heating event in triggering runaway fusion, as described

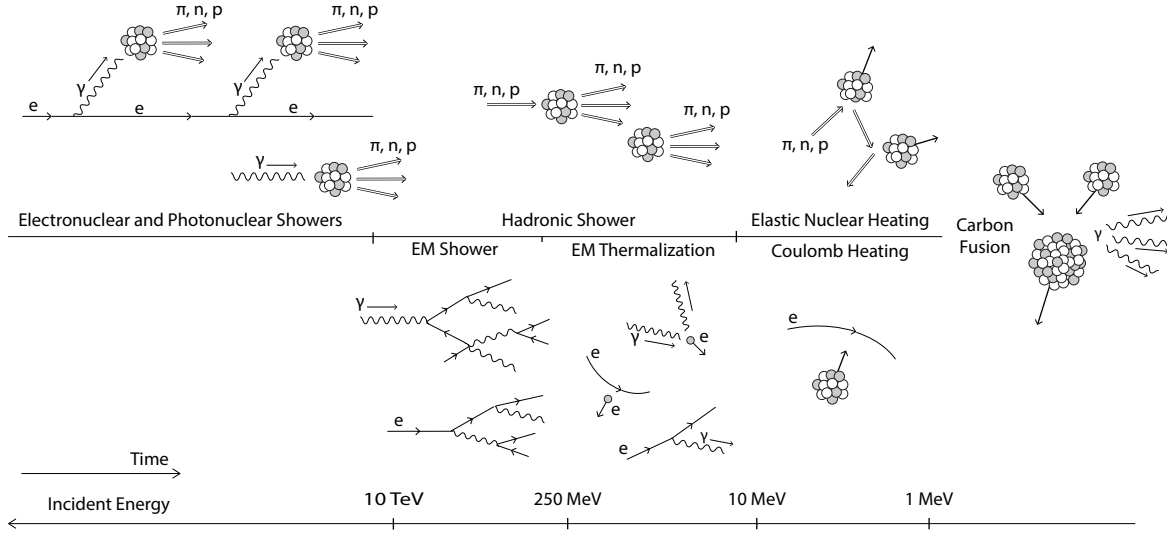


Figure 4.2: Dominant energy loss and thermalization processes in the WD as a function of energy, with energy decreasing towards the right. Hadronic processes are shown in the upper panel and EM processes in the lower panel. High energy particles will induce showers that terminate into elastic thermalization of the WD ions, moving from left to right in the diagram. The quoted energies are for a  $\sim 1.37 M_{\odot}$  WD, although the cartoon is qualitatively the same for all densities.

by condition (4.3). Note that this is a question of purely SM physics. The unknown physics of DM will serve only to set the initial properties of the SM particles.

We find that SM particles efficiently heat the WD regardless of species or energy (neutrinos are a slight exception)—the heating length is typically less than or of order the trigger size  $\lambda_T$ . This is accomplished primarily through hadronic showers initiated by collisions with carbon ions. In some cases electromagnetic showers are important, however at high energies these are suppressed by density effects and even photons and electrons are dominated by hadronic interactions. These showers rapidly stop high-energy particles due to their logarithmic nature, transferring the energy into a cloud of low-energy particles which heat the medium through elastic scatters. A schematic for the flow of energy during deposition is given in Figure 4.2. In this light, the WD operates analogously to a particle detector, including hadronic and electromagnetic “calorimeter” components. Runaway fusion provides the necessary amplification to convert a detected event into an observable signal.

The remainder of this section will discuss the above heating process in more detail. We summarize the dominant source of energy loss and the resulting stopping lengths  $\lambda$  for SM particles of incident kinetic energy  $\epsilon$ . The total path length traveled by a particle before



depositing  $\mathcal{O}(1)$  of its energy is approximately

$$R_{\text{SP}} \sim \frac{\epsilon}{dE/dx}, \quad (4.4)$$

where  $dE/dx$  is the stopping power in the WD medium. If the mean free path to hard scatter  $\lambda_{\text{hard}}$  is smaller than this path length  $R_{\text{SP}}$ , then the particle undergoes a random walk with  $N_{\text{hard}}$  scatters, and the net displacement is reduced by  $\sqrt{N_{\text{hard}}}$ . We therefore approximate the stopping length as

$$\lambda \sim \min \left\{ R_{\text{SP}}, \sqrt{R_{\text{SP}} \lambda_{\text{hard}}} \right\} \quad (4.5)$$

This random walk behavior is relevant for low-energy elastic scatters.

Stopping lengths are plotted in Figures 4.3 and 4.4, and a detailed treatment of the stopping powers is given in Appendix D. We will consider incident light hadrons, photons, electrons, and neutrinos—as we are concerned with triggering runaway fusion, we restrict our attention to energies  $\epsilon \gg T_f \sim \text{MeV}$ .

## High-Energy Showers

**Hadronic Showers.** Incident hadrons with kinetic energy larger than the nuclear binding scale  $\sim 10 \text{ MeV}$  will undergo violent inelastic collisions with carbon ions resulting in an  $\mathcal{O}(1)$  number of secondary hadrons. This results in a roughly collinear shower of hadrons of size

$$X_{\text{had}} \sim \frac{1}{n_{\text{ion}} \sigma_{\text{inel}}} \log \left( \frac{\epsilon}{10 \text{ MeV}} \right) \approx 10^{-6} \text{ cm} \left( \frac{10^{32} \text{ cm}^{-3}}{n_{\text{ion}}} \right).$$

where the inelastic nuclear cross section is  $\sigma_{\text{inel}} \approx 100 \text{ mb}$  and we have taken the logarithm to be  $\sim 10$ . The shower terminates into pions and nucleons of energy  $\sim 10 \text{ MeV}$ , whose cooling is discussed below. Note that neutral pions of energy  $10 - 100 \text{ MeV}$  have a decay length to photons of  $\delta_{\pi^0} \sim 10^{-6} \text{ cm}$ . Hadronic showers will therefore generate an electromagnetic component carrying an  $\mathcal{O}(1)$  fraction of the energy.

**Photonuclear and Electronuclear Showers.** A photon or electron can directly induce hadronic showers via production of a quark-antiquark pair, depicted in Figure 4.5. The LPM effect, discussed below, ensures that these process dominate the stopping of photons and electrons at high energies,  $\epsilon \gtrsim 10^4 - 10^6 \text{ GeV}$ .

The only substantial difference between photonuclear showers and purely hadronic ones is that they require a longer distance to initiate. Roughly, the photonuclear cross section is suppressed relative to the hadronic inelastic cross section  $\sigma_{\text{inel}}$  by a factor of  $\alpha$ , and so the photon range is

$$\lambda_{\gamma A} \approx 10^{-5} \text{ cm} \left( \frac{10^{32} \text{ cm}^{-3}}{n_{\text{ion}}} \right). \quad (4.6)$$



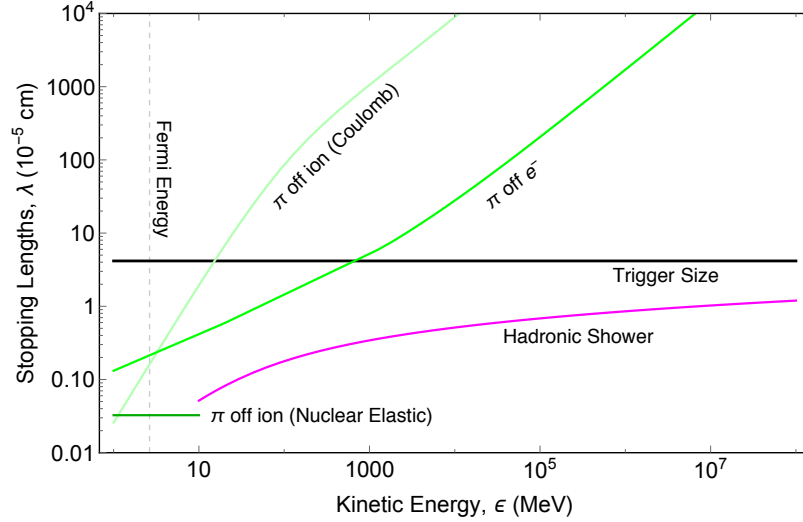


Figure 4.3: Stopping lengths for incident hadrons as a function of kinetic energy in a WD of density  $n_{\text{ion}} \sim 10^{31} \text{ cm}^{-3}$  ( $\approx 1.25 M_{\odot}$ ), including the hadronic shower length (magenta). Any discontinuities in the stopping lengths are due to approximate analytic results in the different energy regimes. See Appendix D for calculation details.

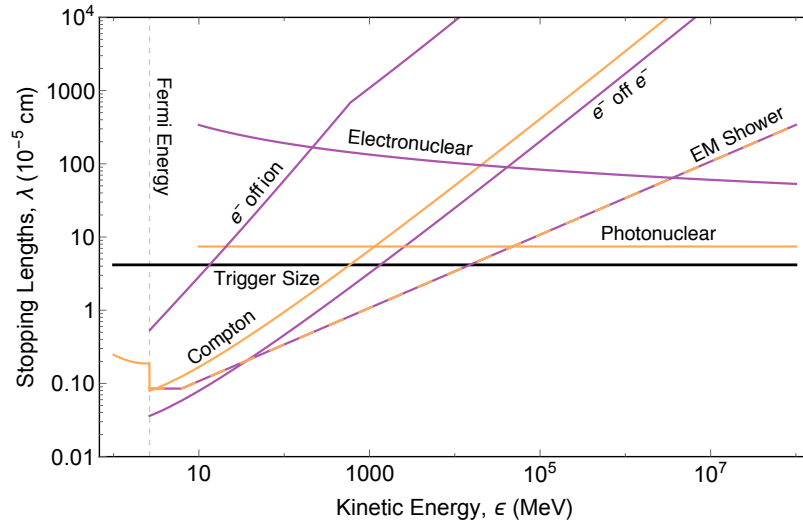


Figure 4.4: Stopping lengths of incident photons (orange) and electrons (purple) as a function of kinetic energy in a WD of density  $n_{\text{ion}} \sim 10^{31} \text{ cm}^{-3}$  ( $\approx 1.25 M_{\odot}$ ), including the EM shower length (dashed). Any discontinuities in the stopping lengths are due to approximate analytic results in the different energy regimes. See Appendix D for calculation details.

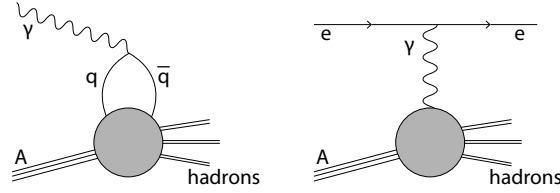


Figure 4.5: Photonuclear (left) and Electronuclear (right) interactions. The shaded region contains, at high energies, the familiar point-like processes of deep inelastic scattering and for energies below  $\Lambda_{\text{QCD}}$  is best described by exchange of virtual mesons.

Here  $\lambda_{\gamma A}$  is the distance to initiate a hadronic shower, whereas the shower itself extends a distance  $X_{\text{had}}$ . Note that  $\lambda_{\gamma A}$  is of order the trigger size.

The electronuclear showers are qualitatively different, as the electron survives the interaction. This process is best described as a continuous energy loss of the electron, due to radiation of virtual photons into hadronic showers. The stopping power is again radiative, which gives the constant stopping length

$$\lambda_{eA} \approx 10^{-4} \text{ cm} \left( \frac{10^{32} \text{ cm}^{-3}}{n_{\text{ion}}} \right). \quad (4.7)$$

This is suppressed by an additional factor of  $\alpha$  relative to the photonuclear interaction, although a full calculation also yields an  $\mathcal{O}(10)$  logarithmic enhancement. We see that the electronuclear length scale  $\lambda_{eA}$  is at most larger than the trigger size by an order of magnitude.

**Electromagnetic Showers.** Of course, electrons and photons can also shower through successive bremsstrahlung and pair-production. An electromagnetic shower proceeds until a critical energy  $\sim 100$  MeV, at which point these radiative processes become subdominant to elastic Coulomb and Compton scattering. Below this scale radiation can still be important, though electromagnetic showers do not occur. Note that bremsstrahlung and pair-production are strictly forbidden for incident energies below the Fermi energy  $E_F$ .

At sufficiently high electron/photon energies and nuclear target densities, electromagnetic showers are elongated due to the Landau-Pomeranchuk-Migdal (LPM) effect. High-energy radiative processes necessarily involve small momentum transfers to nuclei. These soft virtual photons cannot be exchanged with only a single ion, but rather interact simultaneously with multiple ions. This generates a decoherence, suppressing bremsstrahlung/pair-production above an energy  $E_{\text{LPM}}$  which scales inversely with density:

$$E_{\text{LPM}} \approx 1 \text{ MeV} \left( \frac{10^{32} \text{ cm}^{-3}}{n_{\text{ion}}} \right). \quad (4.8)$$

The corresponding shower lengths are

$$X_{\text{EM}} \approx X_0 \cdot \begin{cases} \left(\frac{\epsilon}{E_{\text{LPM}}}\right)^{1/2} & \epsilon > E_{\text{LPM}} \\ 1 & \epsilon < E_{\text{LPM}} \end{cases} \quad (4.9)$$

where

$$X_0 \approx 10^{-7} \text{ cm} \left( \frac{10^{32} \text{ cm}^{-3}}{n_{\text{ion}}} \right) \quad (4.10)$$

is the unsuppressed EM shower length. See Appendix D.3 for details. At the highest WD densities radiative processes are always LPM-suppressed, while at lower densities we observe both regimes. We emphasize that for all densities, throughout the energy range where it is relevant, the length of electromagnetic showers is never parametrically larger than the trigger size.

**Neutrinos.** Neutrinos scatter off nuclei with a cross section that increases with energy. In these interactions, an  $\mathcal{O}(1)$  fraction of the neutrino energy is transferred to the nucleus with the rest going to produced leptons—this is sufficient to start a hadronic shower [121, 122]. At an energy of  $\sim 10^{11}$  GeV, [121] calculates the neutrino-nuclear cross section to be  $\sim 10^{-32} \text{ cm}^2$ . Conservatively assuming this value for even higher energies, we find a neutrino mean free path in a WD of order  $\sim 10$  cm. Therefore, any high-energy neutrino released in the WD will (on average) only interact after traveling a distance  $\gg \lambda_T$ . As per the discussion above, this makes the heating of a WD via the release of multiple neutrinos highly inefficient due to the (enormous) volume dilution factor in (4.3). Interestingly, a *single* high-energy neutrino with energy greater than  $\mathcal{E}_{\text{boom}}$  will still be able to efficiently heat the star and trigger a runaway. This is because the neutrino mean free path is simply a displacement after which a compact shower of size  $X_{\text{had}}$  occurs. If the energy contained in a single shower is large enough, then the heating caused by this single neutrino can effectively be considered as a separate and efficient heating event.

## Low-Energy Elastic Heating

The showers of high-energy particles described above terminate in a cloud of low-energy  $\epsilon \sim 10$  MeV neutrons, protons, and charged pions, and  $\epsilon \sim 10 - 100$  MeV electrons and photons. Of course, particles at these energies may also be directly produced by the DM. At these energies, elastic nuclear, Coulomb, and Compton scatters dominate and eventually lead to the thermalization of ions. Once again, the physical expressions for all computed stopping powers and stopping lengths are given in Appendix D whereas we simply quote the relevant numerical values here.

**Hadrons.** Neutral hadrons are the simplest species we consider, interacting at low-energies only through elastic nuclear scatters with cross section  $\sigma_{\text{el}} \approx 1 \text{ b}$ , where  $1 \text{ b} = 10^{-24} \text{ cm}^2$ . Note that the large ion mass requires  $\sim 10 - 100$  hard scatters to transfer the hadron’s energy in the form of a random-walk. This elastic heating range is

$$\lambda_{\text{el}} \approx 10^{-7} \text{ cm} \left( \frac{10^{32} \text{ cm}^{-3}}{n_{\text{ion}}} \right), \quad (4.11)$$

and is always less than the trigger size.

Charged hadrons are also subject to Coulomb interactions, which would provide the dominant stopping in terrestrial detectors. In this case, however, Coulomb scatters off degenerate WD electrons are strongly suppressed and charged hadrons predominantly undergo elastic nuclear scatters like their neutral brethren. This suppression is due to (1) motion of the electrons, which fixes the relative velocity to be  $\mathcal{O}(1)$  and removes the enhancement of Coulomb stopping usually seen at low velocity, and (2) Pauli blocking, which forces the incident particle to scatter only electrons near the top of the Fermi sea. For an incident particle with velocity  $v_{\text{in}} \ll 1$ , the first effect suppresses the stopping power by a factor of  $v_{\text{in}}^2$  relative to that off stationary, non-degenerate electrons and the second by an additional factor of  $v_{\text{in}}$ . Note that there is a small range of energies in which Coulomb scatters off ions dominate the stopping of charged hadrons—either way, both length scales are well below the trigger size.

**Electrons and Photons.** For electrons and photons below  $\sim 100 \text{ MeV}$  the dominant interactions are Coulomb scatters off WD electrons and Compton scatters, respectively. The length scale of these processes is smaller than any interaction with ions, and so these electrons and photons will thermalize into a compact electromagnetic “gas” with a size set by the radiative length scale  $X_{\text{EM}}$ . The EM gas will cool and diffuse to larger length scales, eventually allowing thermalization with nuclei via the subdominant Coulomb scatters of electrons off ions. The photons of the EM gas will not undergo photonuclear showers here, as the gas will cool below  $\sim 10 \text{ MeV}$  by the time it diffuses out to a size  $\lambda_{\gamma A}$ . This gas temperature is initially at most  $\sim 100 \text{ MeV}$ . At these temperatures the heat capacity is dominated by photons, so as the gas diffuses to a size  $\lambda_{\gamma A}$  it cools by a factor  $(X_{\text{EM}}/\lambda_{\gamma A})^{3/4} \sim 10^{-2} - 10^{-1}$ . Note that for temperatures  $T$  less than  $E_F$ , the electrons are partially degenerate and heating proceeds via the thermal tail with kinetic energies  $\epsilon \sim E_F + T$ . Therefore, the relevant thermalization process is Coulomb scattering of electrons off ions.

Like the hadronic elastic scatters, an electron Coulomb scattering off ions will occasionally hard scatter, and thus deposit its energy along a random walk. This reduces the stopping length at low energies, yielding

$$\lambda_{\text{coul}} \approx 10^{-6} \text{ cm} \left( \frac{\epsilon}{10 \text{ MeV}} \right)^{3/2} \left( \frac{10^{32} \text{ cm}^{-3}}{n_{\text{ion}}} \right) \quad (4.12)$$

which is below the trigger size.

## 4.4 Dark Matter-Induced Ignition

Any DM interaction that produces SM particles in a WD has the potential to ignite the star, provided that sufficient SM energy is produced. The distribution in space, momentum, and species of these SM products is dependent on unknown DM physics and is needed to determine the rate of DM-induced ignition. This can be done precisely for a specific DM model, as we do for Q-balls in Section 4.6. In this Section, however, we study some general features of DM-WD encounters involving DM that possesses interactions with itself and the SM. We collect below the basic formulas relating DM model parameters to ignition criteria, SN rate, etc.

DM can generically heat a WD through three basic processes: DM-SM scattering, DM-DM collisions, and DM decays. For ultra-heavy DM, these processes can be complicated events involving many (possibly dark) final states, analogous to the interactions of heavy nuclei. In the case of DM-SM scattering, we consider both elastic and inelastic DM scatters off WD constituents, e.g. carbon ions. We classify DM candidates into three types according to the interaction that provides the dominant source of heating, and refer to these as scattering, collision, and decay candidates. We also make the simplifying assumption that the above events are “point-like”, producing SM products in a localized region (smaller than the heating length) near the interaction vertex. Where this is not the case (as in our elastic scattering and Q-ball constraints, see Sections 4.5 and 4.6), then the same formalism applies but with the event size added to the stopping length.

The SN rate may be greatly enhanced if DM is captured in the star, so we also consider separately “transiting DM” and “captured DM”. In general, there is some loss of DM kinetic energy in the WD. In the transit scenario, this energy loss is negligible and the DM simply passes through the star. In the capture scenario, the energy loss is not directly capable of ignition but is sufficient to stop the DM and cause it to accumulate in the star. Energy loss may be due to a variety of processes, but for simplicity we will focus on an DM-nuclei elastic scattering. Of course, due to the velocity spread of DM in the rest frame of a WD, there will necessarily be both transiting and captured DM populations in the star.

### DM Transit

**DM-SM Scattering.** Runaway fusion only occurs in the degenerate WD interior where thermal expansion is suppressed as a cooling mechanism. The outer layers of the WD, however, are composed of a non-degenerate gas and it is therefore essential that a DM candidate penetrate this layer in order to ignite a SN. We parameterize this by a DM stopping power  $(dE/dx)_{\text{SP}}$ , the kinetic energy lost by the DM per distance traveled in the non-degenerate layer, and demand that

$$\left(\frac{dE}{dx}\right)_{\text{SP}} \ll \frac{m_{\chi} v_{\text{esc}}^2}{R_{\text{env}}}, \quad (4.13)$$

where  $R_{\text{env}}$  is the nominal size of the non-degenerate WD envelope and  $v_{\text{esc}} \sim 10^{-2}$  is the escape velocity of the WD, at which the DM typically transits the star.

DM-SM scattering will result in a continuous energy deposit along the DM trajectory (if the interaction is rare enough for this not to be true, then the encounter is analogous to the case of DM decay). This is best described by a linear energy transfer  $(dE/dx)_{\text{LET}}$ , the kinetic energy of SM particles produced per distance traveled by the DM. If these products have a heating length  $L_0$  then the energy deposit must at minimum be taken as the energy transferred along a distance  $L_0$  of the DM trajectory. Importantly, as per the ignition condition (4.3), such a deposition is *less* explosive unless  $L_0$  is smaller than the trigger size  $\lambda_T$ . We thus consider the energy deposited over the larger of these two length scales. Assuming the energy of the DM is roughly constant during this heating event, the ignition condition is:

$$\left(\frac{dE}{dx}\right)_{\text{LET}} \gtrsim \frac{\mathcal{E}_{\text{boom}}}{\lambda_T} \cdot \max\left\{\frac{L_0}{\lambda_T}, 1\right\}^2. \quad (4.14)$$

Note that the DM stopping power  $(dE/dx)_{\text{SP}}$  and the linear energy transfer  $(dE/dx)_{\text{LET}}$  are related in the case of elastic scatters, but in general the two quantities may be controlled by different physics. In addition, a transit event satisfying condition (4.13) will have negligible energy loss over the parametrically smaller distances  $\lambda_T$  or  $L_0$ , validating (4.14).

The above condition sums the individual energy deposits along the DM trajectory as though they are all deposited simultaneously. This is valid if the DM moves sufficiently quickly so that this energy does not diffuse out of the region of interest before the DM has traversed the region. We therefore require that the diffusion time  $\tau_{\text{diff}}$  across a heated region of size  $L$  at temperature  $T_f$  be larger than the DM crossing-time:

$$\tau_{\text{diff}} \sim \frac{L^2}{\alpha(T_f)} \gg \frac{L}{v_{\text{esc}}}, \quad (4.15)$$

where  $\alpha(T)$  is the temperature-dependent diffusivity. This condition is more stringent for smaller regions, so we focus on the smallest region of interest,  $L = \lambda_T$ . Then (4.15) is equivalent to demanding that the escape speed is greater than the conductive speed of the fusion wave front,  $v_{\text{cond}} \sim \alpha(T_f)/\lambda_T$ . Numerical calculations of  $v_{\text{cond}}$  are tabulated in [114], and indeed condition (4.15) is satisfied for all WD densities.

The rate of transit events is directly given by the flux of DM through a WD

$$\Gamma_{\text{trans}} \sim \frac{\rho_\chi}{m_\chi} R_{\text{WD}}^2 \left(\frac{v_{\text{esc}}}{v_{\text{halo}}}\right)^2 v_{\text{halo}}, \quad (4.16)$$

where  $\rho_\chi$  is the DM density in the region of the WD, and  $R_{\text{WD}}$  is the WD radius. Here  $v_{\text{halo}} \sim 10^{-3}$  is the virial velocity of our galactic halo. Note the  $(v_{\text{esc}}/v_{\text{halo}})^2 \sim 100$  enhancement due to gravitational focusing.

We will not consider here captured DM that heats the star via scattering events, as such heating will typically cause ignition before capture occurs. However, it is possible to cause ignition after capture if the collection of DM leads to an enhanced scattering process.

**DM-DM Collisions and DM Decays.** For a point-like DM-DM collision or DM decay event releasing particles of heating length  $L_0$ , ignition will occur if the total energy in SM products satisfies condition (4.3). Such an event will likely result in both SM and dark sector products, so we parameterize the resulting energy in SM particles as a fraction  $f_{\text{SM}}$  of the DM mass. For non-relativistic DM, the DM mass is the dominant source of energy and therefore  $f_{\text{SM}} \lesssim 1$  regardless of the interaction details. A single DM-DM collision or DM decay has an ignition condition:

$$m_\chi f_{\text{SM}} \gtrsim \mathcal{E}_{\text{boom}} \cdot \max \left\{ \frac{L_0}{\lambda_T}, 1 \right\}^3. \quad (4.17)$$

Thus the WD is sensitive to annihilations/decays of DM masses  $m_\chi \gtrsim 10^{16}$  GeV.

DM that is not captured traverses the WD in a free-fall time  $t_{\text{ff}} \sim R_{\text{WD}}/v_{\text{esc}}$ , and the rate of DM-DM collisions within the WD parameterized by cross section  $\sigma_{\chi\chi}$  is:

$$\Gamma_{\text{SN}}^{\text{ann}} \sim \left( \frac{\rho_\chi}{m_\chi} \right)^2 \sigma_{\chi\chi} \left( \frac{v_{\text{esc}}}{v_{\text{halo}}} \right)^3 v_{\text{halo}} R_{\text{WD}}^3. \quad (4.18)$$

Similarly the net DM decay rate inside the WD parameterized by a lifetime  $\tau_\chi$  is:

$$\Gamma_{\text{SN}}^{\text{decay}} \sim \frac{1}{\tau_\chi} \frac{\rho_\chi}{m_\chi} \left( \frac{v_{\text{esc}}}{v_{\text{halo}}} \right) R_{\text{WD}}^3. \quad (4.19)$$

## DM Capture

**Review of DM Capture.** We first summarize the capture and subsequent evolution of DM in the WD, ignoring annihilations or decays—see Appendix E for details. Consider a spin-independent, elastic scattering off carbon ions with cross section  $\sigma_{\chi A}$ . The rate of DM capture in gravitating bodies is of course very well-studied [123, 124]. However, this rate must be modified when the DM requires multiple scatters to lose the necessary energy for capture. Ultimately, for ultra-heavy DM the capture rate is of the form

$$\Gamma_{\text{cap}} \sim \Gamma_{\text{trans}} \cdot \min \left\{ 1, \bar{N}_{\text{scat}} \frac{m_{\text{ion}} v_{\text{esc}}^2}{m_\chi v_{\text{halo}}^2} \right\}, \quad (4.20)$$

where  $\bar{N}_{\text{scat}} \sim n_{\text{ion}} \sigma_{\chi A} R_{\text{WD}}$  is the average number of DM-carbon scatters during one DM transit. For the remainder of this Section, all results are given numerically assuming a WD central density  $n_{\text{ion}} \sim 10^{31} \text{ cm}^{-3}$ . The relevant parametric expressions are presented in further detail in Appendix E.

Once DM is captured, it eventually thermalizes with the stellar medium at velocity  $v_{\text{th}} \sim (T_{\text{WD}}/m_\chi)^{1/2}$ , where  $T_{\text{WD}}$  is the WD temperature. The dynamics of this process depend on the strength of the DM-carbon interaction, namely on whether energy loss to carbon ions provides a small perturbation to the DM's gravitational orbit within the star

or whether DM primarily undergoes Brownian motion in the star due to collisions with carbon. For simplicity, we will focus here only on the former case, corresponding roughly to interactions

$$\sigma_{\chi A} \lesssim \frac{m_\chi}{\rho_{\text{WD}} R_{\text{WD}}} \sim 10^{-26} \text{ cm}^2 \left( \frac{m_\chi}{10^{16} \text{ GeV}} \right) \quad (4.21)$$

where the DM is able to make more than a single transit through the star before thermalizing. Note that the opposite regime indeed also provides constraints on captured DM and is unconstrained by other observations, see Figure 4.9, however the resulting limits are similar to those presented here.

In the limit (4.21), captured DM will thermalize by settling to a radius  $R_{\text{th}}$  given by the balance of gravity and the thermal energy  $T_{\text{WD}}$ ,

$$R_{\text{th}} \approx 0.1 \text{ cm} \left( \frac{m_\chi}{10^{16} \text{ GeV}} \right)^{-1/2}. \quad (4.22)$$

This settling proceeds in two stages. Captured DM will initially be found on a large, bound orbit that exceeds the size of the WD, decaying after many transits of the star until the orbital size is fully contained within the WD. This occurs after a time

$$t_1 \approx 7 \times 10^{16} \text{ s} \left( \frac{m_\chi}{10^{16} \text{ GeV}} \right)^{3/2} \left( \frac{\sigma_{\chi A}}{10^{-35} \text{ cm}^2} \right)^{-3/2}. \quad (4.23)$$

The DM then completes many orbits within the star until its orbital size decays to the thermal radius, occurring after a further time

$$t_2 \approx 10^{14} \text{ s} \left( \frac{m_\chi}{10^{16} \text{ GeV}} \right) \left( \frac{\sigma_{\chi A}}{10^{-35} \text{ cm}^2} \right)^{-1}. \quad (4.24)$$

Note that the difference in scalings between  $t_1$  and  $t_2$  is due to the fact that, while the two times are ultimately determined by scattering in the star, the dynamics of the settling DM are quite distinct in each case.  $t_1$  is dominated by the time spent on the largest orbit outside the WD (which additionally depends on  $\sigma_{\chi A}$ ) while  $t_2$  is dominated by the time spent near the thermal radius. Subsequently the DM will begin steadily accumulating at  $R_{\text{th}}$ , with the possibility of self-gravitational collapse if the collected mass of DM exceeds the WD mass within this volume. This occurs after a time

$$t_{\text{sg}} \approx 10^9 \text{ s} \left( \frac{m_\chi}{10^{16} \text{ GeV}} \right)^{-1/2} \left( \frac{\sigma_{\chi A}}{10^{-35} \text{ cm}^2} \right)^{-1}. \quad (4.25)$$

Of course, not all of these stages may be reached within the age of the WD  $\tau_{\text{WD}}$ . The full time to collect and begin self-gravitating is  $t_1 + t_2 + t_{\text{sg}}$ .

At any point during the above evolution, captured DM has the potential to trigger a SN. We will consider ignition via either the decay or annihilation of captured DM. Of particular interest are events occurring within a collapsing DM core, as such cores have the additional ability to ignite a WD for DM masses less than  $\mathcal{E}_{\text{boom}}$ , either via multiple DM annihilations or by the formation of a black hole. This is discussed in detail in [4]. In the following, we restrict attention to the limit (4.21) and require DM masses sufficiently large so that a single collision or decay will ignite the star, and give only a quick assessment of DM core collapse.



**Captured DM-DM Collisions.** We now turn to the rate of DM-DM collisions for captured DM. Of course, the thermalizing DM constitutes a number density of DM throughout the WD volume. Assuming that  $t_1 + t_2 < \tau_{\text{WD}}$ , the total rate of annihilations for this “in-falling” DM is peaked near the thermal radius and is of order:

$$\Gamma_{\text{infall}} \sim \frac{(\Gamma_{\text{cap}} t_2)^2}{R_{\text{th}}^3} \sigma_{\chi\chi} v_{\text{th}}. \quad (4.26)$$

If  $\Gamma_{\text{infall}} t_2 > 1$ , then a SN will be triggered by the in-falling DM population. Otherwise if  $\Gamma_{\text{infall}} t_2 < 1$ , the DM will start accumulating at the thermal radius. If  $t_{\text{sg}} \ll t_2$  (as expected for such heavy DM masses) there will be no collisions during this time and thus a collapse will proceed. For a DM sphere consisting of  $N$  particles at a radius  $r$ , the rate of annihilations is

$$\Gamma_{\text{collapse}} \sim \frac{N^2}{r^3} \sigma_{\chi\chi} v_{\chi}, \quad v_{\chi} \sim \sqrt{\frac{GNm_{\chi}}{r}}. \quad (4.27)$$

Of course, there may be some stabilizing physics which prevents the DM from collapsing and annihilating below a certain radius, such as formation of a black hole or bound states. To illustrate the stringent nature of the collapse constraint we will simply assume some benchmark stable radius, as in Figure 4.10. We assume that the timescale for collapse at this radius is set by DM cooling  $t_{\text{cool}}$ , which is related to  $t_2$ . Note that if a single collision has not occurred during collapse, one may additionally examine annihilations of the subsequent in-falling DM down to the stable radius—for simplicity, we do not consider this scenario.

**Captured DM Decays.** Lastly, we compute the rate of decays for captured DM, which is simply proportional to the number of DM particles in the WD available for decay at any given instance. In the transit scenario (4.19), this rate is  $\Gamma \sim \tau_{\chi}^{-1} \Gamma_{\text{trans}} t_{\text{ff}}$ . In the capture scenario, this number is instead determined by the thermalization time within the WD  $\Gamma \sim \tau_{\chi}^{-1} \Gamma_{\text{cap}} t_2$ , conservatively assuming that after a thermalization time, the DM quickly collapses and stabilizes to an “inert” core incapable of further decay. If this is not the case, then the captured DM decay rate is given by  $\Gamma \sim \tau_{\chi}^{-1} \Gamma_{\text{cap}} \tau_{\text{WD}}$ .

## 4.5 Dark Matter Constraints

We now constrain some generic DM candidates which will ignite a WD via one of the processes parameterized in Section 4.4. These release SM particles that deposit their energy and thermalize ions within a distance described in Section 4.3. First, however, we review how WD observables constrain DM candidates capable of triggering SN.

### Review of WD Observables

Following the discussion of [103], our constraints come from (1) the existence of heavy, long-lived white dwarfs, or (2) the measured type Ia SN rate. The ages of WD can be

estimated by measuring their temperature and modeling their cooling over time, and we take the typical age of an old WD to be of order  $\sim \text{Gyr}$  [125]. RX J0648.04418 is one such nearby star and one of the heavier known WDs, with a mass  $\sim 1.25 M_\odot$  [126] and local dark matter density which we take to be  $\rho_\chi \sim 0.4 \text{ GeV/cm}^3$ . Of course, this is not the only known heavy WD—the Sloan Digital Sky Survey [127] has found 20+ others. The NuStar collaboration has also recently uncovered evidence for the likely existence of heavy WDs near the galactic center [128], where the DM density is assumed to be much greater  $\rho_\chi \gtrsim 10^3 \text{ GeV/cm}^3$  [129]. Such heavy candidates are particularly suited for our constraints as the energy deposit necessary to trigger SN (4.3) is a decreasing function of WD mass. However, less dense white dwarfs are significantly more abundant in the galaxy. Thus, even if a sufficiently massive DM is unable to trigger a violent heating event within the lifetime of a WD, it could still ignite enough lighter WDs to affect the measured SN rate of  $\sim 0.3$  per century. The DM-induced SN rate is estimated using the expected number of white dwarfs per galaxy  $\sim 10^{10}$  and their mass distribution [127]. Simulations indicate that only WD masses heavier than  $\sim 0.85 M_\odot$  will result in optically visible SN [103]. Therefore, most of the stars exploded in this manner will be in the mass range  $\sim 0.85 - 1 M_\odot$ , resulting in weaker SN than expected of typical Chandrasekhar mass WDs.

To summarize, a bound on DM parameters can be placed if either a single explosive event occurs during the lifetime of an observed star such as RX J0648.04418, or the SN rate due to such DM events throughout the galaxy exceeds the measured value. Note that for low-mass WDs dominated by photon diffusion,  $\mathcal{E}_{\text{boom}}$  is a strong function of WD density. The average density for WDs is typically a factor  $\sim 10^{-2} - 10^{-1}$  less than the central density, although it is found that the WD density only changes by an  $\mathcal{O}(1)$  fraction from the central value up to a distance  $\sim R_{\text{WD}}/2$  [130]. Therefore the central density is a valid approximation as long as we consider heating events within this “modified” WD volume. For simplicity, we employ this approach.

## Scattering Constraints

In order to constrain a DM model with a scattering interaction, we require that it satisfy the ignition condition (4.14). This is given in terms of an LET, which parameterizes the ability for DM to release sufficient energy to the star in the form of SM particles. Here we consider a DM elastic scattering off carbon ions with cross section  $\sigma_{\chi A}$ , which has an LET:

$$\left( \frac{dE}{dx} \right)_{\text{LET}} \sim n_{\text{ion}} \sigma_{\chi A} m_{\text{ion}} v_{\text{esc}}^2. \quad (4.28)$$

This can be expressed in terms of the cross section per nucleon  $\sigma_{\chi n}$ —see Appendix E. Each elastic scatter transfers an energy of order  $m_{\text{ion}} v_{\text{esc}}^2 \approx 1 - 10 \text{ MeV}$  to the target nuclei, thus enabling fusion reactions. Note that the stopping power of the DM in the non-degenerate envelope is of the same form, but with the density replaced by its diminished value in this region. It is interesting that combining the ignition condition (4.14) with the requirement

that the DM adequately penetrates the non-degenerate layer (4.13) yields a lower bound on DM mass.

$$m_\chi > \mathcal{E}_{\text{boom}} \left( \frac{R_{\text{env}}}{\lambda_T} \right) \left( \frac{\rho_{\text{env}}}{\rho_{\text{WD}}} \right) \frac{1}{v_{\text{esc}}^2}, \quad (4.29)$$

where  $\rho_{\text{WD}}$  is the central density of the WD. Here  $R_{\text{env}} \approx 50$  km is the width of a non-degenerate WD envelope—the density in this region  $\rho_{\text{env}}$  is typically a small fraction  $\sim 10^{-3}$  of the central density [125]. We conservatively take the envelope to be composed of carbon ions; if it were primarily hydrogen or helium, then the condition for penetration is weakened by 4 orders of magnitude due to the reduced energy transfer and cross section for scattering. We find that the DM must be heavier than  $\sim 10^{28}$  GeV to ensure an explosive transit of a  $1.25 M_\odot$  WD *and* minimal loss of kinetic energy in the non-degenerate layer. For the sake of comparison this corresponds to a macroscopic DM mass of order  $\sim 20$  kg.

Of course, this bound is only applicable if the energy input to the WD is solely coming from DM kinetic energy. We may also consider DM inelastic scattering off carbon ions which transfer more than  $\sim$  MeV per collision. Examples of such a process include baryon-number violating interactions which can release the nucleon mass energy  $\sim$  GeV per collision. This is similar to Q-balls, which absorb the baryon number of nuclear targets and liberate binding energy rather than transferring kinetic energy—this interaction is examined in Section 4.6. Note that the assumption of a “point-like” interaction requires that the physical size of the DM is much smaller than  $\lambda_T$ —this is sensible up to masses of order  $\sim 10^{47}$  GeV, at which point the gravitational radius of the DM exceeds  $\lambda_T$ .

In Figure 4.6 we constrain the DM elastic scattering cross section per nucleon  $\sigma_{\chi n}$  as a function of DM mass  $m_\chi$  using the different classes of observables described above. Note that the scattering cross sections constrained here are incredibly large  $\gtrsim 10^{-10}$  cm<sup>2</sup>—however, the constraints from WDs reach to very large masses for which no other constraints exist. At these masses, the most stringent limits on DM elastic scattering are from CMB and Lyman- $\alpha$  spectrum analysis [131], which constrain  $\frac{\sigma_{\chi n}}{m_\chi} < \frac{10^{-3}\text{b}}{\text{GeV}}$ . These cross sections also require that the DM involved be macroscopically large, of order or larger than the trigger size, and so the interaction is decidedly not “point-like.” This fact does not weaken our constraints, however, since the energy transferred to each ion in the DM’s path is greater than  $\sim$  MeV.

## Collision and Decay Constraints

In order to constrain a DM model through its annihilations or decays within a WD, we require that it satisfy the ignition condition (4.17). Consider a single annihilation or decay with  $f_{\text{SM}} = 1$  that releases a spectrum of SM particles. As shown in Section 4.3, the constraint has minimal dependence on the released species if the typical energy  $\epsilon$  of secondary products is greater than an MeV. In the case of neutrinos, we may simply demand that  $\epsilon$  is sufficiently large that a single neutrino can ignite the star. With this schematic for the DM interaction, we can constrain the cross section for collision  $\sigma_{\chi\chi}$  and lifetime  $\tau_\chi$ . This is done in Figures 4.7

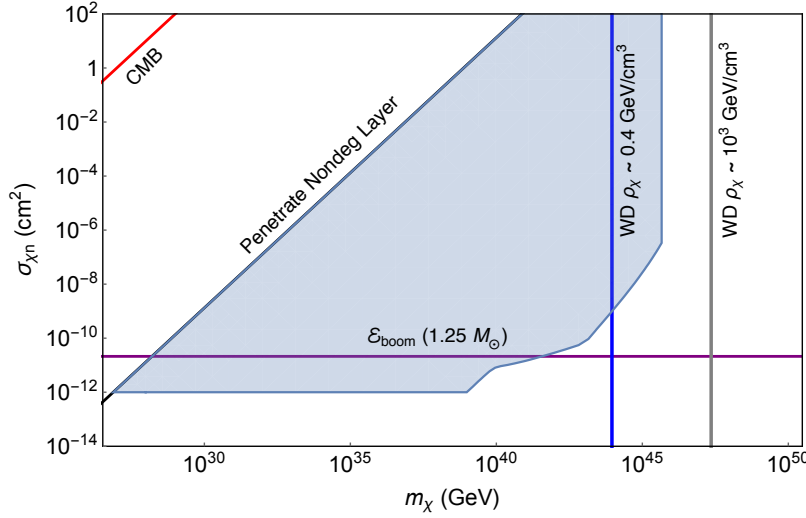


Figure 4.6: Constraints on DM-carbon elastic scattering cross section. Bounds come from demanding that the DM transit triggers runaway fusion (4.14) and occurs at a rate (4.16) large enough to either ignite a  $1.25 M_\odot$  WD in its lifetime or exceed the measured SN rate in our galaxy (blue shaded). We also demand that the DM penetrates the non-degenerate stellar envelope, taken at the highest densities, without losing appreciable kinetic energy. Constraints from the CMB/large-scale structure [131] are depicted as well.

and 4.8 in the case of transiting DM using the different classes of observables for DM-DM collisions and DM decays, respectively.

Of course there are existing limits on DM annihilations and decays, complementary to the ones placed from WDs. DM annihilations/decays inject energy and affect the ionization history of our universe, which can be probed by measurements of the CMB temperature and polarization angular spectrum [134, 132, 133]. These constraints are of order  $\sigma_{\chi\chi}v < 10^{-27} \frac{\text{cm}^3}{\text{s}} \left(\frac{m_\chi}{10 \text{ GeV}}\right)$  for annihilations, and  $\tau_\chi > 10^7$  Gyr for decay. There are also constraints on DM annihilation/decays in our halo from the cosmic ray (CR) flux seen in large terrestrial detectors. Here we provide a crude estimate of the expected constraints from CRs in the case of DM annihilation (decays are qualitatively similar). A more detailed analysis is beyond the scope of this work. The Pierre Auger Observatory [135] has detected the flux of  $E_{\text{th}} \sim 10^{11}$  GeV cosmic rays with an exposure of order  $A_{\text{PA}} \sim 40000 \text{ km}^2 \text{ sr yr}$ . Ultra-heavy DM annihilations  $m_\chi > 10^{16}$  GeV will generally produce secondary particles of energy  $\epsilon \gtrsim E_{\text{th}}$  via final-state radiation. For a simple 2-2 process (e.g.  $\chi\chi \rightarrow qq$ ), the expected number of final-state particles radiated at  $E_{\text{th}}$  due to QCD showers is approximated by the Sudakov double logarithm

$$N_{\text{rad}} \sim \frac{4\alpha_s}{\pi} \log\left(\frac{m_\chi}{\Lambda_{\text{QCD}}}\right) \log\left(\frac{m_\chi}{E_{\text{th}}}\right) \approx 100, \quad (4.30)$$

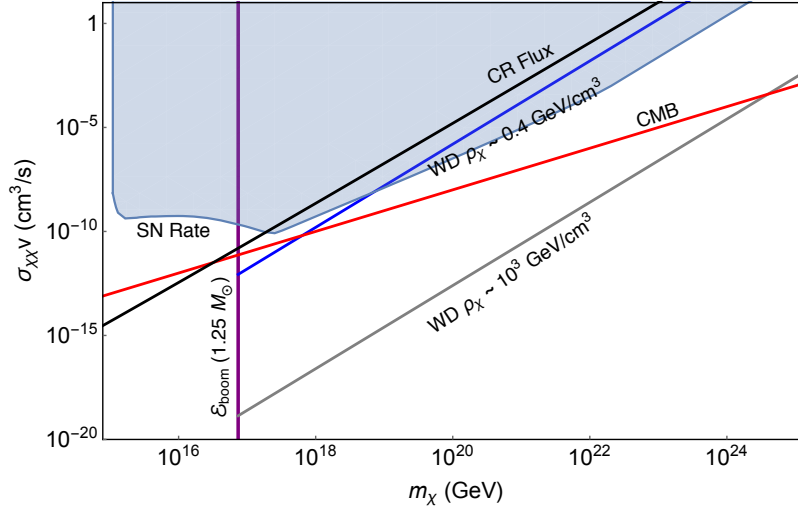


Figure 4.7: Constraints on DM-DM collision cross section to SM products of energy  $\epsilon \gg \text{MeV}$ . Bounds come from demanding that the DM transit interaction triggers runaway fusion (4.17) and occurs at a rate (4.18) large enough to either ignite an observed  $1.25 M_\odot$  WD in its lifetime or exceed the measured SN rate in our galaxy (blue shaded). Also shown are the CMB [132] (red) and CR flux (black) constraints on DM annihilations.

where  $\alpha_s$  is the QCD coupling constant. Similarly, the estimated number of final-state particles at  $E_{\text{th}}$  due to EW showers is  $\approx 50$ . We expect that CRs at this energy originating in our galaxy will be able to strike the earth unattenuated. Thus, such events would affect the measured CR flux of Pierre Auger unless

$$\left(\frac{\rho_\chi}{m_\chi}\right)^2 \sigma_{\chi\chi} v \frac{R_{\text{halo}}}{4\pi} N_{\text{rad}} \times A_{\text{PA}} \lesssim 1. \quad (4.31)$$

Here we assume an average value for DM density  $\rho_\chi \approx 0.4 \text{ GeV/cm}^3$  as a reasonable approximation to the integral over our galactic halo volume. Surprisingly, the above CR constraints are (within a few orders of magnitude) comparable to the constraints due to the observation of long-lived WDs. This is actually due to a coincidence in the effective “space-time volumes” of the two systems. A terrestrial CR detector such as Pierre Auger sees events within a space-time volume ( $R_{\text{det}}^2 R_{\text{halo}} \times t_{\text{det}}$ ), where  $R_{\text{det}} \sim 50 \text{ km}$ ,  $R_{\text{halo}} \sim 10 \text{ kpc}$ , and  $t_{\text{det}} \sim 10 \text{ yr}$ . This is similar in magnitude to the WD space-time volume ( $R_{\text{WD}}^3 \times \tau_{\text{WD}}$ ).

It is important to note that there is a large parameter space in  $\sigma_{\chi\chi}$  which will lead to DM capture, thermalization, and core collapse in a WD. This is depicted in Figure 4.9, along with the existing constraints on DM elastic scattering. As detailed in [136], direct detection experiments such as Xenon 1T [137] are only sensitive to DM masses  $m_\chi < 10^{17} \text{ GeV}$ . For even larger masses  $m_\chi < 10^{26} \text{ GeV}$  there are constraints from the MACRO experiment [138]

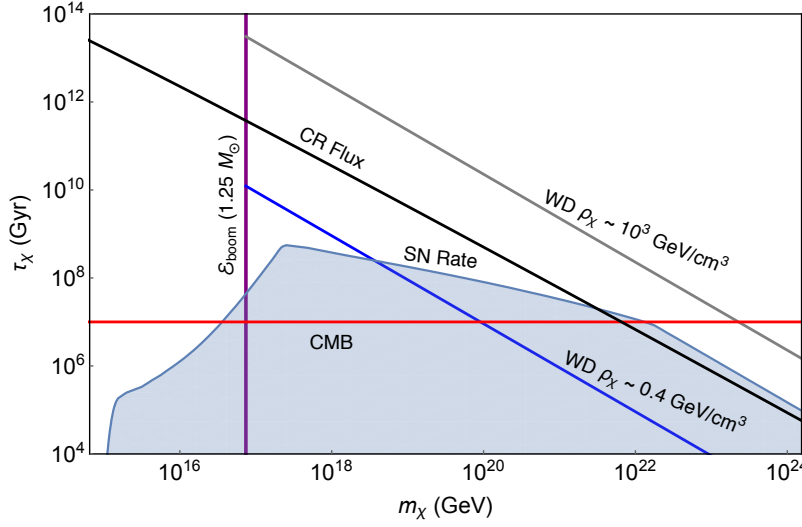


Figure 4.8: Constraints on DM decay to SM products of energy  $\epsilon \gg \text{MeV}$ . Bounds come from demanding that the DM transit interaction triggers runaway fusion (4.17) and occurs at a rate (4.19) large enough to either ignite an observed  $1.25 M_{\odot}$  WD in its lifetime or exceed the measured SN rate in our galaxy (blue shaded). Also shown are the CMB [133] (red) and CR flux (black) constraints on DM lifetime.

and from ancient excavated mica. The latter has been studied in [139]. We have similarly estimated the bounds from MACRO assuming a detectable threshold of  $\sim 5 \text{ MeV/cm}$  [138].

In the case of captured DM, we show the constraints on  $\sigma_{\chi\chi}$  and  $\tau_{\chi}$  assuming a benchmark value of the elastic scattering cross section  $\sigma_{\chi n} = 10^{-32} \text{ cm}^2$ . With regards to DM-DM collisions, we also assume a stabilizing radius for the collapsing DM sphere. This is done in Figures 4.10 and 4.11—for simplicity, here we only show the constraints from the existence of nearby, heavy WDs.

## 4.6 Q-balls

Having derived constraints on generic models of ultra-heavy DM, we turn towards a concrete example. In various supersymmetric extensions of the SM, non-topological solitons called Q-balls can be produced in the early universe [140, 141]. If these Q-balls were stable, they would comprise a component of the DM today. For gauge-mediated models with flat scalar potentials, the Q-ball mass and radius are given by

$$M_Q \sim m_S Q^{3/4}, \quad R_Q \sim m_S^{-1} Q^{1/4}, \quad (4.32)$$

where  $m_S$  is related to the scale of supersymmetry breaking, and  $Q$  is the global charge of the Q-ball—in our case, baryon number. The condition  $M_Q/Q < m_p$  ensures that the Q-ball is

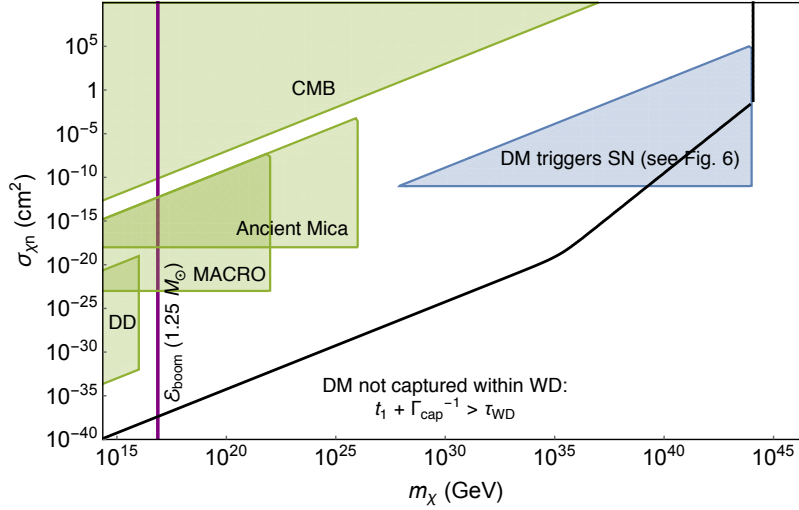


Figure 4.9: Viable parameter space (above the black line) in which DM-nucleon elastic scattering leads to DM capture in a  $1.25 M_{\odot}$  WD. All of this space is subject to constraints on DM decay and DM-DM annihilation analogous to those given in Figures 4.11 and 4.10. Note the blue region, reproducing Figure 4.6, indicates DM which causes SN via elastic heating. We also indicate here estimates of the scattering constraints from cosmology, direct detection, MACRO, and ancient mica [139].

stable against decay to nucleons. The interaction of relic Q-balls with matter depends on its ability to retain electric charge [142]. We restrict our attention to electrically neutral Q-balls, which induce the dissociation of incoming nucleons and in the process absorb their baryonic charge. During this proton decay-like process (see Figure 4.12), excess energy of order  $\Lambda_{\text{QCD}}$  is released via the emission of 2–3 pions. We assume that for each Q-ball inelastic collision, there is equal probability to produce  $\pi^0$  and  $\pi^{\pm}$  under the constraint of charge conservation. The cross section for this interaction is approximately geometric

$$\sigma_Q \sim \pi R_Q^2, \quad (4.33)$$

and thus grows with increasing  $Q$ . Note that a sufficiently massive Q-ball will become a black hole if  $R_Q \lesssim GM_Q$ . In the model described above, this translates into a condition  $(M_{\text{pl}}/m_S)^4 \lesssim Q$ .

We now determine the explosiveness of a Q-ball transit. This process is described by a linear energy transfer

$$\left( \frac{dE}{dx} \right)_{\text{LET}} \sim n_{\text{ion}} \sigma_Q N_{\pi} \epsilon, \quad (4.34)$$

where the nuclear interaction results in  $N_{\pi} \approx 30$  pions released, each with kinetic energy  $\epsilon \approx 500$  MeV. These pions induce hadronic showers which terminate in low-energy hadrons



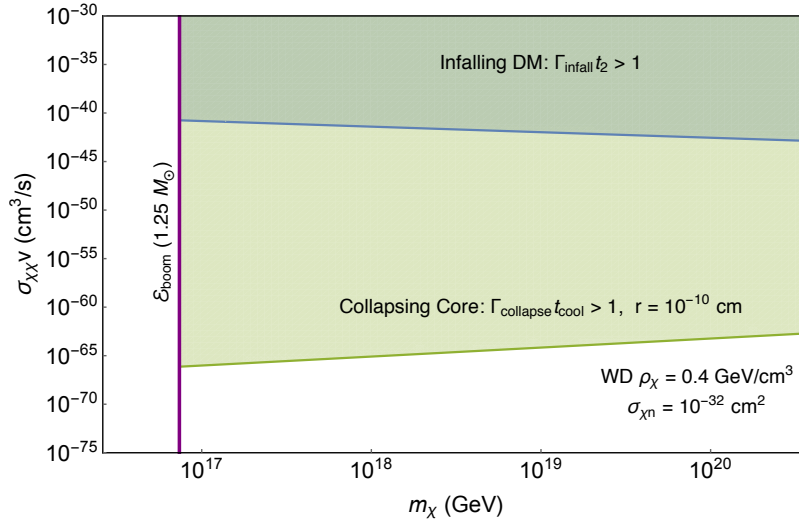


Figure 4.10: Constraints on DM-DM collision cross section to SM products of energy  $\epsilon \gg \text{MeV}$ , assuming DM is captured with an elastic scattering cross section  $\sigma_{\chi n} = 10^{-32} \text{ cm}^2$ . Bounds come from the observation of  $1.25 M_\odot$  WDs in local DM density. We consider the annihilation rate during the in-falling thermalization stage (4.26) (blue shaded) and during self-gravitational collapse (4.27) to a stable radius  $r = 10^{-10} \text{ cm}$  (green shaded). See text for details.

that rapidly transfer their energy to ions via elastic scatters, as discussed in Section 4.3. The pions have a heating length  $X_{\text{had}} \lesssim \lambda_T$ ; however, we will see the Q-ball has a finite size  $R_Q \gtrsim X_{\text{had}}$  in the region we are able to constrain. So, as mentioned in Section 4.4, we take the heating length to be  $L_0 \sim R_Q + X_{\text{had}} \sim R_Q$ . The ignition condition is then given by equations (4.14) and (4.34):

$$R_Q^2 \gtrsim \frac{1}{n_{\text{ion}}} \frac{\mathcal{E}_{\text{boom}}}{\lambda_T} \max \left\{ \frac{R_Q}{\lambda_T}, 1 \right\}^2 \left( \frac{1}{10 \text{ GeV}} \right). \quad (4.35)$$

This implies  $\sigma_Q \gtrsim 10^{-12} \text{ cm}^2$  is sufficient to ignite a  $1.25 M_\odot$  WD, which corresponds to a charge  $Q \gtrsim 10^{42} (m_S/\text{TeV})^4$ . Note that for sufficiently large  $Q$ , the radius will grow larger than  $\lambda_T$ . This situation still results in ignition, however, as the energy  $\sim 10 \text{ GeV}$  released per ion is much larger than the  $\sim \text{MeV}$  needed per ion for fusion. Note finally that the Q-ball interaction described above results in minimal slowing for Q-balls this massive, so transits will easily penetrate the non-degenerate WD envelope (4.13).

The existing limits on Q-balls primarily come from Super-Kamiokande and air fluorescence detectors of cosmic rays (OA, TA) [143]. However, the constraints that come from considering the ignition of WDs are in a fundamentally new and complementary region of parameter space. These are plotted in Figure 4.13. We have also included the constraints that result from gravitational heating of a WD during a Q-ball transit, as in [103].



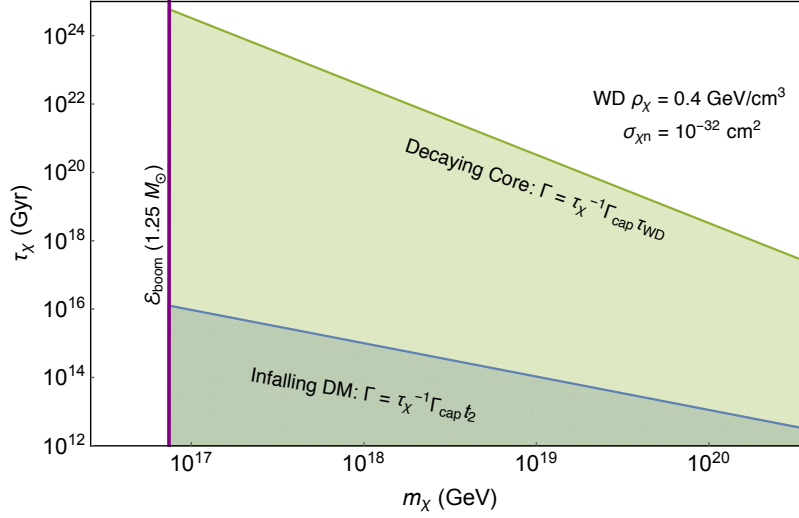


Figure 4.11: Constraints on DM decay to SM products of energy  $\epsilon \gg \text{MeV}$ , assuming DM is captured with an elastic scattering cross section  $\sigma_{\chi n} = 10^{-32} \text{ cm}^2$ . Bounds come from the observation of  $1.25 M_{\odot}$  WDs in local DM density. We consider the rate of decays during the in-falling thermalization stage (blue shaded) and for a decaying DM core (green shaded). See text for details.

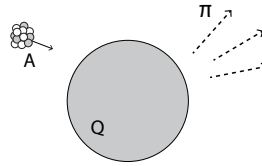


Figure 4.12: Interaction of a baryonic Q-ball with a nucleus  $A$ . The Q-ball destroys the nucleus and absorbs its baryonic charge, while the excess energy is radiated into roughly  $A$  outgoing pions of energy  $\Lambda_{\text{QCD}}$ .

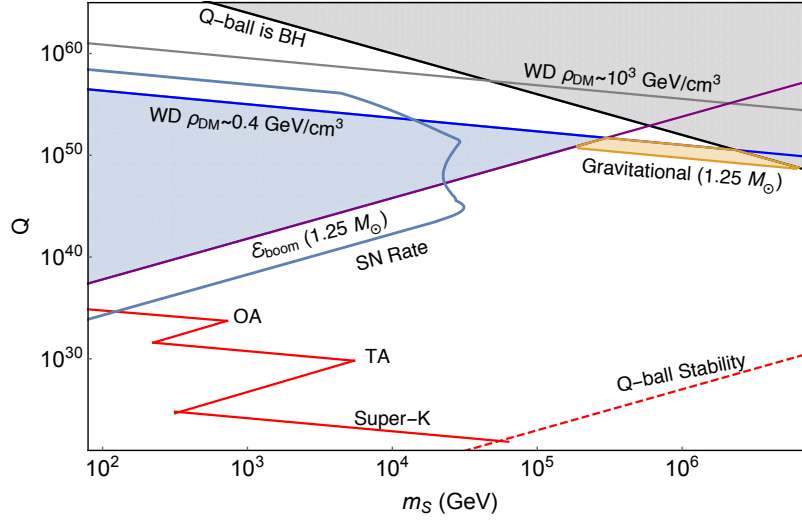


Figure 4.13: Constraints on Q-ball DM. Bounds come from demanding that the Q-ball interaction during a DM transit is capable of igniting WDs, occurring at a rate large enough to either ignite a single observed  $1.25 M_{\odot}$  WD in its lifetime (WD in local DM density is blue shaded) or exceed the measured SN rate in our galaxy. Also shown is the corresponding constraint from gravitational heating of WDs (orange shaded), and existing limits from terrestrial detectors (red) [143].

## 4.7 Discussion

The detection of ultra-heavy DM is an open problem which will likely require a confluence of astrophysical probes. Here we present a guide to constraining these candidates through DM-SM scatters, DM-DM annihilations, and DM decays inside a WD that release sufficient SM energy to trigger runaway fusion. In particular, we calculate the energy loss of high-energy particles due to SM interactions within the WD medium and determine the conditions for which a general energy deposition will heat a WD and ignite SN. Ultra-heavy DM that produces greater than  $10^{16}$  GeV of SM particles in a WD is highly constrained by the existence of heavy WDs and the measured SN rate. The formalism provided will enable WDs to be applied as detectors for any DM model capable of heating the star through such interactions. We have done so for baryonic Q-balls, significantly constraining the allowed parameter space in a complementary way to terrestrial searches.

We have explored briefly the application of this WD instability to self-gravitational collapse of DM cores, which has very interesting possibilities. The decay or annihilation of DM which is captured by a WD and forms a self-gravitating core is highly constrained for DM with mass greater than  $10^{16}$  GeV. In addition, such collapsing cores can provide enough heating via multiple annihilations to ignite the star for much smaller DM masses than those considered here, e.g.  $10^7$  GeV, and can induce SN through other means such as the formation

and evaporation of mini black holes. This is addressed in Chapter 5.

Finally, in addition to the constraints mentioned above, the general phenomenology of these DM-induced runaways will be the ignition of sub-Chandrasekhar mass WDs, possibly with no companion star present. Some of the mechanisms considered above are also likely to initiate fusion far from the center of the star. This is in contrast with conventional single-degenerate and double-degenerate mechanisms, which require a companion star and ignite fusion near the center of a super-Chandrasekhar mass WD [104]. This raises the tantalizing possibility that DM encounters with WDs provide an alternative explosion mechanism for type Ia SN or similar transient events, and that these events may be distinguishable from conventional explosions. Understanding and searching for possible distinguishing features of DM-induced events is an important follow-up work.

# Chapter 5

## Type Ia Supernovae from Dark Matter Core Collapse

### 5.1 Introduction

Dark matter (DM) accounts for over 80% of the matter density of the Universe, but its identity remains unknown. While direct detection [144] is a promising approach to identifying the nature of DM, searches for indirect signatures of DM interactions in astrophysical systems is also fruitful, particularly if the unknown DM mass happens to be large.

It was recently suggested [103] that white dwarfs (WD) act as astrophysical DM detectors: DM may heat a local region of a WD and trigger thermonuclear runaway fusion, resulting in a type Ia supernova (SN). DM ignition of sub-Chandrasekhar WDs was further studied in a companion paper [3], where we showed that generic classes of DM capable of producing high-energy standard model (SM) particles in the star can be constrained, e.g., by DM annihilations or decay to SM products. As an illustrative example, [3] placed new constraints on ultra-heavy DM with masses greater than  $10^{16}$  GeV for which a single annihilation or decay is sufficient to ignite a SN.

Here we examine the possibility of igniting SN by the formation and self-gravitational collapse of a DM core. We study two novel processes by which a collapsing DM core in a WD can ignite a SN—these were first pointed out in [3], and are studied here in more detail. If the DM has negligible annihilation cross section, collapse may result in a mini black hole (BH) that can ignite a SN via the emission of energetic Hawking radiation or possibly as it accretes. If the DM has a small but non-zero annihilation cross section, collapse can dramatically increase the number density of the DM core, resulting in SN ignition via a large number of rapid annihilations. Both of these processes extend the previously derived constraints on DM in [3], notably to masses as low as  $10^5$  GeV.

A number of potential observables of DM cores in compact objects have been considered in the literature. These include: (1) gravitational effects of DM cores on the structure of low-mass stars [145, 146, 147, 148, 149], WDs [117], and neutron stars (NS) [150, 151, 152, 153],

(2) BH formation and subsequent destruction of host NSs [154, 155, 156, 157, 158, 159, 160, 161, 162, 163, 164, 165, 166, 167, 168], and (3) anomalous heating from DM annihilations or scatters in WDs and NSs [169, 170, 171, 172, 173, 174, 175, 176]. See also [177, 178] for unique astroseismology signatures of possible low-mass bosonic DM cores. We emphasize that the signature of a DM core igniting a type Ia SN is distinct from these, and thus the constraints derived here are complementary. For instance, while it has been known that DM cores which form evaporating mini BHs are practically unobservable in a NS, this is decidedly not the case in a WD where (as we show) such BHs will typically ignite a SN. Note that [118] considers DM cores in WDs which inject heat and ignite SN through elastic DM-nuclear scatters—we discuss this process in more detail later as it pertains to our new constraints.

The paper is organized as follows. In Sec. 5.2, we review the triggering of runaway fusion by localized energy deposition in a WD. In Sec. 5.3, we summarize the necessary conditions for DM core collapse and discuss the generic end-states of such collapse. In Sec. 5.4 and Sec. 5.5, we derive constraints on DM cores which would ignite SN by the processes described above, namely black hole formation and DM-DM annihilations. We conclude in Sec. 5.6.

## 5.2 Triggering thermonuclear runaway

Thermonuclear runaway in a carbon WD generally occurs when the cooling timescale of a hot region exceeds the fusion timescale. Cooling is dominated by the thermal diffusion of either photons or degenerate electrons, while the highly exothermic fusion of carbon ions is unsuppressed at temperatures greater than their Coulomb threshold  $\approx$  MeV. Crucially, the diffusion time increases with the size  $L$  of the heated region while the fusion time is independent of  $L$ . This defines a critical trigger size and temperature for ignition:

$$L \gtrsim \lambda_T \text{ and } T \gtrsim \text{MeV} \Rightarrow \text{ignite supernova.} \quad (5.1)$$

$\lambda_T$  was numerically computed in [114] and is  $\lambda_T \approx 10^{-5}$  cm at a number density  $n_{\text{ion}} \approx 10^{32}$  cm $^{-3}$ .

One can also consider, as in [3], the critical energy  $\mathcal{E}_{\text{boom}}$  required to heat an entire trigger region  $\lambda_T^3$  to an MeV.  $\mathcal{E}_{\text{boom}} \approx 10^{16}$  GeV for  $n_{\text{ion}} \approx 10^{32}$  cm $^{-3}$  and sharply increases at lower WD densities—this agrees with the expectation that WDs grow closer to instability as they approach the Chandrasekhar mass. Of course to trigger runaway fusion, an energy in excess of  $\mathcal{E}_{\text{boom}}$  must also be deposited sufficiently rapidly. The relevant timescale is the characteristic diffusion time  $\tau_{\text{diff}}$  across a region of size  $\lambda_T$  at a temperature  $\approx$  MeV. This diffusion time is also computed in [114] to be  $\tau_{\text{diff}} \approx 10^{-12}$  s at densities  $n_{\text{ion}} \approx 10^{32}$  cm $^{-3}$ . Therefore a total energy  $\mathcal{E}$ , specifically deposited within a trigger region  $\lesssim \lambda_T^3$  and a diffusion time  $\lesssim \tau_{\text{diff}}$ , will ignite a SN if:

$$\mathcal{E} \gtrsim \mathcal{E}_{\text{boom}} \Rightarrow \text{ignite supernova.} \quad (5.2)$$

One possibility is that the necessary energy (5.2) is deposited directly to carbon ions, e.g., by a transiting primordial BH [103]. It is also possible to deposit this energy indirectly, e.g., by DM interactions releasing SM particles into the stellar medium [3]. To this end the stopping distances of high-energy ( $\gg$  MeV) particles in a WD was calculated in [3], where it was shown that hadrons, photons and electrons all transfer their energies to the stellar medium within a distance of order  $\lambda_T$  (the sole exception being neutrinos). We thus safely presume that any  $\mathcal{E} \gtrsim \mathcal{E}_{\text{boom}}$  released into these SM products inside  $\lambda_T^3$  will be efficiently deposited and thermalized within this region as well.

In summary, the rate of any process which deposits an energy  $\mathcal{E}$  (defined to be localized spatially within  $\lambda_T^3$  and temporally within  $\tau_{\text{diff}}$ ) that satisfies (5.2) can be constrained. This is done by either demanding that a single explosive event not occur during the lifetime of an observed heavy  $\gtrsim 1.2 M_\odot$  WD<sup>1</sup>, or that the occurrence of many such events throughout the galaxy in predominantly lower mass WDs not affect the observed SN rate. For simplicity we just utilize the former here and the existence of a WD with properties:

$$\begin{aligned} n_{\text{ion}} &\approx 10^{31} \text{ cm}^{-3}, & \rho_{\text{WD}} &\approx 3 \cdot 10^8 \frac{\text{g}}{\text{cm}^3}, \\ M_{\text{WD}} &\approx 1.25 M_\odot, & R_{\text{WD}} &\approx 3000 \text{ km}. \end{aligned} \quad (5.3)$$

Here  $n_{\text{ion}}$  and  $\rho_{\text{WD}}$  refer to the central density of the WD, and we relate this to its mass and radius using the equation of state formulated in [120]. While the average density is smaller by a factor  $\sim 10^{-1}$ ,  $n_{\text{ion}}$  only changes by  $\mathcal{O}(1)$  from the central value out to distances  $\sim R_{\text{WD}}/2$  [130]. For such a WD, the relevant trigger scales are of order:

$$\lambda_T \approx 4 \cdot 10^{-5} \text{ cm}, \quad \mathcal{E}_{\text{boom}} \approx 7 \cdot 10^{16} \text{ GeV}, \quad \tau_{\text{diff}} \approx 4 \cdot 10^{-11} \text{ s}. \quad (5.4)$$

These values are approximate, but we expect they are accurate at the order of magnitude level, as are the ensuing constraints. Finally, we assume the WD has a typical interior temperature  $T_{\text{WD}} \approx \text{keV}$  and lifetime  $\tau_{\text{WD}} \approx 5 \text{ Gyr}$  [125].<sup>2</sup>

### 5.3 Dark matter core collapse

Here we review the conditions for DM capture, collection, and self-gravitational collapse in a WD. As much of this discussion is already present in the literature, in what follows we simply quote the relevant results. We assume throughout that the DM loses energy primarily by short-range nuclear scatters. While other dissipation mechanisms are certainly possible (such as exciting dark states or emitting radiation) we will not treat these here.

Consider DM with mass  $m_\chi \gg 10 \text{ GeV}$  and scattering cross section off ions  $\sigma_{\chi A}$ . For spin-independent interactions,  $\sigma_{\chi A}$  is related to the DM-nucleon cross section  $\sigma_{\chi n}$  by

$$\sigma_{\chi A} = A^2 \left( \frac{\mu_{\chi A}}{\mu_{\chi n}} \right)^2 F^2(q) \sigma_{\chi n} \sim A^4 F^2(q) \sigma_{\chi n}, \quad (5.5)$$

<sup>1</sup>For instance, the Sloan Digital Sky survey has cataloged  $> 10$  such heavy WDs [127].

<sup>2</sup>The age of a WD is typically estimated by measuring its temperature and modeling the cooling over time.

where  $F^2(q)$  is the Helm form factor [179], and  $q \sim m_{\text{ion}} v_{\text{rel}} \sim m_{\text{ion}} \max[v, v_{\text{ion}}]$  is the momentum transfer between the DM at velocity  $v$  and a nuclear target. Currently the most stringent constraints on  $\sigma_{\chi n}$  come from Xenon 1T [144]:

$$\sigma_{\chi n} < 10^{-45} \text{ cm}^2 \left( \frac{m_\chi}{\text{TeV}} \right), \quad (5.6)$$

It is also possible for DM to have spin-dependent interactions (e.g., Majorana DM) which does not benefit from a  $A^2$  coherent enhancement and is less constrained by direct detection [180]. WDs predominantly consist of spin-zero nuclei ( $^{12}\text{C}$ ,  $^{16}\text{O}$ ), though as pointed out by [156] DM capture/thermalization can proceed by scattering off a lower density of non-zero spin nuclei (e.g., a small fraction of  $^{13}\text{C}$ ). For simplicity, we will restrict our attention here only to spin-independent interactions.

## Core formation

DM capture in compact objects has a long history [123, 124], though the usual formulae must be modified to account for heavy DM requiring multiple scatters to be captured (e.g., see [3]). DM transits the WD at a rate

$$\Gamma_{\text{trans}} \sim \frac{\rho_\chi}{m_\chi} R_{\text{WD}}^2 \left( \frac{v_{\text{esc}}}{v_{\text{halo}}} \right)^2 v_{\text{halo}}, \quad (5.7)$$

where  $v_{\text{esc}} \approx 2 \cdot 10^{-2}$  is the escape velocity and  $v_{\text{halo}} \approx 10^{-3}$  is the virial velocity of our galactic halo.  $\rho_\chi$  is the DM density in the region of the WD—we may consider either nearby WDs [127] with  $\rho_\chi \approx 0.4 \frac{\text{GeV}}{\text{cm}^3}$  or WDs close to the galactic center [128] where it is expected that  $\rho_\chi \gtrsim 10^3 \frac{\text{GeV}}{\text{cm}^3}$  [129]. Meanwhile, DM is captured by the WD at rate that is parametrically

$$\Gamma_{\text{cap}} \sim \Gamma_{\text{trans}} \cdot \min \left[ 1, \frac{N_{\text{scat}}}{N_{\text{cap}}(v_{\text{halo}})} \right]. \quad (5.8)$$

$N_{\text{scat}} \sim n_{\text{ion}} \sigma_{\chi A} R_{\text{WD}}$  is the average number of DM scatters during a single transit, and  $N_{\text{cap}}(v) \sim \frac{m_\chi v^2}{m_{\text{ion}} v_{\text{esc}}^2}$  is roughly the number of scatters needed for DM with velocity  $v$  asymptotically far away from star to become gravitationally bound, though with a necessary minimum of  $N_{\text{cap}} \geq 1$ . More properly,  $\Gamma_{\text{cap}}$  should be numerically calculated [181], though the expression in (5.8) is parametrically correct. Based on the assumed WD parameters (5.3), we find  $N_{\text{cap}}(v_{\text{halo}}) > 1$  for DM masses  $m_\chi > 10 \text{ TeV}$ ; in this regime, the capture rate scales as  $\Gamma_{\text{cap}} \propto \frac{\sigma_{\chi A}}{m_\chi^2}$  as opposed to the usual  $\Gamma_{\text{cap}} \propto \frac{\sigma_{\chi A}}{m_\chi}$  result that is often used.

We now turn to DM thermalization. This may proceed in either of two qualitatively different regimes, orbital decay or terminal drift, depending on the strength of dissipation. For simplicity we compute detailed constraints only for the case of orbital decay, which is applicable in the case of sufficiently small DM-nuclei cross section  $\sigma_{\chi A}$ , though we also briefly comment on the dynamics of DM terminal drift.

In the limit of orbital decay, DM within the WD follows gravitational orbits which gradually shrink as the DM dissipates energy. We require here that the timescale of energy loss is much slower than the DM orbital period, which is simply the gravitational free-fall time in the star

$$t_{\text{ff}} \sim \sqrt{\frac{1}{G\rho_{\text{WD}}}} \approx 0.1 \text{ s}. \quad (5.9)$$

The rate of energy loss due to nuclear scatters is given by

$$\frac{dE}{dt} \sim \rho_{\text{WD}} \sigma_{\chi A} v^2 \max[v, v_{\text{ion}}], \quad (5.10)$$

where  $v_{\text{ion}} \sim \sqrt{\frac{T_{\text{WD}}}{m_{\text{ion}}}} \approx 4 \cdot 10^{-4}$  is the thermal ion velocity and  $v$  is the velocity of the “in-falling” DM. The  $\max$  function distinguishes between the regimes of “inertial” and “viscous” drag, with the latter being relevant once  $v$  drops below  $v_{\text{ion}}$ . This dissipation is always small on orbital timescales provided  $\sigma_{\chi A}$  is below a critical cross section

$$\sigma_{\text{ff}} \sim \frac{m_{\chi}}{\rho_{\text{WD}} v_{\text{esc}} t_{\text{ff}}} \approx 3 \cdot 10^{-38} \text{ cm}^2 \left( \frac{m_{\chi}}{\text{TeV}} \right). \quad (5.11)$$

In addition to the drag force of (5.10), nuclear scatters will inflict a slight Brownian motion on the DM trajectory, though this only becomes important at cross sections well above  $\sigma_{\text{ff}}$ . An individual nuclear scatter will transfer a small amount of momentum  $\delta p \ll m_{\chi} v$  to the DM,

$$\delta p \sim m_{\text{ion}} \max[v, v_{\text{ion}}], \quad (5.12)$$

which is set by the ion momentum in the rest frame of the DM and is roughly constant for hard scatters. Over the course of one orbit, an accumulation of momentum transfers will yield a net change  $\Delta p$ . This accumulation is a Brownian process as each scatter transfers momentum of roughly the same magnitude  $\delta p$  (5.12) but with a random direction, giving  $\Delta p \sim \delta p \cdot N^{1/2}$  where  $N \sim n_{\text{ion}} \sigma_{\chi A} \max[v, v_{\text{ion}}] t_{\text{ff}}$  is the number of scatters occurring during an orbit. We find that  $\Delta p$  is small compared to the DM momentum  $m_{\chi} v$  provided that  $\sigma_{\chi A} < \sigma_{\text{ff}}$ . Thus the DM undergoes negligible deflection during an orbit, and Brownian motion may indeed be ignored for the case of orbital decay.

Thermalization in the orbital decay limit proceeds in three stages (e.g., see [156] for a detailed derivation). First, the DM will pass through the star many times on a wide elliptic orbit of initial size  $R_i \gg R_{\text{WD}}$  set by the number of scatters during the first stellar transit:

$$R_i \sim R_{\text{WD}} \left( \frac{m_{\chi}}{m_{\text{ion}}} \right) \frac{1}{\max[N_{\text{scat}}, 1]}. \quad (5.13)$$

The time for the DM orbital size to become contained within the WD is then:

$$t_1 \sim \frac{m_{\chi}}{\rho_{\text{WD}} \sigma_{\chi A} v_{\text{esc}}} \left( \frac{R_i}{R_{\text{WD}}} \right)^{1/2}, \quad (R_i \rightarrow R_{\text{WD}}). \quad (5.14)$$



Note that  $t_1$  is parametrically shorter if the DM scatters multiple times in a single transit  $N_{\text{scat}} > 1$  (see (5.13)), corresponding to cross sections  $\sigma_{\chi n} > 10^{-41} \text{ cm}^2$ . This results in a change of slope at  $10^{-41} \text{ cm}^2$  in the constraints shown in Fig. 5.1, 5.4, and 5.5. Subsequently the DM completes many orbits within the star, losing energy according to (5.10). Eventually the DM reaches velocities  $v_{\text{th}}$  and settles at a radius  $R_{\text{th}}$  where its kinetic energy is of order  $T_{\text{WD}}$  and balances the gravitational potential of the enclosed WD mass:

$$v_{\text{th}} \sim \sqrt{\frac{T_{\text{WD}}}{m_{\chi}}} \approx 10^{-7} \left( \frac{m_{\chi}}{10^8 \text{ GeV}} \right)^{-1/2}, \quad (5.15)$$

$$R_{\text{th}} \sim \left( \frac{T_{\text{WD}}}{G m_{\chi} \rho_{\text{WD}}} \right)^{1/2} \approx 500 \text{ cm} \left( \frac{m_{\chi}}{10^8 \text{ GeV}} \right)^{-1/2}. \quad (5.16)$$

The DM first slows to  $v_{\text{ion}}$  in a time

$$t_2 \sim \frac{m_{\chi}}{\rho_{\text{WD}} \sigma_{\chi A} v_{\text{ion}}}, \quad (v_{\text{esc}} \rightarrow v_{\text{ion}}). \quad (5.17)$$

and then to  $v_{\text{th}}$  in a time that is logarithmically greater:

$$t_3 \sim t_2 \log \left( \frac{m_{\chi}}{m_{\text{ion}}} \right), \quad (v_{\text{ion}} \rightarrow v_{\text{th}}). \quad (5.18)$$

A DM core will thus form within the age of the WD for  $\sigma_{\chi A} < \sigma_{\text{ff}}$  if

$$t_1 + t_2 + t_3 < \tau_{\text{WD}} \quad (\text{form DM core}). \quad (5.19)$$

We now consider  $\sigma_{\chi A} > \sigma_{\text{ff}}$ , the regime of terminal drift, in which case the condition for core formation is parametrically different than (5.19). In particular, the time required for DM to settle to  $R_{\text{th}}$  increases with increasing  $\sigma_{\chi A}$ , which sets an upper bound  $\sigma_{\text{max}}$  on the cross sections for which a DM core can form within the age of a WD. In this scenario,  $\mathcal{O}(1)$  of the DM kinetic energy is rapidly lost in the first pass through the star. The dynamics are then dominated by the drag force corresponding to (5.10)

$$F_A \sim \rho_{\text{WD}} \sigma_{\chi A} v \max[v, v_{\text{ion}}], \quad (5.20)$$

and the DM will fall towards  $R_{\text{th}}$  on a predominantly radial trajectory with the infall velocity given by the terminal speed at which  $F_A$  balances gravity. To estimate  $\sigma_{\text{max}}$ , we consider the extreme case of large  $\sigma_{\chi A}$  and a radial infall. Here  $F_A$  takes the linear form as  $v$  is small, and the DM drifts always with the local terminal speed, yielding a drift time

$$t_{\text{drift}} \sim \frac{t_{\text{ff}}^2}{t_2} \log \left( \frac{R_{\text{WD}}}{R_{\text{th}}} \right). \quad (5.21)$$

Core formation occurs if  $t_{\text{drift}} < \tau_{\text{WD}}$ , which sets an upper bound  $\sigma_{\text{max}} \sim 10^{16} \sigma_{\text{ff}}$ . Finally, with  $\sigma_{\chi A} > \sigma_{\text{ff}}$ , the Brownian nature of nuclear scatters may become important before a DM

particle reaches  $R_{\text{th}}$ , and its motion will then be a random walk with an inward gravitational drift. Indeed, the terminal velocity may fall below  $v_{\text{th}}$  as the DM approaches the center of the star, at which point the DM becomes thermal even outside of  $R_{\text{th}}$  and equilibrates with the stellar medium. The DM then settles into a Boltzmann distribution of temperature  $T_{\text{WD}}$ , in this case a Gaussian density profile with size  $R_{\text{th}}$  in the center of the star. The relevant core formation timescale is now the time required for thermal DM particles located at some  $r > R_{\text{th}}$  to settle into this distribution. But, such a biased random walk proceeds precisely as Brownian motion about a center which drifts inward at the terminal speed—thus the timescale for infall is just (5.21) and the bound  $\sigma_{\text{max}}$  is valid regardless of the onset of Brownian motion.

## Asymmetric DM Collapse

First consider the evolution of a core of non-annihilating DM, herein referred to as asymmetric DM [182, 183]. Upon formation, the DM core will steadily collect at  $R_{\text{th}}$  at a rate  $\Gamma_{\text{cap}}$ . If its density ever exceeds the WD density  $\rho_{\text{WD}}$ , then the core will become self-gravitating. The critical number of DM particles needed for the onset of self-gravitation is

$$N_{\text{sg}} \sim \frac{\rho_{\text{WD}} R_{\text{th}}^3}{m_\chi} \approx 5 \cdot 10^{32} \left( \frac{m_\chi}{10^8 \text{ GeV}} \right)^{-5/2}, \quad (5.22)$$

while the total number of DM particles that can possibly be collected within  $\tau_{\text{WD}}$  is simply:

$$N_{\text{life}} \sim \Gamma_{\text{cap}} \tau_{\text{WD}}. \quad (5.23)$$

Thus self-gravitational collapse requires

$$N_{\text{sg}} < N_{\text{life}}, \quad (\text{core self-gravitates}). \quad (5.24)$$

This sets an upper limit on the DM mass that can form a self-gravitating core  $m_\chi \gtrsim 100 \text{ TeV}$  (or  $R_{\text{th}} \lesssim 0.1 \text{ km}$ ), taking the maximum possible capture rate  $\Gamma_{\text{cap}} = \Gamma_{\text{trans}}$  and  $\rho_\chi = 0.4 \frac{\text{GeV}}{\text{cm}^3}$ .

Of course, this assumes that the DM core obeys Maxwell-Boltzmann statistics throughout the collection phase. In general, the quantum statistics of DM with velocity  $v$  in a core of size  $N$  becomes important once the de Broglie wavelength of individual DM particles exceeds their physical separation in the core. For the thermal DM population at  $R_{\text{th}}$ , this occurs after it has collected a number:

$$N_{\text{QM, th}} \sim (m_\chi T_{\text{WD}})^{3/2} R_{\text{th}}^3 \sim \frac{T_{\text{WD}}^3}{(G\rho_{\text{WD}})^{3/2}} \approx 10^{52}, \quad (5.25)$$

which is greater than  $N_{\text{sg}}$  for all DM masses  $m_\chi \gtrsim \text{GeV}$ . In the case of bosonic DM, if the core reaches  $N_{\text{QM, th}}$  before the onset of self-gravitation it will begin populating a Bose-Einstein condensate (BEC). A more compact BEC could then self-gravitate earlier, as considered by [154, 158, 157] in a NS. We find this is not possible in a WD, namely  $N_{\text{QM, th}} \gg N_{\text{life}}$  even for light bosonic DM  $m_\chi \lesssim \text{GeV}$ . Thus the condition for core collapse is indeed (5.24).

For simplicity, we focus on DM which scatters infrequently with the medium,  $\sigma_{\chi A} < \sigma_{\text{ff}}$ , see (5.11). The orbital timescale of the constituents of a collapsing core decreases faster than the timescale of energy loss due to nuclear scatters, so in this regime the DM trajectories will continue to have the form of slowly decaying orbits during the entire collapse.

In summary, the conditions (5.19) and (5.24) on  $\{m_\chi, \sigma_{\chi n}\}$  parameter space for which a DM core forms and collapses in a WD are depicted in Fig. 5.1. One can check that for DM masses and scattering cross sections satisfying (5.24), the left-hand side of the core formation condition (5.19) is ultimately dominated by  $t_1$ . We also show a rough amalgamation (e.g., see [136]), extending to large DM masses and cross sections, of the constraints from underground direct detection experiments including Xenon 1T [144].

We now turn to the dynamics of collapse. In order for a self-gravitating DM core to shrink, it must lose the excess gravitational potential energy. The “cooling” timescale  $t_{\text{col}}$  (leading to gravitational heating of the DM) is initially independent of DM velocity but hastens once the DM velocity exceeds  $v_{\text{ion}}$ . For a collapsing DM core with a number of particles  $N_{\text{col}}$ , the velocity and characteristic collapse time at size  $r$  is:

$$\begin{aligned} v_{\text{col}}(r) &\sim \sqrt{\frac{GN_{\text{col}}m_\chi}{r}}, \\ t_{\text{col}}(r) &\sim \frac{m_\chi v_{\text{col}}^2}{dE/dt(v_{\text{col}})} \sim t_2 \min \left[ 1, \frac{v_{\text{ion}}}{v_{\text{col}}} \right], \end{aligned} \quad (5.26)$$

where we have used elastic scatters (5.10) as the dominant dissipation mechanism. This should be modified once  $v_{\text{col}} \gtrsim 2 \cdot 10^{-2}$  and the momentum transfer becomes  $\sim \Lambda_{\text{QCD}}$ . At this point the interaction is not described by elastic scattering off nuclei, but an inelastic scattering off constituent quarks. This is a non-perturbative QCD process that will result in the release of pions. Since the typical momentum transfer here saturates at  $\sim \Lambda_{\text{QCD}}$ , the energy transfer per scatter scales linearly with velocity and is roughly of order  $\sim \Lambda_{\text{QCD}} v_{\text{col}}$ . For simplicity, we assume that the cross section for this inelastic interaction is also of order  $\sigma_{\chi A}$  (with the form factor (5.5) set to  $A^{-2}$ ). The rate of energy loss in this regime is parametrically

$$\frac{dE}{dt} \sim \Lambda_{\text{QCD}} n_{\text{ion}} \sigma_{\chi A} v_{\text{col}}^2. \quad (5.27)$$

Thus at velocities  $v_{\text{col}} \gtrsim 2 \cdot 10^{-2}$ , the characteristic core collapse time saturates to  $t_{\text{col}} \sim \frac{m_\chi}{n_{\text{ion}} \sigma_{\chi A} \Lambda_{\text{QCD}}}$ . One can also check that  $t_{\text{col}}$  is always greater than the (decreasing) dynamical time  $\sim r/v_{\text{col}}$ .

We emphasize that while cooling by nuclear scatters during core collapse is the minimal assumption, other dissipation mechanisms (e.g., radiating as a blackbody) could become efficient due to the increasing DM density, as considered by [154]. However since this is more model-dependent, we do not consider any such additional cooling mechanisms here.

Actually, the initial number of collapsing particles can be parametrically greater than the critical self-gravitation number  $N_{\text{col}} \gg N_{\text{sg}}$ . As discussed in [3], this occurs when the

time to capture a self-gravitating number is much less than the time for the DM core to collapse, i.e., when  $N_{\text{sg}} < \Gamma_{\text{cap}} t_{\text{col}}$ . We find this is relevant for DM masses  $m_\chi \gtrsim 10^{14}$  GeV. Here the collapsing core will inevitably “over-collect” to a much larger number until these two timescales become comparable  $N_{\text{col}} \sim \Gamma_{\text{cap}} t_{\text{col}}$ , although the density profile of the core at this point is highly non-trivial. It is worth noting that the collapsing core would likely be non-uniform even in the absence of over-collection, as emphasized in [160]—realistically, the core might develop a “cuspy” profile similar to the formation of galactic DM halos. In either case, a precise understanding of the DM core density profile is beyond the scope of this work. For simplicity we will assume a core of *uniform* density with a number of collapsing particles

$$N_{\text{col}} = \max[N_{\text{sg}}, \Gamma_{\text{cap}} t_{\text{col}}]. \quad (5.28)$$

However, this assumption of a uniform density core is likely a conservative one with regards to our constraints. For asymmetric DM, a density peak within the collapsing core (e.g. due to over-collection) would collapse to BHs of smaller mass than otherwise assumed and (as we show) would still ignite a SN. For annihilating DM, a density peak may have a greater rate of annihilations depending on the density profile which would ignite a SN sooner than otherwise assumed.

Though irrelevant prior to self-gravitation, QM effects may become important during the collapse itself. For a number of collapsing particles  $N_{\text{col}} = N_{\text{sg}}$ , this occurs once the de Broglie wavelengths of DM particles in the core begin overlapping:  $\frac{1}{m_\chi v_{\text{col}}(r)} \sim \frac{r}{N_{\text{sg}}^{1/3}}$ . That is, once the core has shrunk to a size

$$R_{\text{QM}} \sim \frac{1}{G m_\chi^3 N_{\text{sg}}^{1/3}} \approx 3 \cdot 10^{-11} \text{ cm} \left( \frac{m_\chi}{10^8 \text{ GeV}} \right)^{-13/6}, \quad (5.29)$$

and has a density

$$\rho_{\text{QM}} \sim \frac{N_{\text{sg}} m_\chi}{R_{\text{QM}}^3} \sim \frac{m_\chi^5 T_{\text{WD}}^3}{\rho_{\text{WD}}} \approx 10^{72} \frac{\text{GeV}}{\text{cm}^3} \left( \frac{m_\chi}{10^8 \text{ GeV}} \right)^5. \quad (5.30)$$

Of course this assumes that the core has not already formed a BH  $G N_{\text{sg}} m_\chi \lesssim R_{\text{QM}}$ . This means that QM collapse is only relevant for DM masses:

$$m_\chi \lesssim \frac{\rho_{\text{WD}}}{T_{\text{WD}}^3} \approx 10^9 \text{ GeV}, \quad (\text{QM affects collapse}), \quad (5.31)$$

for which it is indeed the case that  $N_{\text{col}} = N_{\text{sg}}$ . Note that the extreme densities of the DM core (5.30) are not necessarily problematic as we always assume the DM is point-like with no substructure; however, with an explicit model one should be wary of higher dimension operators modifying the collapse dynamics by potentially triggering new interactions.

**Fermionic DM** If DM is a fermion, (5.29) is precisely the radius of stabilization due to degeneracy pressure. A degenerate DM core will sit at  $R_{\text{QM}}$  until it collects an additional

number of particles  $N \gg N_{\text{sg}}$  and subsequently shrinks as  $r \sim \frac{1}{Gm_\chi^3 N^{1/3}}$ . Note that additional captured DM particles are still able to dissipate energy and decrease their orbital sizes below the thermal radius under the gravitational influence of the compact core. For DM masses (5.31) the collection time  $\frac{N}{\Gamma_{\text{cap}}}$  is always far greater than the cooling time  $t_{\text{col}}$  (5.26), and thus the shrinking proceeds adiabatically at a rate  $\Gamma_{\text{cap}}$ .

Fermi pressure is capable of supporting a self-gravitating degenerate DM core until it exceeds the Chandrasekhar limit

$$N_{\text{Cha}}^{\text{f}} \sim \frac{M_{\text{pl}}^3}{m_\chi^3} \approx 2 \cdot 10^{33} \left( \frac{m_\chi}{10^8 \text{ GeV}} \right)^{-3}. \quad (5.32)$$

Thus the fermi degenerate core will collapse to a BH as long as

$$N_{\text{Cha}}^{\text{f}} < N_{\text{life}}, \quad (\text{BH from degenerate core}), \quad (5.33)$$

which is the case for  $m_\chi \gtrsim 10^6 \text{ GeV}$ , assuming  $\Gamma_{\text{cap}} = \Gamma_{\text{trans}}$  and  $\rho_\chi = 0.4 \frac{\text{GeV}}{\text{cm}^3}$ . We note that the presence of attractive e.g., Yukawa-type DM self-interactions can drastically reduce the critical number required to overcome Fermi pressure (see [164]), though we do not consider this possibility here.

**Bosonic DM** If DM is a boson, once the DM core collapses to (5.29) it starts populating a BEC. Further collapse results in increasing the number of particles in the BEC, with the density of the non-condensed particles fixed at  $\rho_{\text{QM}}$ , see [160] for details. The size of the BEC is initially set by the gravitational potential of the enveloping self-gravitating sphere, and particles in the BEC have a velocity set by the uncertainty principle:

$$\begin{aligned} r_{\text{BEC}} &\sim \left( \frac{1}{G\rho_{\text{QM}}m_\chi^2} \right)^{1/4} \approx 10^{-16} \text{ cm} \left( \frac{m_\chi}{10^8 \text{ GeV}} \right)^{-7/4}, \\ v_{\text{BEC}} &\sim \frac{1}{m_\chi r_{\text{BEC}}} \approx 10^{-6} \left( \frac{m_\chi}{10^8 \text{ GeV}} \right)^{3/4}. \end{aligned} \quad (5.34)$$

The BEC sits at  $r_{\text{BEC}}$  until it becomes self-gravitating at a number:

$$N_{\text{BEC, sg}} \sim \frac{\rho_{\text{QM}} r_{\text{BEC}}^3}{m_\chi} \approx 2 \cdot 10^{16} \left( \frac{m_\chi}{10^8 \text{ GeV}} \right)^{-5/4}. \quad (5.35)$$

A self-gravitating BEC will continue to add particles, and in the process shrink as  $r_{\text{BEC}} \sim \frac{1}{Gm_\chi^3 N}$ . The rate at which DM particles are added to the BEC is set by the rate at which the non-condensed DM core sheds the excess gravitational energy. The time to condense a number of particles  $N \ll N_{\text{sg}}$  is:

$$t_{\text{BEC}}(N) \sim \frac{N}{N_{\text{sg}}} t_{\text{col}}(R_{\text{QM}}). \quad (5.36)$$

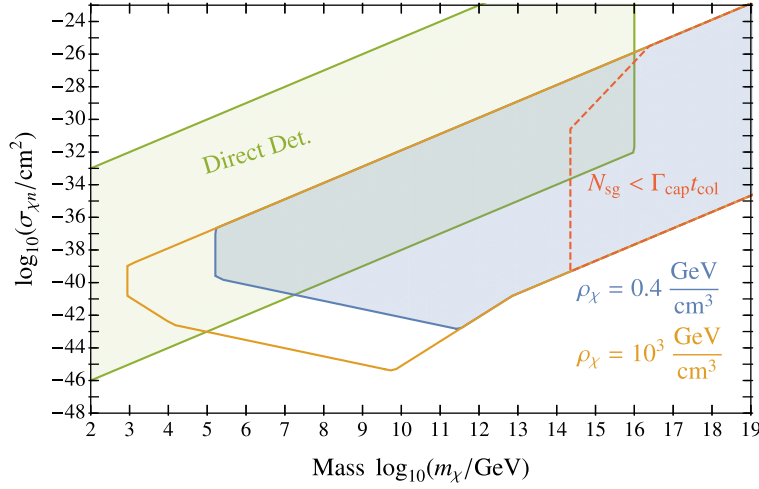


Figure 5.1: Parameter space  $\{m_\chi, \sigma_{\chi n}\}$  of asymmetric DM in which a DM core forms and collapses within  $\tau_{\text{WD}} \approx 5$  Gyr in a WD of local DM density  $\rho_\chi$ . See text for details.

Note that the typical DM velocity in the non-condensed DM sphere at this stage is:

$$v_{\text{col}}(R_{\text{QM}}) \sim \sqrt{\frac{GN_{\text{sg}}m_\chi}{R_{\text{QM}}}} \approx 0.3 \left( \frac{m_\chi}{10^8 \text{ GeV}} \right)^{1/3}. \quad (5.37)$$

The pressure induced by the uncertainty principle is capable of supporting the self-gravitating sphere of DM particles until it exceeds the so-called bosonic Chandrasekhar limit:

$$N_{\text{Cha}}^{\text{b}} \sim \frac{M_{\text{pl}}^2}{m_\chi^2} \approx 10^{22} \left( \frac{m_\chi}{10^8 \text{ GeV}} \right)^{-2}, \quad (5.38)$$

which is far less than  $N_{\text{sg}}$  for all DM masses (5.31). Interestingly, this limit is dramatically affected by even the presence of miniscule DM self-interactions [184]. These may be a generic expectation given the already assumed scattering cross section off nucleon, as emphasized in [163]. In the case of a repulsive  $\lambda|\chi|^4$  interaction potential where  $\lambda > 0$ , no stable configuration exists beyond a critical number

$$N_{\text{Cha, self}}^{\text{b}} \sim \frac{M_{\text{pl}}^2}{m_\chi^2} \left( 1 + \frac{\lambda}{32\pi} \frac{M_{\text{pl}}^2}{m_\chi^2} \right)^{1/2}. \quad (5.39)$$

We find that  $N_{\text{Cha, self}}^{\text{b}}$  is still less than  $N_{\text{sg}}$  as long as  $\lambda \lesssim 10^{-2}$ . An attractive self-interaction could reduce the necessary critical limit, although this is highly model-dependent. From here on, we will use (5.38) as the relevant critical limit.

## Annihilating DM Collapse

Now consider the case of DM with an annihilation cross section  $\sigma_{\chi\chi}$  into SM products, e.g., quarks. We will restrict our attention here to DM masses  $m_\chi \ll \mathcal{E}_{\text{boom}}$  such that multiple annihilations are necessary to ignite a SN. As in the asymmetric case, for simplicity we focus on DM which scatters infrequently,  $\sigma_{\chi A} < \sigma_{\text{ff}}$ .

As described above, the thermalizing DM constitutes a number density of DM throughout the WD volume. Depletion of this in-falling DM is dominated by the total rate of annihilations near the thermal radius:

$$\Gamma_{\text{infall}} \sim \frac{(\Gamma_{\text{cap}} t_2)^2}{R_{\text{th}}^3} \sigma_{\chi\chi} v_{\text{th}}. \quad (5.40)$$

Therefore a DM core at  $R_{\text{th}}$  will steadily collect at a rate roughly  $\Gamma_{\text{cap}}$  as long as

$$\Gamma_{\text{infall}} < \Gamma_{\text{cap}}, \quad (\text{steady DM collection}). \quad (5.41)$$

Of course this collecting DM core is also depleting via annihilations, and will at most reach an equilibrium number

$$N_{\text{eq}} \sim \left( \frac{\Gamma_{\text{cap}} R_{\text{th}}^3}{\sigma_{\chi\chi} v_{\text{th}}} \right)^{1/2}. \quad (5.42)$$

This results in a more stringent condition for self-gravitation:

$$N_{\text{sg}} < \min[N_{\text{life}}, N_{\text{eq}}], \quad (\text{core self-gravitates}). \quad (5.43)$$

If  $N_{\text{sg}} > N_{\text{life}}$  or  $N_{\text{sg}} > N_{\text{eq}}$ , the DM core has either saturated at a number  $N_{\text{eq}}$  or is still continuing to collect at a number  $N_{\text{life}}$ , whichever comes first. In either case if the core does not reach self-gravitation (i.e. (5.43) is not satisfied), we found that the total rate of annihilations within a core subregion of volume  $\lambda_T^3 \ll R_{\text{th}}^3$  is much too small to ignite a SN.

We thus turn to core collapse, during which annihilations become more rapid as the core shrinks. The conditions (5.19), (5.41) and (5.43) on the  $\{m_\chi, \sigma_{\chi\chi} v\}$  parameter space for which a collapse takes place are depicted in Fig. 5.2. Here we have taken a fixed fiducial value of the scattering cross section  $\sigma_{\chi n} = 10^{-39} \text{ cm}^2$ , though the allowed parameter space of collapse in the case of annihilating DM exists for any  $\sigma_{\chi n}$  within the region shown in Fig. 5.1. We have checked that there are no existing constraints at these low DM annihilation cross sections, for instance from DM annihilations in the galactic halo contributing to the observed cosmic ray flux.

As before, a self-gravitating DM core shrinks at a rate set by cooling (5.26). However the core is also annihilating so that  $N(r)$  is decreasing from its initial value  $N_{\text{col}}$  (5.28). When the DM core is at a radius  $r$ , the total rate of annihilations is:

$$\Gamma_{\chi\chi} \sim \frac{N^2}{r^3} \sigma_{\chi\chi} v_{\text{col}}, \quad (5.44)$$



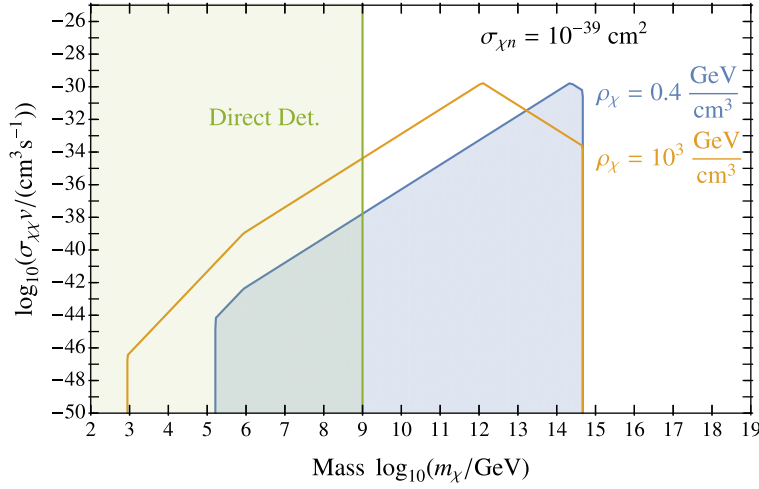


Figure 5.2: Parameter space  $\{m_\chi, \sigma_{\chi\chi}v\}$  of annihilating DM in which a DM core forms and collapses within  $\tau_{\text{WD}} \approx 5$  Gyr in a WD of local DM density  $\rho_\chi$ . We take a fixed value of the DM-nuclei scattering cross section  $\sigma_{\chi n} = 10^{-39} \text{ cm}^2$ . See text for details.

The collapse will initially proceed unscathed, with the number of collapsing particles roughly constant  $N(r) \approx N_{\text{col}}$ , until the characteristic annihilation time  $\frac{N}{\Gamma_{\chi\chi}}$  is of order the collapse time  $t_{\text{col}}$ . The size of the core at this stage is an important scale, which we denote as  $R_{\chi\chi}$ . Note that  $R_{\chi\chi}$  as defined is trivially smaller than  $R_{\text{th}}$  if conditions (5.41) and (5.43) are satisfied. The expression for  $R_{\chi\chi}$  depends on whether this takes place during the “viscous” or “inertial” drag regimes, or in the inelastic scattering regime (5.27). Written in terms of the annihilation cross-section  $\sigma_{\chi\chi}v_{\text{col}}$ , this scales as:

$$R_{\chi\chi} \propto \begin{cases} (\sigma_{\chi\chi}v_{\text{col}})^{1/3} & v_{\text{col}} < v_{\text{ion}} \text{ or } 2 \cdot 10^{-2} < v_{\text{col}} \\ (\sigma_{\chi\chi}v_{\text{col}})^{2/5} & v_{\text{ion}} < v_{\text{col}} < 2 \cdot 10^{-2} \end{cases}. \quad (5.45)$$

Note that  $v_{\text{col}}$  is to be evaluated at  $R_{\chi\chi}$  in these expressions.

Once the DM core collapses to within  $R_{\chi\chi}$ , it begins depleting appreciably. We call this an annihilation burst. Once  $r \lesssim R_{\chi\chi}$ , the continued evolution of the DM core is driven by two competing effects: scatters with the stellar matter drive the core to collapse to smaller radii, as before, but at the same time annihilations drive the core to expand by weakening the gravitational potential. We do not work out this detailed evolution, but rather conservatively consider the constraints only for  $r \gtrsim R_{\chi\chi}$ .

For DM masses (5.31), if  $R_{\chi\chi} > R_{\text{QM}}$  then the core effectively annihilates before any quantum statistics become significant. On the other hand, if  $R_{\chi\chi} < R_{\text{QM}}$  then the core remains roughly intact and can form a fermi degenerate core or BEC, as in the asymmetric DM case. We examine the subsequent evolution of the core in the case  $R_{\chi\chi} < R_{\text{QM}}$ , but with the added presence of annihilations.



**Fermionic DM** If DM is a fermion, a fermi degenerate core will continue to collect DM particles and shrink (and thus the rate of annihilations increases). During this stage, the degenerate DM core can saturate at an equilibrium  $N_{\chi\chi}^f$  when the annihilation rate  $\Gamma_{\chi\chi}$  is of order the shrinking rate set by DM capture  $\Gamma_{\text{cap}}$ . If  $N_{\chi\chi}^f \lesssim N_{\text{sg}}$ , the fermi degenerate core saturates while still roughly at  $R_{\text{QM}}$  (5.29). If  $N_{\chi\chi}^f \gtrsim N_{\text{sg}}$ , the core substantially shrinks before saturating at a number:

$$N_{\chi\chi}^f \sim \frac{\Gamma_{\text{cap}}^{1/3}}{Gm_\chi^3(\sigma_{\chi\chi}v_{\text{col}})^{1/3}}, \quad N_{\chi\chi}^f > N_{\text{sg}}. \quad (5.46)$$

Of course, for sufficiently low annihilation cross section a saturated core may never form in the WD lifetime  $N_{\text{life}} < N_{\chi\chi}^f$  or before forming a BH  $N_{\text{Cha}}^f < N_{\chi\chi}^f$ .

**Bosonic DM** If DM is a boson the core will condense particles into a BEC. As the non-condensed core collapse proceeds at constant density, it will never burst as the rate of annihilations in the enveloping sphere only decreases. However the BEC can saturate at an equilibrium number when the annihilation rate in the compact region becomes of order the condensation rate given by (5.36). We have checked that this saturation is never reached before the BEC self-gravitates at a number (5.35). Subsequently the BEC adds particles from the core and shrinks (and the rate of annihilations in the BEC increases). The self-gravitating BEC then either saturates at a number

$$N_{\chi\chi}^b \sim \left( \frac{N_{\text{sg}}}{t_{\text{col}}(R_{\text{QM}})G^3m_\chi^9\sigma_{\chi\chi}v_{\text{BEC}}} \right)^{1/5}, \quad N_{\chi\chi}^b > N_{\text{BEC, sg}}. \quad (5.47)$$

or first reaches  $N_{\text{Cha}}^b$  when annihilations are negligible and forms a BH.

## Endgame

There are many possible outcomes of the DM core collapse in a WD. For asymmetric DM the core can collapse to a mini BH, either directly or by first forming a fermi degenerate core or populating a BEC. As detailed in Sec. 5.4, such a BH can ignite a SN by emission of Hawking radiation or, as we motivate, possibly even during its accretion. For annihilating DM the core annihilates at an increasing rate until collapsing to  $R_{\chi\chi}$ , at which point it is effectively annihilating an  $\mathcal{O}(1)$  fraction. As detailed in Sec. 5.5, this large number of rapid annihilations can even ignite a SN before the core reaches  $R_{\chi\chi}$ .

It is also the case that the DM core is directly heating the WD via nuclear scatters. This may be sufficient to ignite a SN, as first calculated by [118]. We estimate the total energy deposited by a collapsing core of size  $r$  inside a trigger region  $\lambda_T^3$  during a time  $\tau_{\text{diff}}$  as:

$$\mathcal{E}_{\chi A}(r) \sim N_{\text{col}}m_\chi v_{\text{col}}^2 \left( \frac{\tau_{\text{diff}}}{t_{\text{col}}} \right) \cdot \min \left[ 1, \left( \frac{\lambda_T}{r} \right)^3 \right]. \quad (5.48)$$

In considering this process, [118] additionally required that (1) the DM core be self-thermalized (e.g., due to DM-DM self interactions) and (2) the core must uniformly heat a trigger region  $\lambda_T^3$ , thus restricting the analysis to core sizes  $r \gtrsim \lambda_T$ . Neither of these requirements are necessary, however. While a deposited energy well inside the trigger region may not immediately ignite a conductive flame as per [114], it will eventually if the energy is sufficiently large (5.2) once the heat has diffused out to a size  $\sim \lambda_T$  (see [3] for a more detailed discussion of this evolution). This observation allows the derived constraints of [118] to be extended to larger DM masses: we simply require  $\mathcal{E}_{\chi A} \gtrsim \mathcal{E}_{\text{boom}}$  satisfies the condition (5.2) in order for scattering to ignite a SN.

We emphasize that the heat deposited in the stellar matter during a DM collapse would be drastically affected by the presence of an additional cooling mechanism which drives the collapse, e.g., emitting dark radiation. In particular, if such a cooling mechanism is present and efficient in a collapsing core, ignition due to heating by nuclear scatters as in [118] might not occur. As we show in Sec. 5.4 and Sec. 5.5, however, most collapsing DM cores would still ignite a SN from BH formation or annihilations. For this reason, while we show the extended constraints on DM-nuclear scatters from (5.48), we will also consider and show the consequences of core collapse to smaller radii, below the size at which nuclear scatters (as the sole cooling mechanism) would deposit sufficient energy to be constrained.

## 5.4 Black hole-induced SN

As described in Sec. 5.3, a BH formed by DM collapse will have an initial mass (shown in Fig. 5.3):

$$M_{\text{BH}} \sim \begin{cases} N_{\text{Cha}}^{\text{f}} m_{\chi} & m_{\chi} \lesssim 10^9 \text{ GeV} & \text{fermionic DM} \\ N_{\text{Cha}}^{\text{b}} m_{\chi} & m_{\chi} \lesssim 10^9 \text{ GeV} & \text{bosonic DM} \\ GN_{\text{col}} m_{\chi} & m_{\chi} \gtrsim 10^9 \text{ GeV} \end{cases} . \quad (5.49)$$

Note that any such BH will necessarily have some angular momentum. The DM core initially inherits its angular velocity from the rotating WD, though loses angular momentum to the stellar medium as it cools and collapses. We find the dimensionless spin parameter of the initial BH is always small  $\frac{J_{\text{BH}}}{GM_{\text{BH}}^2} \lesssim 10^{-2}$ , assuming a WD angular velocity of  $\Omega_{\text{WD}} \approx 0.01 \text{ Hz}$ . Thus the newly formed BH is approximately Schwarzschild, and has a radius:

$$R_{\text{BH}} = 2GM_{\text{BH}} \approx 3 \cdot 10^{-5} \text{ cm} \left( \frac{M_{\text{BH}}}{10^{47} \text{ GeV}} \right). \quad (5.50)$$

### Fate of a BH

It is generally believed [185] that BHs have a temperature

$$T_{\text{BH}} = \frac{1}{4\pi R_{\text{BH}}} \approx 6 \text{ MeV} \left( \frac{M_{\text{BH}}}{10^{39} \text{ GeV}} \right)^{-1}, \quad (5.51)$$

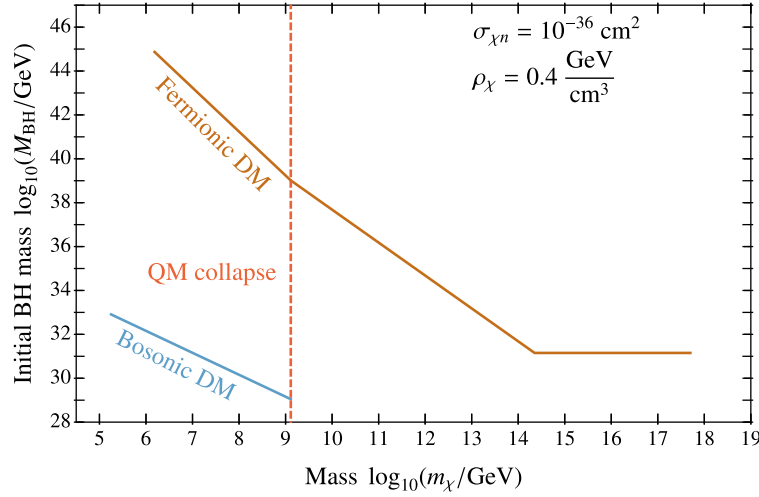


Figure 5.3: Initial black hole mass formed by DM core collapse in a WD. We take a representative value of the scattering cross section, though  $M_{\text{BH}}$  is independent of  $\sigma_{\chi n}$  except for large DM masses where  $N_{\text{sg}} < \Gamma_{\text{cap}} t_{\text{col}}$ . As plotted  $M_{\text{BH}}$  cuts-off at points where a DM core does not even form or collapse, or where a fermi degenerate core does not have time to collect a Chandrasekhar number  $N_{\text{Cha}}^{\text{f}}$ .

and lose mass by emitting particles at a rate

$$\left( \frac{dM_{\text{BH}}}{dt} \right)_{\text{HR}} = \frac{\alpha}{G^2 M_{\text{BH}}^2}, \quad (5.52)$$

where  $\alpha(M_{\text{BH}})$  encodes the different particle emission rates, roughly increasing as the BH temperature exceeds the mass threshold of a new species. Detailed calculation [186] finds  $\alpha \approx 2.8 \cdot 10^{-4}$  for  $T_{\text{BH}} \lesssim \text{MeV}$ , accounting for emission of photons, gravitons, and three neutrino species. Counting only experimentally verified SM degrees of freedom, the emission rate effectively asymptotes to  $\alpha \approx 4.1 \cdot 10^{-3}$  for  $T_{\text{BH}} \gtrsim 100 \text{ GeV}$  [187]. Thus an evaporating BH (by this we mean a BH which only Hawking radiates without any accretion)<sup>3</sup> has a lifetime less than  $\tau_{\text{WD}} \approx 5 \text{ Gyr}$  if:

$$M_{\text{BH}} \lesssim 2 \cdot 10^{38} \text{ GeV} \quad (\text{evaporate in } \tau_{\text{WD}}). \quad (5.53)$$

The BH primarily accretes nuclear matter and additional DM particles: which dominates depends on the BH mass, or more precisely the DM parameters. In the hydrodynamic spherical so-called Bondi approximation, the former is given by

$$\left( \frac{dM_{\text{BH}}}{dt} \right)_{\text{WD}} = 4\pi\lambda \left( \frac{GM_{\text{BH}}}{c_s^2} \right)^2 \rho_{\text{WD}} c_s, \quad (5.54)$$

<sup>3</sup>An evaporating BH loses angular momentum rapidly and has a decreasing spin parameter—thus rotation is negligible throughout the evaporation [188].

where  $c_s \approx 2 \cdot 10^{-2}$  is the sound speed (approximated from numerical calculations in [189]), and  $\lambda \sim \mathcal{O}(1)$  [190].

The accretion of DM potentially has two contributions. Under the influence of the BH gravitational potential, individual DM particles will continue reducing their orbit size below the thermal radius by scattering with the stellar medium. Once it crosses the angular momentum barrier  $4GM_{\text{BH}}$ , the DM will rapidly fall into the BH [190]. A steady state is soon achieved after the BH is formed where DM feeds the BH at a rate set by the capture rate:

$$\left(\frac{dM_{\text{BH}}}{dt}\right)_\chi = \Gamma_{\text{cap}} m_\chi \quad (5.55)$$

There may also be large overdensity of DM particles in the vicinity of the newly formed BH, which is likely if the DM core collapses with non-uniform density. In the collisionless spherical approximation [190], a DM population with density  $\rho_\infty$  and velocity  $v_\infty$  far from the BH accretes at a rate:

$$\left(\frac{dM_{\text{BH}}}{dt}\right)_\chi = \frac{16\pi\rho_\infty G^2 M_{\text{BH}}^2}{v_\infty}. \quad (5.56)$$

Such accretion is especially relevant for bosonic DM if the BH is formed from a compact BEC within an enveloping non-condensed DM core [160]. For our purposes we will only consider (5.56) in this scenario, where  $\rho_\infty$  is given by the very large density (5.30) and  $v_\infty$  is given by (5.37).

The fate of a BH is determined by:

$$\frac{dM_{\text{BH}}}{dt} = -\left(\frac{dM_{\text{BH}}}{dt}\right)_{\text{HR}} + \left(\frac{dM_{\text{BH}}}{dt}\right)_{\text{WD}} + \left(\frac{dM_{\text{BH}}}{dt}\right)_\chi. \quad (5.57)$$

We first consider BHs that are not formed from a BEC. Without DM accretion, we find Hawking evaporation beats Bondi accretion, i.e.,  $\left(\frac{dM_{\text{BH}}}{dt}\right)_{\text{HR}} > \left(\frac{dM_{\text{BH}}}{dt}\right)_{\text{WD}}$  at masses:

$$M_{\text{BH}} \lesssim 10^{38} \text{ GeV}, \quad (\text{Hawking beats Bondi}). \quad (5.58)$$

Including the steady accretion of DM (5.55), we find Hawking evaporation beats the largest possible DM accretion, i.e.,  $\left(\frac{dM_{\text{BH}}}{dt}\right)_{\text{HR}} > \left(\frac{dM_{\text{BH}}}{dt}\right)_\chi$  when  $\Gamma_{\text{cap}} = \Gamma_{\text{trans}}$  at masses

$$M_{\text{BH}} \lesssim 2 \cdot 10^{35} \text{ GeV}, \quad (\text{Hawking beats DM}), \quad (5.59)$$

where Hawking also clearly beats Bondi. The critical mass  $M_{\text{crit}}$  at which  $dM_{\text{BH}}/dt = 0$  depends on the strength of the steady DM accretion (5.55), and for the relevant DM parameter space lies in the range:

$$M_{\text{crit}} \approx 2 \cdot 10^{35} - 10^{38} \text{ GeV}, \quad (5.60)$$

where the upper end of this range holds when Bondi dominates the accretion, and all lower values apply when steady DM accretion (5.55) dominates.

We now consider the timescales involved in accreting or evaporating, which can be estimated by the characteristic time:

$$\tau_{\text{BH}} \sim \frac{M_{\text{BH}}}{dM_{\text{BH}}/dt}. \quad (5.61)$$

If the BH is evaporating,  $\tau_{\text{BH}} \propto M_{\text{BH}}^3$  and is set by the time spent at the largest BH mass, i.e. the initial BH mass. If the BH is dominantly accreting by Bondi then  $\tau_{\text{BH}} \propto M_{\text{BH}}^{-1}$  is set by the time spent at the smallest BH mass. If, however, the BH is dominantly accreting by DM (5.55) then  $\tau_{\text{BH}} \propto M_{\text{BH}}$  is instead set by the time spent at the largest BH mass—this is the BH mass at which Bondi accretion takes over  $10^{38} \lesssim M_{\text{BH}} \lesssim 10^{41}$  GeV (depending on the capture rate  $\Gamma_{\text{cap}}$ ). Miraculously, we find  $\tau_{\text{BH}} \approx \text{Gyr}$  for BH masses  $M_{\text{BH}} \approx 10^{38}$  GeV, coinciding with the upper end of (5.60) where Bondi accretion becomes of order the Hawking evaporation. This can also be seen from the fact that  $M_{\text{crit}}$  (5.60) lies *just* below the BH mass necessary to evaporate within  $\tau_{\text{WD}} \approx 5$  Gyr in the absence of any accretion (5.53). Thus it is clear that whether the BH is evaporating or accreting, it will necessarily do so in a characteristic time less than a Gyr.

Returning to the case of BHs formed from a BEC, we find that the DM accretion of the non-condensed enveloping DM core (5.56) in fact beats Hawking evaporation over the entire DM mass range of interest. Note that this outcome is strikingly different from the analogous process in a NS, where it has been found that such BHs always dominantly evaporate [160]. The difference arises from the fact that the density of the DM core (5.30) is significantly smaller at NS densities/temperatures and at the lower DM masses considered by [160].

We now briefly address the question: is Bondi always a valid estimate for the accretion of nuclear matter onto the BH? As is well-known, accretion could be in the Eddington-limited regime: this occurs when the radiation produced by in-falling matter exerts a significant pressure so as to back-react on the accretion. In the spherical approximation, this yields a maximum luminosity:

$$L_{\text{edd}} = \frac{4\pi G M_{\text{BH}} m_{\text{ion}}}{\sigma}, \quad (5.62)$$

where  $\sigma$  is the dominant interaction by which outgoing radiation transfers momentum to the in-falling matter. Assuming photon energies near the horizon  $\omega \gtrsim \text{MeV}$ , this is either set by hard Compton scattering off electrons  $\sigma \sim \frac{\alpha^2}{m_e \omega} \sim 100 \text{ mb} \left(\frac{\omega}{\text{MeV}}\right)^{-1}$  or inelastic photo-nuclear interactions off ions  $\sigma \sim \text{mb}$  (see [3] for details). Accretion is Eddington-limited if  $\epsilon \cdot (dM_{\text{BH}}/dt)_{\text{WD}}$  exceeds  $L_{\text{edd}}$ , where  $\epsilon$  is the radiation efficiency. If we conservatively take  $\epsilon \sim 0.1$ , we find Bondi accretion is not Eddington-limited for BH masses less than  $M_{\text{BH}} \lesssim 10^{40}$  GeV. Note that even if the accretion is Eddington-limited at larger BH masses, the timescale  $\tau_{\text{BH}}$  then becomes independent of  $M_{\text{BH}}$  and is still much less than a Gyr.

The accretion could also be stalled by the stellar rotation: this occurs when the in-falling matter possesses excess angular momentum that must be dissipated to accrete, e.g., by viscous stresses during a slow phase of disk accretion [190]. [162] examines the effect of rotations for mini BHs in NSs, concluding that kinematic viscosity can maintain Bondi spherical accretion as long as the BH mass is sufficiently small. Based on the analysis of [162],

we crudely estimate that Bondi accretion would hold for  $M_{\text{BH}} \lesssim 10^{46}$  GeV, assuming a (conservative choice of) WD viscosity [191]. Even if the BH accretion is stalled beyond this point we suspect the accretion timescale is still much smaller than a Gyr, though a detailed understanding is beyond the scope of this work.

## Constraints

**Hawking.** The Hawking radiation emitted by a BH will ignite a SN if

$$\mathcal{E}_{\text{BH}} \sim \frac{\alpha}{G^2 M_{\text{BH}}^2} \cdot \min[\tau_{\text{diff}}, \tau_{\text{BH}}] \quad (5.63)$$

satisfies the condition (5.2)  $\mathcal{E}_{\text{BH}} \gtrsim \mathcal{E}_{\text{boom}}$ . If the BH is evaporating, then  $\tau_{\text{BH}}$  is just its remaining lifetime (which is greater than  $\tau_{\text{diff}}$  for BH masses  $M_{\text{BH}} \gtrsim 10^{29}$  GeV). Even if a BH is technically accreting, it is possible to ignite a SN by the large amount of Hawking radiation emitted during its infancy. In this case, one can check that (5.63) still approximates the dominant contribution to the total energy emitted during a time  $\tau_{\text{diff}}$ .

Assuming  $\tau_{\text{diff}} \ll \tau_{\text{BH}}$ , applicable for all starting BH masses we consider, Hawking is explosive at BH masses:

$$M_{\text{BH, boom}} \approx 2 \cdot 10^{35} \text{ GeV}. \quad (5.64)$$

Of course, any DM core that results in a BH initially less than  $M_{\text{BH, boom}}$  ignites a SN upon formation. In addition, DM cores that result in a BH initially greater than  $M_{\text{BH, boom}}$  but less than the critical threshold  $M_{\text{crit}}$  evaporate and eventually ignite a SN within a Gyr. Coincidentally, any BH initially greater than  $M_{\text{crit}}$  will not ignite a SN via Hawking but will instead accrete—this is evident from the fact that (5.64) lies just below the lower end of the critical threshold (5.60). However this is notably not the case for accreting BHs formed from a BEC: we have checked that all BHs formed from a BEC *immediately* ignite a SN by Hawking despite the large accretion rate from the large enveloping DM density.

**Accretion.** Finally, we comment on the final outcome of an accreting BH. It is conservative to suppose that such a BH simply eats the star. However, it is plausible that accreting BHs in WDs ignite SN once they grow sufficiently large. We can think of at least two potential mechanisms for this:

(1) The flow of stellar matter into the BH leads to the formation of a sonic horizon  $R_s \sim GM_{\text{BH}}/c_s^2 \sim 10^4 R_{\text{BH}}$ , with supersonic flow as the matter enters free-fall near the BH. The kinetic energy of a carbon ion at the sonic horizon is  $m_{\text{ion}} c_s^2 \sim \text{MeV}$ , increasing as it falls inward. It is reasonable to suppose that the flow inside the sonic horizon is not perfectly radial, in which case this violent swarm of carbon ions may ignite thermonuclear fusion. BH masses  $M_{\text{BH}} \gtrsim 10^{43}$  GeV have sonic horizons  $R_s \gtrsim \lambda_T$ . Assuming substantial non-radial flow, such BHs may then have carbon ions colliding at large enough energies to overcome the coulomb barrier and initiate fusion over a large region. As this fusion is happening within the

sonic horizon, a resulting fusion front would need to propagate out as a supersonic shockwave (e.g., a so-called detonation front [125]) in order to ignite the rest of the star.

(2) Inflow onto the BH also increases the density of stellar matter near the BH, for instance by roughly a factor  $\sim 10 - 100$  at the sonic horizon [190]. This increased density may be sufficient, even at low temperatures, to ignite the star outside the sonic horizon through pycnonuclear fusion without the need for a supersonic shockwave (or inside the sonic horizon, with an accompanying supersonic fusion front.) Runaway pycnonuclear fusion begins when a sufficiently large region of carbon achieves a critical density  $\sim 10^{10} \text{ g/cm}^3$  [125], which is a factor  $\sim 30$  greater than our chosen central density. Note that the corresponding pycnonuclear trigger size  $\lambda_P$  may be different from the thermonuclear trigger size  $\lambda_T$  as the rates of fusion and diffusion depend on density and temperature, and both may be modified by dynamics near the BH. However, if we simply assume  $\lambda_P \sim \lambda_T \sim 10^{-5} \text{ cm}$ , then large BH masses  $M_{\text{BH}} \gtrsim 10^{44} \text{ GeV}$  would have a sonic horizon  $R_s \gg \lambda_P$ , and could thus potentially ignite a SN via subsonic fusion front.

To confirm either of these mechanisms leads to ignition would require more detailed numerical calculations, which we do not attempt here. In any case, whether an accreting BH eats the star or ignites a SN, we are able to constrain any such BHs by the existence of observed WDs given that the accretion timescale is less than a Gyr.

To summarize, BHs formed by DM core collapse will either ignite a SN by Hawking radiation, or accrete and subsequently eat the star or ignite a SN. The resulting constraints on DM parameters are shown in Fig. 5.4 (fermionic DM) and Fig. 5.5 (bosonic DM). For fermionic DM these constraints extend well beyond those previously derived which consider BH formation/accretion in NSs, and are thus complementary. For bosonic DM these constraints are entirely new—in the DM mass range of interest, there are in fact no bounds due to BH formation in NSs (see [160] for details). We also show the constraints from DM-nuclei scatters igniting a SN during core collapse at any point before formation of a BH (or a fermi degenerate core or BEC).

## 5.5 Annihilation-induced SN

A collapsing core of annihilating DM has an increasing annihilation rate, and effectively depletes  $\mathcal{O}(1)$  (“bursts”) upon shrinking to a size  $r \sim R_{\chi\chi}$ . However, even while  $r \gtrsim R_{\chi\chi}$  and the DM core roughly retains its initial number  $N(r) \approx N_{\text{col}}$ , the energy deposited by a small fraction of the core may be significant. We estimate the energy deposited in the large number of annihilations within a trigger region  $\lambda_T^3$  and diffusion time  $\tau_{\text{diff}}$  for  $r \gtrsim R_{\chi\chi}$ :

$$\mathcal{E}_{\chi\chi}(r) \sim m_\chi \frac{N_{\text{col}}^2}{r^3} \sigma_{\chi\chi} v_{\text{col}} \tau_{\text{diff}} \cdot \min \left[ 1, \left( \frac{\lambda_T}{r} \right)^3 \right]. \quad (5.65)$$

This is sufficient to ignite a SN if it satisfies  $\mathcal{E}_{\chi\chi} \gtrsim \mathcal{E}_{\text{boom}}$  (5.2).

As expected, the annihilating core deposits energy more and more rapidly as it shrinks to smaller radii. We can also evaluate the deposited energy (5.65) at the bursting point



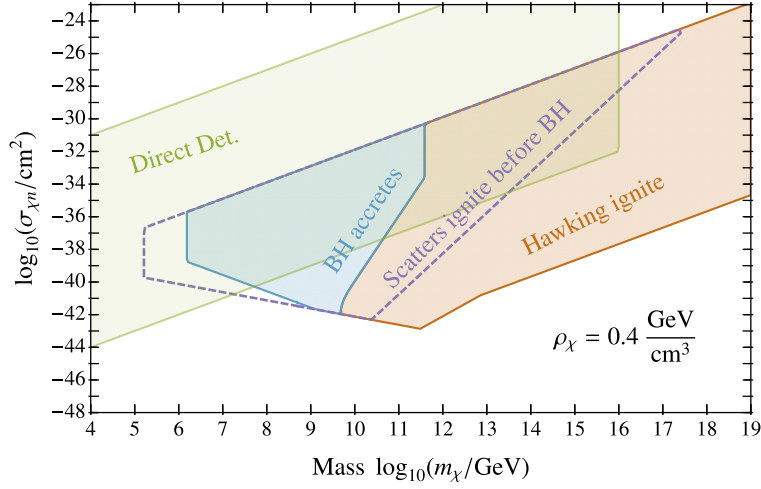


Figure 5.4: Constraints on fermionic asymmetric DM which forms a DM core and collapses to a mini black hole in a WD. The black hole either ignites a supernova via Hawking emission (red) or accretes and eats the star (or possibly ignites a supernova) (blue). Also shown (purple) are the constraints on DM-nuclei scatters igniting a supernova during core collapse before formation of a black hole.

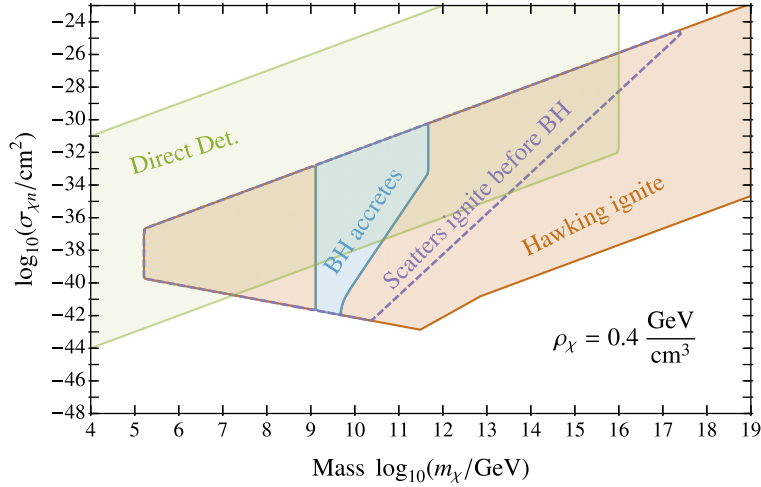


Figure 5.5: Constraints on bosonic asymmetric DM which forms a DM core and collapses to a mini black hole in a WD. The black hole either ignites a supernova via Hawking emission (red) or accretes and eats the star (or possibly ignites a supernova) (blue). Also shown (purple) are the constraints on DM-nuclei scatters igniting a supernova during core collapse before formation of a black hole.



$r \sim R_{\chi\chi}$ . Interestingly for  $R_{\chi\chi} < \lambda_T$ , we find  $\mathcal{E}_{\chi\chi}(R_{\chi\chi})$  scales inversely with annihilation cross section  $\mathcal{E}_{\chi\chi}(R_{\chi\chi}) \propto (\sigma_{\chi\chi} v_{\text{col}})^{-1/5}$  in the regime  $v_{\text{ion}} < v_{\text{col}}(R_{\chi\chi}) < 2 \cdot 10^{-2}$ , i.e. the DM core is more explosive for *lower* annihilation cross section. This is basically a result of the collapsing core focusing and becoming more dense before annihilating  $\mathcal{O}(1)$ , thus making this energy deposition at  $r \sim R_{\chi\chi}$  more violent. It is also interesting that  $\mathcal{E}_{\chi\chi}(R_{\chi\chi})$  scales inversely with DM mass—this is just a result of the greater number of collapsing particles at lower DM masses. Similarly, in the regimes  $v_{\text{col}}(R_{\chi\chi}) < v_{\text{ion}}$  or  $v_{\text{col}}(R_{\chi\chi}) > 2 \cdot 10^{-2}$  we find  $\mathcal{E}_{\chi\chi}(R_{\chi\chi})$  is *independent* of annihilation cross section  $\sigma_{\chi\chi} v_{\text{col}}$ , i.e. the ignition condition  $\mathcal{E}_{\chi\chi}(R_{\chi\chi}) \gtrsim \mathcal{E}_{\text{boom}}$  simply corresponds to an upper bound on DM mass. This variation in the dependence of  $\mathcal{E}_{\chi\chi}$  on  $\sigma_{\chi\chi} v_{\text{col}}$  for different regimes of  $v_{\text{col}}(R_{\chi\chi})$  is responsible for the change in slope of the constrained regions of Figure 5.6 and 5.7 for  $10^{11} \text{ GeV} \lesssim m_\chi \lesssim 10^{12} \text{ GeV}$ .

If the core has not yet ignited a SN by the time it collapses to  $R_{\chi\chi}$ , could it do so afterwards? Although the number of collapsing particles at this point is depleting appreciably, the shrinking of the core may still drive the total rate of annihilations to increase; if so, there is the possibility of igniting a SN at sizes  $r \lesssim R_{\chi\chi}$ . We have estimated that this is not the case. However, as described in Sec. 5.3, the evolution of the annihilating DM core here is somewhat complicated and requires more detailed study—thus we only consider the constraints on annihilations while the DM core is still at sizes  $r \gtrsim R_{\chi\chi}$ .

Of course, the DM core may never annihilate efficiently if it first collapses to a BH  $GN_{\text{col}} m_\chi \gtrsim R_{\chi\chi}$ , though the energy deposited by annihilations before the core shrinks to within the Schwarzschild radius may still be sufficient to ignite a SN. Similarly, if the DM core first reaches the size at which QM effects become important before efficiently annihilating,  $R_{\text{QM}} \gtrsim R_{\chi\chi}$ , then the energy deposited by annihilations at or before this point may still be sufficient to ignite a SN. We have included both of these constraints.

We now consider annihilations igniting SN after formation of a fermi degenerate core or a BEC. As shown in Sec. 5.3, a fermi degenerate core shrinks by capturing additional DM and can saturate once the capture rate is of order the annihilation rate. If this saturation occurs before the core has a chance to shrink much below  $R_{\text{QM}}$ , then it does not ignite a SN. On the other hand if saturation occurs at a number (5.46) much greater than the initial collapsing number, then annihilations in the fermi degenerate core can ignite a SN at a number  $N \lesssim N_{\chi\chi}^f$ . The energy deposited in a trigger region  $\lambda_T^3$  and a diffusion time  $\tau_{\text{diff}}$  is:

$$\mathcal{E}_{\chi\chi}^f(N) \sim m_\chi \frac{N^2}{r^3} \sigma_{\chi\chi} v_{\text{col}}(r) \tau_{\text{diff}} \cdot \min \left[ 1, \left( \frac{\lambda_T}{r} \right)^3 \right], \quad r \sim \frac{1}{G m_\chi^3 N^{1/3}}. \quad (5.66)$$

Thus a shrinking fermi degenerate core ignites a SN through annihilations if (5.66) satisfies  $\mathcal{E}_{\chi\chi}^f \gtrsim \mathcal{E}_{\text{boom}}$  (5.2). Of course this assumes that  $N \lesssim N_{\text{life}}$  and that the core has not yet collapsed to a BH first  $N \lesssim N_{\text{Cha}}^f$ .

Similarly, a self-gravitating BEC that is collecting particles from the enveloping non-condensed core will saturate at a number (5.47). This highly compact BEC can ignite a SN at any number  $N \lesssim N_{\chi\chi}^b$ . The energy deposited by annihilations in the BEC within a time

$\tau_{\text{diff}}$  (or (5.36), whichever is shorter) is simply:

$$\mathcal{E}_{\chi\chi}^f(N) \sim m_\chi \frac{N^2}{r^3} \sigma_{\chi\chi} v_{\text{BEC}}(r) \tau_{\text{diff}} \cdot \min \left[ 1, \left( \frac{\lambda_T}{r} \right)^3 \right], \quad r \sim \frac{1}{Gm_\chi^3 N}. \quad (5.67)$$

and will ignite a SN if it satisfies  $\mathcal{E}_{\chi\chi}^b \gtrsim \mathcal{E}_{\text{boom}}$  (5.2). Of course this also assumes that the BEC has not yet collapsed to a BH  $N \lesssim N_{\text{Cha}}^b$ . Note that the DM annihilation cross section must be extremely small for a shrinking BEC to have not ignited a SN before formation of a BH: the requirement  $\mathcal{E}_{\chi\chi}^b(N_{\text{Cha}}^b) \gtrsim \mathcal{E}_{\text{boom}}$  implies cross sections as low as  $\sigma_{\chi\chi} v_{\text{BEC}} \gtrsim \frac{\mathcal{E}_{\text{boom}}}{M_{\text{pl}}^4 \tau_{\text{diff}}} \sim 10^{-90} \text{ cm}^3/\text{s}$  would ignite a SN through annihilations in the BEC.

To summarize, a collapsing DM core can ignite a SN by a large number of rapid annihilations. These constraints are valid regardless of the nature of the annihilation products as long as they deposit their energy within a trigger sized region. The resulting constraints on DM parameters are shown in Fig. 5.6 (fermionic DM) and Fig. 5.7 (bosonic DM), taking a fixed value of the scattering cross section  $\sigma_{\chi n} = 10^{-39} \text{ cm}^2$ . This roughly corresponds to the interaction strength for  $Z$  boson exchange, i.e., heavy hyper-charged DM (or “WIM-Pzilla”) [192, 193, 194, 195]. We also show the constraint from DM-nuclei scatters igniting a SN during core collapse at any point before DM annihilations would have done so. Note that the particular shape of the bounded regions in Fig. 5.6 and Fig. 5.7 results from the expressions for the energy released in annihilations, e.g. as in (5.65).

For an explicit DM model  $\sigma_{\chi\chi} v$  is typically related to the DM mass in a calculable way, e.g. s-wave annihilation of hyper-charged DM  $\sigma_{\chi\chi} v \sim \alpha_2^2/m_\chi^2$ ,  $\alpha_2$  is the  $SU(2)_L$  gauge coupling. As shown in Fig. 5.6 and Fig. 5.7, we constrain annihilation cross sections many orders of magnitude smaller than this naive estimate. However, this estimate is based upon annihilations of DM its antiparticle  $\chi\bar{\chi} \rightarrow \text{SM}$ , with both existing in roughly equal abundances today. It is straightforward to imagine a scenario in which essentially no  $\bar{\chi}$  particles remain today, and yet  $\chi$  is capable of annihilating itself through a parametrically suppressed interaction. To demonstrate, an explicit DM model of this sort is hypercharged DM with a large vector-like mass and an additional small dimension-5 Majorana mass term. We emphasize though that any DM candidate which can annihilate itself through higher dimension operators may have  $\sigma_{\chi\chi} v$  small enough to be constrained by our results e.g., annihilation to SM fermions through a Planck-suppressed cross section  $\sigma_{\chi\chi} v \sim m_\chi^2/M_{\text{pl}}^4$ .

## 5.6 Discussion

We have studied the possibility of DM core collapse triggering type Ia SN in sub-Chandrasekhar WDs, following up on previous work [3]. Collapse of asymmetric DM can lead to the formation of a mini BH which ignites a SN by the emission of Hawking radiation, and collapse of annihilating DM can lead to large number of rapid annihilations which also ignite a SN. Such processes allow us to place novel constraints on DM parameters, as shown in Fig. 5.4, Fig. 5.5, Fig. 5.6, and Fig. 5.7. These constraints improve on the limits set by terrestrial experiments,

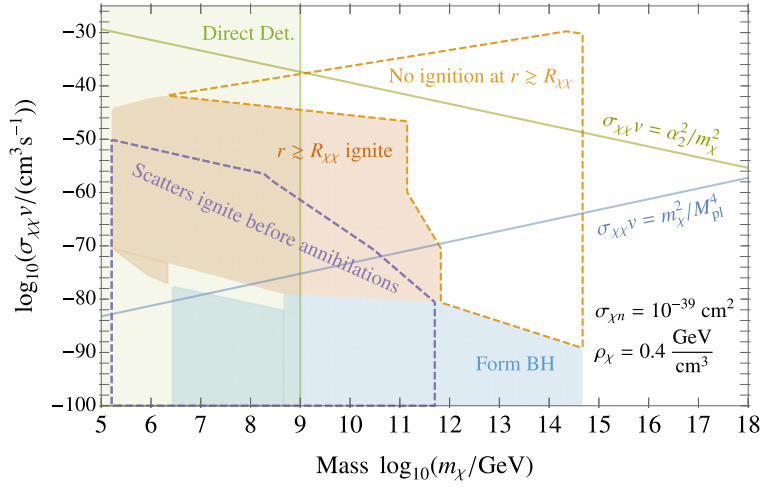


Figure 5.6: Constraints on fermionic DM which forms a DM core and ignites a supernova through annihilations (red). For sufficiently small  $\sigma_{\chi\chi}v$  the core first collapses to a black hole (blue), and is otherwise constrained, see Fig. 5.4. Also shown (purple) are the constraints on DM-nuclei scatters igniting a supernova during core collapse before annihilations could do so.

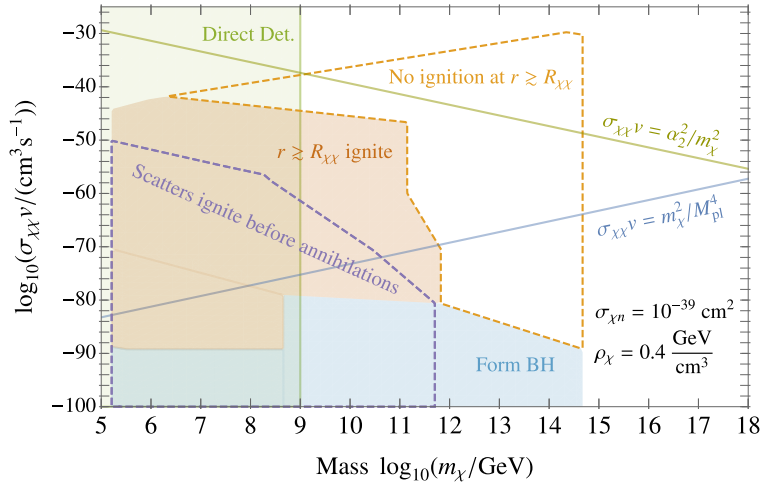


Figure 5.7: Constraints on bosonic DM which forms a DM core and ignites a supernova through annihilations (red). For sufficiently small  $\sigma_{\chi\chi}v$  the core first collapses to a black hole (blue), and is otherwise constrained, see Fig. 5.5. Also shown (purple) are the constraints on DM-nuclei scatters igniting a supernova during core collapse before annihilations could do so.

and they are complementary to previous considerations of DM capture in compact objects. It is interesting to contemplate that the ignition of type Ia SN through the evaporation of mini black holes represents a potential observable signature of Hawking radiation. Further, it is also interesting that the extremely tiny annihilation cross sections constrained in this work, which to our knowledge have no other observable consequences, can nonetheless be capable of igniting a SN.

The processes studied here present a number of opportunities for future work. The DM constraints presented in this paper are based on the existence known, heavy WDs. It would also be interesting to calculate the constraints on DM core collapse scenarios arising from the observed galactic SN rate—these may depend more sensitively on the timescale to form a core, or in the case of BH formation, the evaporation time. In addition, we have restricted our attention here and in [3] to DM candidates which interact with the SM through short-range, elastic nuclear scatters. It would be interesting to broaden our scope to relics with qualitatively different interactions, such as inelastic scatters or radiative processes. DM which can cool via emission of dark radiation will be more susceptible to collapse, and is likely to be more strongly constrained than models possessing only elastic cooling. Another particularly interesting case is electrically charged particles [196] or magnetic monopoles. Ultra-heavy monopoles and anti-monopoles could be captured in a WD and subsequently annihilate, igniting SN—we estimate that such a process can be used to place constraints on the flux of galactic monopoles exceeding current limits [197].

Finally, though we have not touched upon it here, there are many puzzles in our understanding of the origin of type Ia SN and other WD events, such as Ca-rich transients. It is plausible (e.g., see the discussion in [3]) that DM is responsible for a fraction of these events. To this end, it is important to identify the distinguishing features of SN that would originate from DM core collapse (e.g. the lack of a stellar companion) in order to observationally test such tantalizing possibilities.

*Note added:* While this paper was in the final stages of preparation, [198] appeared which has some overlap with this work.

# Bibliography

- [1] Ryan Janish, Vijay Narayan, Surjeet Rajendran, and Paul Riggins. Axion production and detection with superconducting RF cavities. *Phys. Rev.*, D100(1):015036, 2019.
- [2] Jeff A. Dror, Keisuke Harigaya, and Vijay Narayan. Parametric Resonance Production of Ultralight Vector Dark Matter. *Phys. Rev.*, D99(3):035036, 2019.
- [3] Peter W. Graham, Ryan Janish, Vijay Narayan, Surjeet Rajendran, and Paul Riggins. White Dwarfs as Dark Matter Detectors. *Phys. Rev.*, D98(11):115027, 2018.
- [4] Ryan Janish, Vijay Narayan, and Paul Riggins. Type Ia supernovae from dark matter core collapse. *Phys. Rev.*, D100(3):035008, 2019.
- [5] R. D. Peccei and Helen R. Quinn. CP Conservation in the Presence of Instantons. *Phys. Rev. Lett.*, 38:1440–1443, 1977.
- [6] R. D. Peccei and Helen R. Quinn. Constraints Imposed by CP Conservation in the Presence of Instantons. *Phys. Rev.*, D16:1791–1797, 1977.
- [7] Steven Weinberg. A New Light Boson? *Phys. Rev. Lett.*, 40:223–226, 1978.
- [8] Frank Wilczek. Problem of Strong  $P$  and  $T$  Invariance in the Presence of Instantons. *Phys. Rev. Lett.*, 40:279–282, 1978.
- [9] John Preskill, Mark B. Wise, and Frank Wilczek. Cosmology of the Invisible Axion. *Phys. Lett.*, B120:127–132, 1983.
- [10] L. F. Abbott and P. Sikivie. A Cosmological Bound on the Invisible Axion. *Phys. Lett.*, B120:133–136, 1983.
- [11] Michael Dine and Willy Fischler. The Not So Harmless Axion. *Phys. Lett.*, B120:137–141, 1983.
- [12] Peter W. Graham, David E. Kaplan, and Surjeet Rajendran. Cosmological Relaxation of the Electroweak Scale. *Phys. Rev. Lett.*, 115(22):221801, 2015.
- [13] Peter W. Graham, David E. Kaplan, and Surjeet Rajendran. Relaxation of the Cosmological Constant. *Phys. Rev.*, D100(1):015048, 2019.

- [14] Peter Svrcek and Edward Witten. Axions In String Theory. *JHEP*, 06:051, 2006.
- [15] Asimina Arvanitaki, Savas Dimopoulos, Sergei Dubovsky, Nemanja Kaloper, and John March-Russell. String Axiverse. *Phys. Rev.*, D81:123530, 2010.
- [16] P. Sikivie. Experimental Tests of the Invisible Axion. *Phys. Rev. Lett.*, 51:1415–1417, 1983. [,321(1983)].
- [17] K. Van Bibber, N. R. Dagdeviren, S. E. Koonin, A. Kerman, and H. N. Nelson. Proposed experiment to produce and detect light pseudoscalars. *Phys. Rev. Lett.*, 59:759–762, 1987.
- [18] P. Sikivie, D. B. Tanner, and Karl van Bibber. Resonantly enhanced axion-photon regeneration. *Phys. Rev. Lett.*, 98:172002, 2007.
- [19] Klaus Ehret et al. Resonant laser power build-up in ALPS: A ‘Light-shining-through-walls’ experiment. *Nucl. Instrum. Meth.*, A612:83–96, 2009.
- [20] Klaus Ehret et al. New ALPS Results on Hidden-Sector Lightweights. *Phys. Lett.*, B689:149–155, 2010.
- [21] Robin Bahre et al. Any light particle search II Technical Design Report. *JINST*, 8:T09001, 2013.
- [22] F. Hoogeveen. Terrestrial axion production and detection using RF cavities. *Phys. Lett.*, B288:195–200, 1992.
- [23] Joerg Jaeckel and Andreas Ringwald. A Cavity Experiment to Search for Hidden Sector Photons. *Phys. Lett.*, B659:509–514, 2008.
- [24] Fritz Caspers, Joerg Jaeckel, and Andreas Ringwald. Feasibility, engineering aspects and physics reach of microwave cavity experiments searching for hidden photons and axions. *JINST*, 4:P11013, 2009.
- [25] M. Betz, F. Caspers, M. Gasior, M. Thumm, and S. W. Rieger. First results of the CERN Resonant Weakly Interacting sub-eV Particle Search (CROWS). *Phys. Rev.*, D88(7):075014, 2013.
- [26] Peter W. Graham, Igor G. Irastorza, Steven K. Lamoreaux, Axel Lindner, and Karl A. van Bibber. Experimental Searches for the Axion and Axion-Like Particles. *Ann. Rev. Nucl. Part. Sci.*, 65:485–514, 2015.
- [27] A. Grassellino, A. Romanenko, O. Melnychuk, D. Sergatskov, Y. Trenikhina, A. Crawford, A. Rowe, M. Wong, T. Khabiboulline, and F. Barkov. Nitrogen and argon doping of niobium for superconducting radio frequency cavities: a pathway to highly efficient accelerating structures. *Supercond. Sci. Technol.*, 26:102001, 2013.

- [28] Roni Harnik. SRF-based dark matter search: Theory Motivation. <https://indico.fnal.gov/event/19433/session/2/contribution/1/material/slides/0.pdf>.
- [29] Anna Grassellino. SRF-based dark matter search: Experiment. <https://indico.fnal.gov/event/19433/session/2/contribution/2/material/slides/0.pdf>.
- [30] Zachary Bogorad, Anson Hook, Yonatan Kahn, and Yotam Soreq. Probing Axionlike Particles and the Axiverse with Superconducting Radio-Frequency Cavities. *Phys. Rev. Lett.*, 123(2):021801, 2019.
- [31] Saptarshi Chaudhuri, Peter W. Graham, Kent Irwin, Jeremy Mardon, Surjeet Rajendran, and Yue Zhao. Radio for hidden-photon dark matter detection. *Phys. Rev.*, D92(7):075012, 2015.
- [32] Yonatan Kahn, Benjamin R. Safdi, and Jesse Thaler. Broadband and Resonant Approaches to Axion Dark Matter Detection. *Phys. Rev. Lett.*, 117(14):141801, 2016.
- [33] S. Posen, N. Valles, and M. Liepe. RF Magnetic Field Limits of Nb and Nb<sub>3</sub>Sn. *Phys. Rev. Lett.*, 115(4):047001, 2015.
- [34] M. Martinello, A. Grassellino, M. Checchin, A. Romanenko, O. Melnychuk, D. A. Sergatskov, S. Posen, and J. F. Zasadzinski. Effect of Interstitial Impurities on the Field Dependent Microwave Surface Resistance of Niobium. *Appl. Phys. Lett.*, 109:062601, 2016.
- [35] Z. Charifoulline. Residual resistivity ratio (RRR) measurements of LHC superconducting NbTi cable strands. *IEEE Trans. Appl. Supercond.*, 16(2):1188–1191, 2006.
- [36] Ping Ao and David J. Thouless. Berry’s phase and the magnus force for a vortex line in a superconductor. *Phys. Rev. Lett.*, 70:2158–2161, Apr 1993.
- [37] James F. Annett. *Superconductivity, Superfluids and Condensates*. Oxford University Press, 2003.
- [38] Jonathan L. Ouellet. private communication.
- [39] S. M. Anton, J. S. Birenbaum, S. R. O’Kelley, V. Bolkhovsky, D. A. Braje, G. Fitch, M. Neeley, G. C. Hilton, H.-M. Cho, K. D. Irwin, F. C. Wellstood, W. D. Oliver, A. Shnirman, and John Clarke. Magnetic flux noise in dc squids: Temperature and geometry dependence. *Phys. Rev. Lett.*, 110:147002, Apr 2013.
- [40] V. Anastassopoulos et al. New CAST Limit on the Axion-Photon Interaction. *Nature Phys.*, 13:584–590, 2017.
- [41] Peter W. Graham, Jeremy Mardon, Surjeet Rajendran, and Yue Zhao. Parametrically enhanced hidden photon search. *Phys. Rev.*, D90(7):075017, 2014.

- [42] Maxim Pospelov, Adam Ritz, and Mikhail B. Voloshin. Bosonic super-WIMPs as keV-scale dark matter. *Phys. Rev.*, D78:115012, 2008.
- [43] Ann E. Nelson and Jakub Scholtz. Dark Light, Dark Matter and the Misalignment Mechanism. *Phys. Rev.*, D84:103501, 2011.
- [44] Paola Arias, Davide Cadamuro, Mark Goodsell, Joerg Jaeckel, Javier Redondo, and Andreas Ringwald. WISPy Cold Dark Matter. *JCAP*, 1206:013, 2012.
- [45] Haipeng An, Maxim Pospelov, and Josef Pradler. New stellar constraints on dark photons. *Phys. Lett.*, B725:190–195, 2013.
- [46] Jiro Murata and Saki Tanaka. A review of short-range gravity experiments in the LHC era. *Class. Quant. Grav.*, 32(3):033001, 2015.
- [47] Jeff A. Dror, Robert Lasenby, and Maxim Pospelov. New constraints on light vectors coupled to anomalous currents. *Phys. Rev. Lett.*, 119(14):141803, 2017.
- [48] Jeff A. Dror, Robert Lasenby, and Maxim Pospelov. Dark forces coupled to nonconserved currents. *Phys. Rev.*, D96(7):075036, 2017.
- [49] A. Wagner et al. A Search for Hidden Sector Photons with ADMX. *Phys. Rev. Lett.*, 105:171801, 2010.
- [50] Stefan Knirck, Takayuki Yamazaki, Yoshiki Okesaku, Shoji Asai, Toshitaka Idehara, and Toshiaki Inada. First results from a hidden photon dark matter search in the meV sector using a plane-parabolic mirror system. *JCAP*, 1811(11):031, 2018.
- [51] Haipeng An, Maxim Pospelov, Josef Pradler, and Adam Ritz. Direct Detection Constraints on Dark Photon Dark Matter. *Phys. Lett.*, B747:331–338, 2015.
- [52] Itay M. Bloch, Rouven Essig, Kohsaku Tobioka, Tomer Volansky, and Tien-Tien Yu. Searching for Dark Absorption with Direct Detection Experiments. *JHEP*, 06:087, 2017.
- [53] A. Aguilar-Arevalo et al. First Direct-Detection Constraints on eV-Scale Hidden-Photon Dark Matter with DAMIC at SNOLAB. *Phys. Rev. Lett.*, 118(14):141803, 2017.
- [54] Yonit Hochberg, Tongyan Lin, and Kathryn M. Zurek. Detecting Ultralight Bosonic Dark Matter via Absorption in Superconductors. *Phys. Rev.*, D94(1):015019, 2016.
- [55] Philip C. Bunting, Giorgio Gratta, Tom Melia, and Surjeet Rajendran. Magnetic Bubble Chambers and Sub-GeV Dark Matter Direct Detection. *Phys. Rev.*, D95(9):095001, 2017.



- [56] Yonit Hochberg, Yonatan Kahn, Mariangela Lisanti, Kathryn M. Zurek, Adolfo G. Grushin, Roni Ilan, Sinéad M. Griffin, Zhen-Fei Liu, Sophie F. Weber, and Jeffrey B. Neaton. Detection of sub-MeV Dark Matter with Three-Dimensional Dirac Materials. *Phys. Rev.*, D97(1):015004, 2018.
- [57] Simon Knapen, Tongyan Lin, Matt Pyle, and Kathryn M. Zurek. Detection of Light Dark Matter With Optical Phonons in Polar Materials. *Phys. Lett.*, B785:386–390, 2018.
- [58] Masha Baryakhtar, Junwu Huang, and Robert Lasenby. Axion and hidden photon dark matter detection with multilayer optical haloscopes. *Phys. Rev.*, D98(3):035006, 2018.
- [59] Peter W. Graham, David E. Kaplan, Jeremy Mardon, Surjeet Rajendran, and William A. Terrano. Dark Matter Direct Detection with Accelerometers. *Phys. Rev.*, D93(7):075029, 2016.
- [60] Aaron Pierce, Keith Riles, and Yue Zhao. Searching for Dark Photon Dark Matter with Gravitational Wave Detectors. *Phys. Rev. Lett.*, 121(6):061102, 2018.
- [61] Diana López Nacir and Federico R. Urban. Vector Fuzzy Dark Matter, Fifth Forces, and Binary Pulsars. *JCAP*, 1810(10):044, 2018.
- [62] Javier Redondo and Marieke Postma. Massive hidden photons as lukewarm dark matter. *JCAP*, 0902:005, 2009.
- [63] Peter W. Graham, Jeremy Mardon, and Surjeet Rajendran. Vector Dark Matter from Inflationary Fluctuations. *Phys. Rev.*, D93(10):103520, 2016.
- [64] P. A. R. Ade et al. Planck 2015 results. XX. Constraints on inflation. *Astron. Astrophys.*, 594:A20, 2016.
- [65] A. D. Dolgov and D. P. Kirilova. ON PARTICLE CREATION BY A TIME DEPENDENT SCALAR FIELD. *Sov. J. Nucl. Phys.*, 51:172–177, 1990.
- [66] Jennie H. Traschen and Robert H. Brandenberger. Particle Production During Out-of-equilibrium Phase Transitions. *Phys. Rev.*, D42:2491–2504, 1990.
- [67] Lev Kofman, Andrei D. Linde, and Alexei A. Starobinsky. Reheating after inflation. *Phys. Rev. Lett.*, 73:3195–3198, 1994.
- [68] Lev Kofman, Andrei D. Linde, and Alexei A. Starobinsky. Towards the theory of reheating after inflation. *Phys. Rev.*, D56:3258–3295, 1997.
- [69] Raymond T. Co, Lawrence J. Hall, and Keisuke Harigaya. QCD Axion Dark Matter with a Small Decay Constant. *Phys. Rev. Lett.*, 120(21):211602, 2018.

- [70] Gary N. Felder, Lev Kofman, and Andrei D. Linde. Instant preheating. *Phys. Rev.*, D59:123523, 1999.
- [71] Anupam Mazumdar and Saleh Qutub. Nonperturbative overproduction of axionlike particles via derivative interactions. *Phys. Rev.*, D93(4):043502, 2016.
- [72] Prateek Agrawal, Gustavo Marques-Tavares, and Wei Xue. Opening up the QCD axion window. *JHEP*, 03:049, 2018.
- [73] Naoya Kitajima, Toyokazu Sekiguchi, and Fuminobu Takahashi. Cosmological abundance of the QCD axion coupled to hidden photons. *Phys. Lett.*, B781:684–687, 2018.
- [74] Laura Lopez-Honorez, Olga Mena, Sergio Palomares-Ruiz, and Pablo Villanueva-Domingo. Warm dark matter and the ionization history of the Universe. *Phys. Rev.*, D96(10):103539, 2017.
- [75] Vid Iršič et al. New Constraints on the free-streaming of warm dark matter from intermediate and small scale Lyman- $\alpha$  forest data. *Phys. Rev.*, D96(2):023522, 2017.
- [76] P. A. R. Ade et al. Planck 2015 results. XIII. Cosmological parameters. *Astron. Astrophys.*, 594:A13, 2016.
- [77] F. Finelli and Alessandro Gruppuso. Resonant amplification of gauge fields in expanding universe. *Phys. Lett.*, B502:216–222, 2001.
- [78] Kaloian D. Lozanov and Mustafa A. Amin. The charged inflaton and its gauge fields: preheating and initial conditions for reheating. *JCAP*, 1606(06):032, 2016.
- [79] Yohei Ema, Ryusuke Jinno, Kyohei Mukaida, and Kazunori Nakayama. Violent Preheating in Inflation with Nonminimal Coupling. *JCAP*, 1702(02):045, 2017.
- [80] Alejandra Kandus, Kerstin E. Kunze, and Christos G. Tsagas. Primordial magnetogenesis. *Phys. Rept.*, 505:1–58, 2011.
- [81] Patrick B. Greene, Lev Kofman, Andrei D. Linde, and Alexei A. Starobinsky. Structure of resonance in preheating after inflation. *Phys. Rev.*, D56:6175–6192, 1997.
- [82] Gary N. Felder and Igor Tkachev. LATTICEEASY: A Program for lattice simulations of scalar fields in an expanding universe. *Comput. Phys. Commun.*, 178:929–932, 2008.
- [83] Graciela B. Gelmini and Paolo Gondolo. Ultra-cold WIMPs: relics of non-standard pre-BBN cosmologies. *JCAP*, 0810:002, 2008.
- [84] Adrienne L. Erickcek and Kris Sigurdson. Reheating Effects in the Matter Power Spectrum and Implications for Substructure. *Phys. Rev.*, D84:083503, 2011.

- [85] Adrienne L. Erickcek. The Dark Matter Annihilation Boost from Low-Temperature Reheating. *Phys. Rev.*, D92(10):103505, 2015.
- [86] Yan Gong and Xuelei Chen. Cosmological Constraints on Invisible Decay of Dark Matter. *Phys. Rev.*, D77:103511, 2008.
- [87] Lev Kofman, Andrei D. Linde, and Alexei A. Starobinsky. Nonthermal phase transitions after inflation. *Phys. Rev. Lett.*, 76:1011–1014, 1996.
- [88] I. Tkachev, S. Khlebnikov, L. Kofman, and Andrei D. Linde. Cosmic strings from preheating. *Phys. Lett.*, B440:262–268, 1998.
- [89] Nick Kaiser and A. Stebbins. Microwave Anisotropy Due to Cosmic Strings. *Nature*, 310:391–393, 1984.
- [90] Uros Seljak, Anze Slosar, and Patrick McDonald. Cosmological parameters from combining the Lyman-alpha forest with CMB, galaxy clustering and SN constraints. *JCAP*, 0610:014, 2006.
- [91] Xavier Siemens, Vuk Mandic, and Jolien Creighton. Gravitational wave stochastic background from cosmic (super)strings. *Phys. Rev. Lett.*, 98:111101, 2007.
- [92] Thibault Damour and Alexander Vilenkin. Gravitational wave bursts from cosmic strings. *Phys. Rev. Lett.*, 85:3761–3764, 2000.
- [93] Christophe Ringeval and Teruaki Suyama. Stochastic gravitational waves from cosmic string loops in scaling. *JCAP*, 1712(12):027, 2017.
- [94] Jose J. Blanco-Pillado, Ken D. Olum, and Xavier Siemens. New limits on cosmic strings from gravitational wave observation. *Phys. Lett.*, B778:392–396, 2018.
- [95] Yanou Cui, Marek Lewicki, David E. Morrissey, and James D. Wells. Cosmic Archaeology with Gravitational Waves from Cosmic Strings. *Phys. Rev.*, D97(12):123505, 2018.
- [96] R. Smits, M. Kramer, B. Stappers, D. R. Lorimer, J. Cordes, and A. Faulkner. Pulsar searches and timing with the square kilometre array. *Astron. Astrophys.*, 493:1161–1170, 2009.
- [97] Raymond T. Co, Aaron Pierce, Zhengkang Zhang, and Yue Zhao. Dark Photon Dark Matter Produced by Axion Oscillations. *Phys. Rev.*, D99(7):075002, 2019.
- [98] Prateek Agrawal, Naoya Kitajima, Matthew Reece, Toyokazu Sekiguchi, and Fuminobu Takahashi. Relic abundance of dark photon dark matter. *Physics Letters B*, 801:135136, Feb 2020.

- [99] Mar Bastero-Gil, Jose Santiago, Lorenzo Ubaldi, and Roberto Vega-Morales. Vector dark matter production at the end of inflation. *JCAP*, 1904(04):015, 2019.
- [100] D. S. Akerib et al. Results from a search for dark matter in the complete LUX exposure. *Phys. Rev. Lett.*, 118(2):021303, 2017.
- [101] R. Agnese et al. Results from the Super Cryogenic Dark Matter Search Experiment at Soudan. *Phys. Rev. Lett.*, 120(6):061802, 2018.
- [102] Kim Griest, Agnieszka M. Cieplak, and Matthew J. Lehner. Experimental Limits on Primordial Black Hole Dark Matter from the First 2 yr of Kepler Data. *Astrophys. J.*, 786(2):158, 2014.
- [103] Peter W. Graham, Surjeet Rajendran, and Jaime Varela. Dark Matter Triggers of Supernovae. *Phys. Rev.*, D92(6):063007, 2015.
- [104] D. Maoz and F. Mannucci. Type-ia supernova rates and the progenitor problem: A review. *Publications of the Astronomical Society of Australia*, 29(4):447–465, 2012.
- [105] R. Scalzo et al. Type Ia supernova bolometric light curves and ejected mass estimates from the Nearby Supernova Factory. *Mon. Not. Roy. Astron. Soc.*, 440(2):1498–1518, 2014.
- [106] R. A. Scalzo, A. J. Ruiter, and S. A. Sim. The ejected mass distribution of type Ia supernovae: A significant rate of non-Chandrasekhar-mass progenitors. *Mon. Not. Roy. Astron. Soc.*, 445(3):2535–2544, 2014.
- [107] Sean L. McGee and Michael L. Balogh. Constraints on intragroup stellar mass from hostless type ia supernovae. *Monthly Notices of the Royal Astronomical Society: Letters*, 403(1):L79–L83, Mar 2010.
- [108] Ryan J. Foley, P. J. Challis, R. Chornock, M. Ganeshalingam, W. Li, G. H. Marion, N. I. Morrell, G. Pignata, M. D. Stritzinger, J. M. Silverman, and et al. Type iax supernovae: A new class of stellar explosion. *The Astrophysical Journal*, 767(1):57, Mar 2013.
- [109] Mansi M. Kasliwal, S. R. Kulkarni, Avishay Gal-Yam, Peter E. Nugent, Mark Sullivan, Lars Bildsten, Ofer Yaron, Hagai B. Perets, Iair Arcavi, Sagi Ben-Ami, and et al. Calcium-rich gap transients in the remote outskirts of galaxies. *The Astrophysical Journal*, 755(2):161, Aug 2012.
- [110] S. E. Woosley and Daniel Kasen. Sub-chandrasekhar mass models for type ia supernovae. *The Astrophysical Journal*, 734(1):38, May 2011.
- [111] M. Fink, W. Hillebrandt, and F. K. Roepke. Double-detonation supernovae of sub-Chandrasekhar mass white dwarfs. *Astron. Astrophys.*, 2007. [Astron. Astrophys.476,1133(2007)].

- [112] R. Pakmor, M. Kromer, and S. Taubenberger. Helium-ignited violent mergers as a unified model for normal and rapidly declining Type Ia Supernovae. *Astrophys. J.*, 770:L8, 2013.
- [113] P. H. Sell, T. J. Maccarone, R. Kotak, C. Knigge, and D. J. Sand. Calcium-Rich Gap Transients: Tidal Detonations of White Dwarfs? *Mon. Not. Roy. Astron. Soc.*, 450(4):4198–4206, 2015.
- [114] F. X. Timmes and S. E. Woosley. The conductive propagation of nuclear flames. i. degenerate  $c + o$  and  $o + ne + mg$  white dwarfs. *Astrophysical Journal*, 396(2):649–667, 1992.
- [115] Gianfranco Bertone and Malcolm Fairbairn. Compact Stars as Dark Matter Probes. *Phys. Rev.*, D77:043515, 2008.
- [116] Matthew McCullough and Malcolm Fairbairn. Capture of Inelastic Dark Matter in White Dwarves. *Phys. Rev.*, D81:083520, 2010.
- [117] S. C. Leung, M. C. Chu, L. M. Lin, and K. W. Wong. Dark-matter admixed white dwarfs. *Phys. Rev.*, D87(12):123506, 2013.
- [118] Joseph Bramante. Dark matter ignition of type Ia supernovae. *Phys. Rev. Lett.*, 115(14):141301, 2015.
- [119] L. R. Gasques, A. V. Afanasjev, E. F. Aguilera, M. Beard, L. C. Chamon, P. Ring, M. Wiescher, and D. G. Yakovlev. Nuclear fusion in dense matter: Reaction rate and carbon burning. *Phys. Rev.*, C72:025806, 2005.
- [120] F. X. Timmes. [http://cococubed.asu.edu/code\\_pages/coldwd.shtml](http://cococubed.asu.edu/code_pages/coldwd.shtml).
- [121] Raj Gandhi, Chris Quigg, Mary Hall Reno, and Ina Sarcevic. Neutrino interactions at ultrahigh-energies. *Phys. Rev.*, D58:093009, 1998.
- [122] J. A. Formaggio and G. P. Zeller. From eV to EeV: Neutrino Cross Sections Across Energy Scales. *Rev. Mod. Phys.*, 84:1307–1341, 2012.
- [123] William H. Press and David N. Spergel. Capture by the sun of a galactic population of weakly interacting massive particles. *Astrophys. J.*, 296:679–684, 1985. [,277(1985)].
- [124] Andrew Gould. Resonant Enhancements in WIMP Capture by the Earth. *Astrophys. J.*, 321:571, 1987.
- [125] Rudolf Kippenhahn and Alfred Weigert. *Stellar Structure and Evolution*. Springer, New York, 2007.

- [126] Sandro Mereghetti. RX J0648.0–4418: the fastest-spinning white dwarf. In *Proceedings, 13th Marcel Grossmann Meeting on Recent Developments in Theoretical and Experimental General Relativity, Astrophysics, and Relativistic Field Theories (MG13): Stockholm, Sweden, July 1-7, 2012*, pages 2459–2461, 2015.
- [127] S. O. Kepler, S. J. Kleinman, A. Nitta, D. Koester, B. G. Castanheira, O. Giovannini, A. F. M. Costa, and L. Althaus. White Dwarf Mass Distribution in the SDSS. *Mon. Not. Roy. Astron. Soc.*, 375:1315–1324, 2007.
- [128] Kerstin Perez, Charles J. Hailey, and et al. Bauer, Franz E. Extended hard-x-ray emission in the inner few parsecs of the galaxy. *Nature*, 520:646 EP –, 04 2015.
- [129] Fabrizio Nesti and Paolo Salucci. The Dark Matter halo of the Milky Way, AD 2013. *JCAP*, 1307:016, 2013.
- [130] Subrahmanyan Chandrasekhar. *An Introduction to the Study of Stellar Structure*. University of Chicago Press, 1939.
- [131] Cora Dvorkin, Kfir Blum, and Marc Kamionkowski. Constraining Dark Matter-Baryon Scattering with Linear Cosmology. *Phys. Rev.*, D89(2):023519, 2014.
- [132] Tracy R. Slatyer, Nikhil Padmanabhan, and Douglas P. Finkbeiner. CMB Constraints on WIMP Annihilation: Energy Absorption During the Recombination Epoch. *Phys. Rev.*, D80:043526, 2009.
- [133] Tracy R. Slatyer and Chih-Liang Wu. General Constraints on Dark Matter Decay from the Cosmic Microwave Background. *Phys. Rev.*, D95(2):023010, 2017.
- [134] Nikhil Padmanabhan and Douglas P. Finkbeiner. Detecting dark matter annihilation with CMB polarization: Signatures and experimental prospects. *Phys. Rev.*, D72:023508, 2005.
- [135] Alexander Aab et al. The Pierre Auger Cosmic Ray Observatory. *Nucl. Instrum. Meth.*, A798:172–213, 2015.
- [136] Gregory D. Mack, John F. Beacom, and Gianfranco Bertone. Towards Closing the Window on Strongly Interacting Dark Matter: Far-Reaching Constraints from Earth’s Heat Flow. *Phys. Rev.*, D76:043523, 2007.
- [137] E. Aprile et al. First Dark Matter Search Results from the XENON1T Experiment. *Phys. Rev. Lett.*, 119(18):181301, 2017.
- [138] M. Ambrosio et al. Final results of magnetic monopole searches with the MACRO experiment. *Eur. Phys. J.*, C25:511–522, 2002.
- [139] David M. Jacobs, Glenn D. Starkman, and Bryan W. Lynn. Macro Dark Matter. *Mon. Not. Roy. Astron. Soc.*, 450(4):3418–3430, 2015.

- [140] Sidney R. Coleman. Q Balls. *Nucl. Phys.*, B262:263, 1985. [Erratum: Nucl. Phys.B269,744(1986)].
- [141] Alexander Kusenko and Mikhail E. Shaposhnikov. Supersymmetric Q balls as dark matter. *Phys. Lett.*, B418:46–54, 1998.
- [142] Alexander Kusenko, Vadim Kuzmin, Mikhail E. Shaposhnikov, and P. G. Tinyakov. Experimental signatures of supersymmetric dark matter Q balls. *Phys. Rev. Lett.*, 80:3185–3188, 1998.
- [143] Michael Dine and Alexander Kusenko. The Origin of the matter - antimatter asymmetry. *Rev. Mod. Phys.*, 76:1, 2003.
- [144] E. Aprile et al. Dark Matter Search Results from a One Ton-Year Exposure of XENON1T. *Phys. Rev. Lett.*, 121(11):111302, 2018.
- [145] A. Bottino, G. Fiorentini, N. Fornengo, B. Ricci, S. Scopel, and F. L. Villante. Does solar physics provide constraints to weakly interacting massive particles? *Phys. Rev.*, D66:053005, 2002.
- [146] Daniel T. Cumberbatch, Joyce.A. Guzik, Joseph Silk, L. Scott Watson, and Stephen M. West. Light WIMPs in the Sun: Constraints from Helioseismology. *Phys. Rev.*, D82:103503, 2010.
- [147] Mads T. Frandsen and Subir Sarkar. Asymmetric dark matter and the sun. *Phys. Rev. Lett.*, 105:011301, Jul 2010.
- [148] Ilidio Lopes and Joseph Silk. Solar constraints on asymmetric dark matter. *Astrophys. J.*, 757:130, 2012.
- [149] Jordi Casanellas and Ilidio Lopes. First asteroseismic limits on the nature of dark matter. *Astrophys. J.*, 765:L21, 2013.
- [150] Fredrik Sandin and Paolo Ciarcelluti. Effects of mirror dark matter on neutron stars. *Astropart. Phys.*, 32:278–284, 2009.
- [151] Paolo Ciarcelluti and Fredrik Sandin. Have neutron stars a dark matter core? *Phys. Lett.*, B695:19–21, 2011.
- [152] Ang Li, Feng Huang, and Ren-Xin Xu. Too massive neutron stars: The role of dark matter? *Astropart. Phys.*, 37:70–74, 2012.
- [153] I. Goldman, R. N. Mohapatra, S. Nussinov, D. Rosenbaum, and V. Teplitz. Possible Implications of Asymmetric Fermionic Dark Matter for Neutron Stars. *Phys. Lett.*, B725:200–207, 2013.

- [154] Itzhak Goldman and Shmuel Nussinov. Weakly interacting massive particles and neutron stars. *Phys. Rev. D*, 40:3221–3230, Nov 1989.
- [155] Andrew Gould, Bruce T. Draine, Roger W. Romani, and Shmuel Nussinov. Neutron Stars: Graveyard of Charged Dark Matter. *Phys. Lett.*, B238:337–343, 1990.
- [156] Chris Kouvaris and Peter Tinyakov. Constraining asymmetric dark matter through observations of compact stars. *Phys. Rev. D*, 83:083512, Apr 2011.
- [157] Chris Kouvaris and Peter Tinyakov. Excluding light asymmetric bosonic dark matter. *Phys. Rev. Lett.*, 107:091301, Aug 2011.
- [158] Samuel D. McDermott, Hai-Bo Yu, and Kathryn M. Zurek. Constraints on Scalar Asymmetric Dark Matter from Black Hole Formation in Neutron Stars. *Phys. Rev.*, D85:023519, 2012.
- [159] Alan O. Jamison. Effects of gravitational confinement on bosonic asymmetric dark matter in stars. *Phys. Rev.*, D88:035004, 2013.
- [160] Chris Kouvaris and Peter Tinyakov. (not)-constraining heavy asymmetric bosonic dark matter. *Phys. Rev. D*, 87:123537, Jun 2013.
- [161] Joseph Bramante, Keita Fukushima, and Jason Kumar. Constraints on bosonic dark matter from observation of old neutron stars. *Phys. Rev.*, D87(5):055012, 2013.
- [162] Chris Kouvaris and Peter Tinyakov. Growth of Black Holes in the interior of Rotating Neutron Stars. *Phys. Rev.*, D90(4):043512, 2014.
- [163] Nicole F. Bell, Andrew Melatos, and Kalliopi Petraki. Realistic neutron star constraints on bosonic asymmetric dark matter. *Phys. Rev. D*, 87:123507, Jun 2013.
- [164] Chris Kouvaris. Limits on self-interacting dark matter from neutron stars. *Phys. Rev. Lett.*, 108:191301, May 2012.
- [165] Joseph Bramante, Keita Fukushima, Jason Kumar, and Elan Stopnitzky. Bounds on self-interacting fermion dark matter from observations of old neutron stars. *Phys. Rev.*, D89(1):015010, 2014.
- [166] Joseph Bramante and Tim Linden. Detecting Dark Matter with Imploding Pulsars in the Galactic Center. *Phys. Rev. Lett.*, 113(19):191301, 2014.
- [167] Joseph Bramante, Tim Linden, and Yu-Dai Tsai. Searching for dark matter with neutron star mergers and quiet kilonovae. *Phys. Rev.*, D97(5):055016, 2018.
- [168] Raghuveer Garani, Yoann Genolini, and Thomas Hambye. New Analysis of Neutron Star Constraints on Asymmetric Dark Matter. *JCAP*, 1905(05):035, 2019.



- [169] Matthew McCullough and Malcolm Fairbairn. Capture of inelastic dark matter in white dwarves. *Phys. Rev. D*, 81:083520, Apr 2010.
- [170] Dan Hooper, Douglas Spolyar, Alberto Vallinotto, and Nickolay Y. Gnedin. Inelastic dark matter as an efficient fuel for compact stars. *Phys. Rev. D*, 81:103531, May 2010.
- [171] Chris Kouvaris. Wimp annihilation and cooling of neutron stars. *Phys. Rev. D*, 77:023006, Jan 2008.
- [172] Arnaud de Lavallaz and Malcolm Fairbairn. Neutron stars as dark matter probes. *Phys. Rev. D*, 81:123521, Jun 2010.
- [173] Chris Kouvaris and Peter Tinyakov. Can neutron stars constrain dark matter? *Phys. Rev. D*, 82:063531, Sep 2010.
- [174] Gianfranco Bertone and Malcolm Fairbairn. Compact stars as dark matter probes. *Phys. Rev. D*, 77:043515, Feb 2008.
- [175] Masha Baryakhtar, Joseph Bramante, Shirley Weishi Li, Tim Linden, and Nirmal Raj. Dark Kinetic Heating of Neutron Stars and An Infrared Window On WIMPs, SIMPs, and Pure Higgsinos. *Phys. Rev. Lett.*, 119(13):131801, 2017.
- [176] Nirmal Raj, Philip Tanedo, and Hai-Bo Yu. Neutron stars at the dark matter direct detection frontier. *Phys. Rev. D*, 97:043006, Feb 2018.
- [177] Richard Brito, Vitor Cardoso, and Hirotada Okawa. Accretion of dark matter by stars. *Phys. Rev. Lett.*, 115:111301, Sep 2015.
- [178] Richard Brito, Vitor Cardoso, Caio F. B. Macedo, Hirotada Okawa, and Carlos Palenzuela. Interaction between bosonic dark matter and stars. *Phys. Rev.*, D93(4):044045, 2016.
- [179] Richard H. Helm. Inelastic and elastic scattering of 187-mev electrons from selected even-even nuclei. *Phys. Rev.*, 104:1466–1475, Dec 1956.
- [180] E. Aprile et al. Constraining the spin-dependent WIMP-nucleon cross sections with XENON1T. *Phys. Rev. Lett.*, 122(14):141301, 2019.
- [181] Joseph Bramante, Antonio Delgado, and Adam Martin. Multiscatter stellar capture of dark matter. *Phys. Rev.*, D96(6):063002, 2017.
- [182] S. Nussinov. Technocosmology: Could a technibaryon excess provide a 'natural' missing mass candidate. *Phys. Lett.*, 165B:55–58, 1985.
- [183] Kathryn M. Zurek. Asymmetric Dark Matter: Theories, Signatures, and Constraints. *Phys. Rept.*, 537:91–121, 2014.

- [184] Monica Colpi, Stuart L. Shapiro, and Ira Wasserman. Boson stars: Gravitational equilibria of self-interacting scalar fields. *Phys. Rev. Lett.*, 57:2485–2488, Nov 1986.
- [185] S. W. Hawking. Particle Creation by Black Holes. *Commun. Math. Phys.*, 43:199–220, 1975.
- [186] Don N. Page. Particle Emission Rates from a Black Hole: Massless Particles from an Uncharged, Nonrotating Hole. *Phys. Rev.*, D13:198–206, 1976.
- [187] T. N. Ukwatta, D. R. Stump, J. T. Linnemann, J. H. MacGibbon, S. S. Marinelli, T. Yapici, and K. Tollefson. Primordial Black Holes: Observational Characteristics of The Final Evaporation. *Astropart. Phys.*, 80:90–114, 2016.
- [188] Don N. Page. Particle emission rates from a black hole. ii. massless particles from a rotating hole. *Phys. Rev. D*, 14:3260–3273, Dec 1976.
- [189] Shmuel Balberg and Stuart L. Shapiro. The Properties of matter in white dwarfs and neutron stars. 2000.
- [190] Stuart L. Shapiro and Saul A. Teukolsky. *Black Holes, White Dwarfs, and Neutron Stars*. Wiley, New York, 1983.
- [191] Simone Dall’Osso and Elena Maria Rossi. Constraining white dwarf viscosity through tidal heating in detached binary systems. *Mon. Not. Roy. Astron. Soc.*, 443(2):1057–1064, 2014.
- [192] Daniel J. H. Chung, Patrick Crotty, Edward W. Kolb, and Antonio Riotto. Gravitational production of superheavy dark matter. *Phys. Rev. D*, 64:043503, Jul 2001.
- [193] Daniel J. H. Chung, Edward W. Kolb, and Antonio Riotto. Superheavy dark matter. *Phys. Rev. D*, 59:023501, Nov 1998.
- [194] Brian Feldstein, Masahiro Ibe, and Tsutomu T. Yanagida. Hypercharged Dark Matter and Direct Detection as a Probe of Reheating. *Phys. Rev. Lett.*, 112(10):101301, 2014.
- [195] Keisuke Harigaya, Tongyan Lin, and Hou Keong Lou. GUTzilla Dark Matter. *JHEP*, 09:014, 2016.
- [196] Michael A. Fedderke, Peter W. Graham, and Surjeet Rajendran. White Dwarf Bounds on CHAMPs. 2019.
- [197] Ryan Janish, Jacob Leedom, and Vijay Narayan. *to appear*.
- [198] Javier F. Acevedo and Joseph Bramante. Supernovae Sparked By Dark Matter in White Dwarfs. *Phys. Rev.*, D100(4):043020, 2019.
- [199] David A. Hill. *Electromagnetic Fields in Cavities*. Wiley, 2009.

- [200] H. Lübbig K. Grohmann, H.D. Hahlbohm and H. Ramin. Current comparators with superconducting shields. *Cryogenics*, 14:499–502, 1974.
- [201] Kyohei Mukaida and Kazunori Nakayama. Dynamics of oscillating scalar field in thermal environment. *JCAP*, 1301:017, 2013.
- [202] Gordan Krnjaic. Probing Light Thermal Dark-Matter With a Higgs Portal Mediator. *Phys. Rev.*, D94(7):073009, 2016.
- [203] Edward Hardy and Robert Lasenby. Stellar cooling bounds on new light particles: plasma mixing effects. *JHEP*, 02:033, 2017.
- [204] Sergey Alekhin et al. A facility to Search for Hidden Particles at the CERN SPS: the SHiP physics case. *Rept. Prog. Phys.*, 79(12):124201, 2016.
- [205] John Paul Chou, David Curtin, and H. J. Lubatti. New Detectors to Explore the Lifetime Frontier. *Phys. Lett.*, B767:29–36, 2017.
- [206] Vladimir V. Gligorov, Simon Knapen, Michele Papucci, and Dean J. Robinson. Searching for Long-lived Particles: A Compact Detector for Exotics at LHCb. *Phys. Rev.*, D97(1):015023, 2018.
- [207] Jonathan L. Feng, Iftah Galon, Felix Kling, and Sebastian Trojanowski. ForwArd Search ExpeRiment at the LHC. *Phys. Rev.*, D97(3):035001, 2018.
- [208] Vladimir V. Gligorov, Simon Knapen, Benjamin Nachman, Michele Papucci, and Dean J. Robinson. Leveraging the ALICE/L3 cavern for long-lived particle searches. *Phys. Rev.*, D99(1):015023, 2019.
- [209] Stefaan Tavernier. *Experimental Techniques in Nuclear and Particle Physics*. Springer, Berlin, Germany, 2010.
- [210] T.-S. H. Lee and R. P. Redwine. Pion-nucleus interactions. *Annual Review of Nuclear and Particle Science*, 52(1):23–63, 2002.
- [211] Lisa Gerhardt and Spencer R. Klein. Electron and Photon Interactions in the Regime of Strong LPM Suppression. *Phys. Rev.*, D82:074017, 2010.
- [212] Spencer Klein. Suppression of Bremsstrahlung and pair production due to environmental factors. *Rev. Mod. Phys.*, 71:1501–1538, 1999.
- [213] H. Bethe and W. Heitler. On the Stopping of fast particles and on the creation of positive electrons. *Proc. Roy. Soc. Lond.*, A146:83–112, 1934.
- [214] John David Jackson. *Classical electrodynamics; 2nd ed.* Wiley, New York, NY, 1975.
- [215] B. Rossi. *High Energy Particles*. Prentice-Hall, Inc., Englewood Cliffs, NJ, 1952.

# Appendix A

## Estimate of the Axion-induced Fields

In this section we estimate the magnitude of the axion-induced fields, assuming a simple geometry for the production cavity and toroidal conversion region. From the expressions for the axion source field (2.6) and effective current (2.9), the axion-induced magnetic field at a detection point  $\vec{r}$  is generally of the form:

$$\vec{B}_a(\vec{r}) = \frac{i\omega g^2}{(4\pi)^2} e^{i\omega t} \int_{\text{pc}} d^3\vec{y} \int_{\text{cr}} d^3\vec{x} \left\{ \vec{\lambda} \times \vec{B}_0(\vec{x}) \left[ \frac{1}{\lambda^3} + \frac{i\omega}{\lambda^2} \right] \frac{e^{-i\omega\lambda} e^{ik_a|\vec{x}-\vec{y}|}}{|\vec{x}-\vec{y}|} \left( \vec{E} \cdot \vec{B} \right)_\omega \right\}. \quad (\text{A.1})$$

Here the integration  $\vec{y}$  is taken over the volume of the production cavity,  $\vec{x}$  is over the volume of the conversion region, and  $\vec{\lambda} = (\vec{r} - \vec{x})$  is the separation vector between points in the toroid and a detection point  $\vec{r}$ . The time-dependent  $J_{\text{eff}}$  has been evaluated at the retarded time  $t_r = t - \lambda$ . (A.1) also uses the approximation that the axion-induced fields fully propagate outside of the toroid, as expected for quasistatic frequencies.  $B_a$  lies in the poloidal direction and has an amplitude:

$$\hat{z} \cdot \vec{B}_a = \frac{g^2 B_{\text{pc}}^2 B_0}{\omega^2} \beta(\vec{r}), \quad (\text{A.2})$$

where the dimensionless form factor  $\beta$  contains information about the choice of cavity modes, etc.

First we specify the dimensions involved. Consider a circular cylindrical cavity (“pill-box”) of radius  $a$  and height  $h$ . The resonant frequencies are

$$\omega_{npq}^{\text{TM}} = \sqrt{\left(\frac{x_{np}}{a}\right)^2 + \left(\frac{q\pi}{h}\right)^2}, \quad \omega_{npq}^{\text{TE}} = \sqrt{\left(\frac{x'_{np}}{a}\right)^2 + \left(\frac{q\pi}{h}\right)^2}, \quad (\text{A.3})$$

for  $\text{TM}_{npq}$  and  $\text{TE}_{npq}$  modes respectively, where  $x_{np}$  and  $x'_{np}$  are the  $p$ th roots of the  $n$ th order Bessel function  $J_n(x)$  and its derivative  $J'_n(x)$  [199]. Setting  $a = h/2 = 10$  cm ensures resonant frequencies of order  $\approx$  GHz for low-lying modes, typical of SRF cavities.

Next consider a toroid of inner radius  $R$  and rectangular cross section of height and width  $R$ . We take the cylindrical cavity to be aligned axially with the toroid, with a minimal

separation distance of  $(h + R)/2$ . Though this should be gapped toroid, we can approximate the static field contained inside the toroidal volume as

$$\vec{B}_0(r) = B_0 \left( \frac{R}{r} \right) \hat{\phi}, \quad (\text{A.4})$$

for  $r \in [R, 2R]$  where  $r$  is the cylindrical radial distance from the center. If we require the toroid size saturates the quasistatic limit  $R\omega \sim 1$ , an economical choice for the dimension is simply  $R = a$ .

We now consider the axion source in this setup. The source axion field is greatest when  $\vec{E} \cdot \vec{B}$  is maximal and coherent throughout the production cavity volume. Since we have assumed a cylindrical cavity with no external field, it is necessary to drive multiple modes to ensure a non-vanishing  $(\vec{E} \cdot \vec{B})_\omega$ . The choice of these modes is not obvious and requires care even in this simple setup.

To demonstrate an ill-advised choice consider the  $\text{TM}_{010}$  and  $\text{TM}_{111}$  modes which results in  $(\vec{E} \cdot \vec{B})_\omega \propto \sin(\pi z/h) \sin(\phi)$ . Note that the integral of  $(\vec{E} \cdot \vec{B})_\omega$  vanishes over  $z \in [-h/2, h/2]$  of the production cavity. This  $z$ -dependence is in fact a general feature of any cylindrical cavity modes chosen, but it is not detrimental as we are operating in the near-field regime. Rather,  $\text{TM}_{010}$  and  $\text{TM}_{111}$  represents a poor choice of modes because of the  $\phi$  dependence—the sourced axion field will be purely harmonic in the azimuthal angle, and thus would integrate over the toroid to give a highly suppressed signal field near the center. This cancellation is essentially a consequence of the symmetry and alignment of the cylindrical setup and is easily avoidable. One potential solution is to place the production cavity in a position off the axial axis. Another is to modify the toroid wiring so  $\vec{B}_0$  also varies with the azimuthal angle while still being effectively confined. One can also select cavity modes such that  $(\vec{E} \cdot \vec{B})_\omega$  is not purely harmonic in  $\phi$ : the lowest-lying combination of cylindrical modes which yields this angular behavior is the  $\text{TM}_{111}$  and  $\text{TE}_{111}$  modes.

In any case, we can estimate a reasonable upper limit to  $\beta$  in (A.2) by postulating a perfectly *uniform*  $\vec{E} \cdot \vec{B}$  throughout the production cavity volume. Taking this optimal axion source, we numerically find that  $\beta$  is roughly constant for points in the center of the toroid:

$$\beta_{\text{optimal}} \approx 7 \cdot 10^{-2}, \quad z = 0 \text{ and } r \leq R. \quad (\text{A.5})$$

Here we have also taken the limit in which the mass is negligible,  $m_a \ll \omega$ . At masses  $m_a \gtrsim \omega$ , there is the usual exponential drop-off from producing off-shell axions. If we instead use a perhaps more realistic axion source by driving the  $\text{TM}_{111}$  and  $\text{TE}_{111}$  combination, we numerically find that  $\beta_{\text{realistic}} \approx 4 \cdot 10^{-4}$ , again roughly constant near the center of the toroid.

In summary, we expect the form factor  $\beta$  can in principle be made  $\mathcal{O}(0.1)$  in any suitably engineered designs. As discussed, it is important to determine a suitable geometry and choice of modes to be driven in the SRF production cavity, as a poor choice could lead to a significant suppression of the signal fields.

## Appendix B

### A Toy Model for Screening

We ultimately rely on the quasistatic approximation in assuming the axion-induced fields propagate  $\mathcal{O}(1)$  out of the gapped toroid, similar to [32]. This limits the size of the toroid to be less than or of order the inverse frequency of the axion. However it is important to understand the *degree* to which the fields outside the toroid are suppressed at larger frequencies or larger toroid size. This is a complicated boundary-value problem and a full study would require a detailed numerical computation which is outside the scope of this work. We will demonstrate here the power-law nature of this suppression.

To gain some intuition, consider an electromagnetic field of frequency  $\omega$  impinging on a perfect conducting sheet. If the conductor is infinitely large, then the incoming field is reflected and vanishes on the far side of the conductor (i.e., metals are shiny). An analogous behavior holds for fields sourced inside of a region bounded by a closed conducting surface—the field is exactly screened outside (i.e., phones do not work in elevators). The common feature is that the conductors lack a boundary. We thus expect incident fields to be suppressed, but not exactly screened, outside of a large yet finite conductor with a definite boundary. This will occur when the conductor size  $H$  is much larger than the wavelength  $\omega^{-1}$ .

Now suppose the conductor is small relative to  $\omega^{-1}$ . This is just the quasistatic limit, so we may assess the conductor's response by considering its response to a static field. In this familiar situation, the field will induce charges and currents on the surface of the conductor in order to screen the bulk. It is clear that the boundaries play an important role in this limit. For example, a conducting block in a static electric field will develop a screening charge density on the boundary, which modifies the net external field but does not result in a parametrically small external field. For  $\omega H \ll 1$  we therefore expect the field on the far side of the conductor to only differ from the incident field by  $\mathcal{O}(1)$  factors.

We study here a toy model of electromagnetic fields incident on a finite cylindrical conductor. The parametric effects of screening can be sensibly extracted in the high-frequency limit, and we find the magnitude of external, detected fields are only power-law suppressed compared to the internal fields. The physical mechanism underlying this suppression, as summarized in Sec. 2.3, is expected to hold generically in varied geometries.

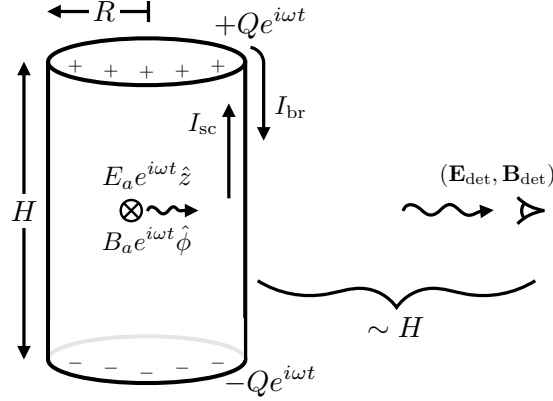


Figure B.1: Screening of EM fields  $(\vec{E}_a, \vec{B}_a)$  sourced inside a finite cylindrical wall. In the high-frequency limit, the conductor response results in charge buildup  $Q$  on the edges and a configuration of screening currents  $I_{sc}$ ,  $I_{br}$  on the inner and outer surfaces. These in turn determine the fields  $(\vec{E}_{det}, \vec{B}_{det})$  detected outside the cylinder.

Consider a perfectly conducting cylinder of height  $H$  and radius  $R$ . More precisely, take this to be a tube of negligible thickness separating an inner and outer cylindrical wall. Suppose there is an EM field  $(\vec{E}_a, \vec{B}_a) = (E_a \hat{z}, B_a \hat{\phi})$ , sourced by an infinite line of current  $I_a e^{i\omega t} \hat{z}$  “in the throat” of the cylinder. This is labelled suggestively in analogy to fields sourced by the axion interaction with a static magnetic field, although for simplicity we assume a spatially uniform  $I_a$ . We specifically examine the limit of a thin cylinder and take  $R \sim \omega^{-1} \ll H$ , which is of course well beyond the quasistatic approximation. Here the fields radiated by  $I_a$  are cylindrical plane waves, with approximate magnitudes:

$$E_a(r) \sim B_a(r) \sim \omega I_a e^{i\omega t} \left( \frac{1}{\omega r} \right)^{1/2}, \quad R \lesssim r \lesssim H. \quad (\text{B.1})$$

These source fields will be compared to the detected fields  $(\vec{E}_{det}, \vec{B}_{det})$  at a point  $r \sim H$  outside the cylinder. This is depicted in Fig. B.1. From here on, we restrict our attention to the behavior of fields in the region  $R \lesssim r \lesssim H$ , extending from the cylindrical surface to the detection point. We will also ignore any contributions to the fields due to the source wire  $I_a$  “sticking out” the ends, since this finite cylinder is intended to resemble an “unwrapped” version of our gapped toroid.

To determine the detected fields, the conductor response is paramount. Boundary conditions dictate that the electric and magnetic fields vanish in the thickness of the cylinder, and the  $z$ -component of the electric field vanishes on the surface. Importantly, for a finite cylinder the inner and outer surfaces are connected, so that the current established on the inner wall is communicated in some form to the outer wall. This communication, and the de-

tected fields that result, can be estimated by approximately satisfying boundary conditions as follows:

Firstly,  $I_a$  drives a screening current  $I_{sc}$  on the inner walls in order to cancel the source fields. By continuity, there is then necessarily a charge buildup  $\pm Qe^{i\omega t}$  at the top and bottom edges of the cylinder, respectively. We will not attempt to explicitly satisfy boundary conditions near these edges (which involves complicated fringe effects). Instead, we will consider the effects of this charge on the rest of the cylinder at locations far from the edges—that is,  $H/2 - |z| \gg R$ , where  $z = 0$  corresponds to the vertical center of the cylinder. Here the oscillating rings of charge at  $z = \pm H/2$  appear as points and produce an electric field on the cylinder surface:

$$\hat{z} \cdot \vec{E}_Q(R, z) \sim Qe^{i\omega t} \left( \frac{e^{-i\omega z_+}(1 + i\omega z_+)}{z_+^2} + \frac{e^{-i\omega z_-}(1 + i\omega z_-)}{z_-^2} \right), \quad (\text{B.2})$$

where  $z_{\pm} = H/2 \pm z$ . Up to a phase, this is approximately

$$\hat{z} \cdot \vec{E}_Q(R, z) \sim \frac{\omega Q e^{i\omega t}}{H/2 - |z|} \cos(\omega z). \quad (\text{B.3})$$

To continue satisfying boundary conditions, this field must now be canceled. Therefore, a “back-reaction” current  $I_{br}$  must be set up on the cylinder walls, chosen to cancel  $\vec{E}_Q$ . Numerically, we find that a current of the form  $I_{br}(z) \sim I_{br} \cos(\omega z)$  sources electric fields with the necessary sinusoidal behavior:

$$\hat{z} \cdot \vec{E}_{br}(R, z) \sim \frac{I_{br} e^{i\omega t}}{H/2 - |z|} \cos(\omega z). \quad (\text{B.4})$$

We can ensure that this back-reaction does not also violate the previously satisfied boundary conditions by taking  $I_{br}$  to flow in the same direction on both inner and outer walls. It is notable that near the center of the cylinder, (B.4) vanishes as the height increases  $H \rightarrow \infty$ . Such a scaling can be understood by considering a  $\cos(\omega z)$  current on the surface of an *infinitely* tall cylinder. In that case, the  $z$ -component of the electric field exactly vanishes as there is a cancellation between the field sourced by the current and the field sourced by stripes of charge which are present due to charge continuity. This cancellation is weaker near the edges of a finite cylinder, leading to larger  $\hat{z} \cdot \vec{E}_{br}$  there.

The above charges/currents must be self-consistent. The initial screening current  $I_{sc}$  on the inner wall, charge buildup  $Q$  on the edges, and back-reaction currents  $I_{br}$  on both walls here are related by charge continuity:

$$\frac{dQ}{dt} = i\omega Q \sim I_{sc} - 2I_{br}, \quad (\text{B.5})$$

where the factor of 2 accounts for the fact that  $I_{br}$  flows in the same direction on both walls. Since the cylinder is tall and thin, we can invoke the infinite-cylinder solution to



approximately cancel the source fields, and thus we take  $I_{\text{sc}} \sim I_a$  on the inner surface. Comparing (B.3) and (B.4), to cancel the fields produced by the charge buildup requires back-reaction currents of order  $I_{\text{br}} \sim \omega Q$ . These currents, taken together, then approximately satisfy boundary conditions everywhere away from the edges. Now further demanding the constraint of continuity (B.5), we find the charge buildup should be  $Q \sim I_a/\omega$ , and therefore the back-reaction currents are of order  $I_{\text{br}} \sim I_a \cos(\omega z)$ . The  $z$ -component of the back-reaction field is parametrically smaller than the source field (B.1) on the surface:

$$\frac{\hat{z} \cdot \vec{E}_{\text{br}}(R, z)}{E_a(R, z)} \sim (\omega H)^{-1} \ll 1. \quad (\text{B.6})$$

This is consistent with our use of the infinite-cylinder solution for the inner screening current  $I_{\text{sc}} \sim I_a$ .

To summarize, we have found there are additional currents  $I_{\text{br}} \sim I_a \cos(\omega z)$  on the inner and outer cylinder surfaces, arising from the need to satisfy boundary conditions in the presence of charge build-up. These are inevitably of the same order as the source current, but with a crucial spatial modulation. Based on these currents, we estimate the detected fields at a point  $r \gtrsim H$  (and near  $z \sim 0$ ) outside the cylinder:

$$\begin{aligned} \vec{E}_{\text{det}}(r, z) &\sim I_a \cos(\omega z) e^{i\omega t} \left( \frac{1}{r} \hat{r} + \frac{1}{H+r} \hat{z} \right), \\ \vec{B}_{\text{det}}(r, z) &\sim \frac{I_a}{r} \cos(\omega z) e^{i\omega t} \hat{\phi}. \end{aligned} \quad (\text{B.7})$$

The fields radiated by the oscillating charges on the cylinder edges are of this same magnitude.

The charge buildup and back-reaction currents thus propagate fields outside the cylinder. Importantly, the magnitudes of these fields (B.7) fall off as  $r^{-1}$ , faster than the  $r^{-1/2}$  behavior of the source fields (B.1) that would be seen if the conductor were not present. Comparing these, we see the magnitude of the external, detected field is power-law suppressed:

$$B_{\text{det}}/B_a \sim (\omega H)^{-1/2} \ll 1. \quad (\text{B.8})$$

This is fundamentally because the fields radiated by a modulated, multipolar current decay more rapidly than the fields from a spatially uniform current.

Lastly, we briefly comment on the low-frequency behavior of our toy model. The spatially modulated current distribution we had found on the surface is a consequence of modulated fields from non-negligible charge buildup—this feature, however, is only present at sufficiently high frequencies. In the opposite limit  $R, H \ll \omega^{-1}$ , the analogous secondary fields from charge buildup are uniform across the cylinder surface and drive an unmodulated current that results in equal and opposite currents flowing on the inner and outer surfaces. This is the familiar quasistatic result in which no screening occurs and a uniform current loop is established, as in the operation of a cryogenic current comparator [200].

# Appendix C

## Dark Higgs Thermalization

In this section we further examine vector production by PR for the case  $\lambda \gg e$  requiring that the vector constitutes all of the DM today. In Sec. 3.4, we explored the parameter space in this scenario assuming that the large initial yield of dark Higgs after PR thermalizes with the SM. Here, we explicitly study the case of thermalization through a Higgs-portal coupling,

$$\mathcal{L} \supset y^2 |\varphi|^2 |H|^2, \quad (\text{C.1})$$

where  $H$  is the SM Higgs doublet. After electroweak symmetry breaking, there is a mixing between the two real scalars with an angle,

$$\tan 2\theta \sim y^2 \frac{2vv_{\text{EW}}}{m_h^2 - m_\phi^2}, \quad (\text{C.2})$$

where  $v_{\text{EW}} \sim 246$  GeV. For simplicity, we will consider the regime  $m_\phi \ll m_h$  so that  $\theta \sim y^2 v / v_{\text{EW}}$ . This interaction must satisfy a number of conditions in order for the cosmology to be viable, namely:

1. The thermalization occurs sufficiently rapidly,
2. The dynamics of PR is largely unaffected,
3. The coupling is not ruled out by experiments.

Our aim here is to show the existence of a viable parameter region in dark Higgs mass and coupling for which all conditions can be consistently satisfied.

We first address the requirements on thermalizing the dark Higgs. The relevant processes differ if thermalization occurs before or after the electroweak phase transition which depletes the SM Higgs. Above this scale the dominant number-density depleting process that brings the dark Higgs into chemical equilibrium is through a Higgs absorption  $\phi H \rightarrow H$ . Proper calculation of this rate requires non-equilibrium field theory techniques. The thermalization rate is roughly of order [201]  $\Gamma_{\phi H \rightarrow H} \sim y^4 v^2 / T$ . From this we estimate the temperature of dark Higgs thermalization  $T_{\text{th}} \sim (y^4 v^2 M_{\text{pl}})^{1/3}$ . Requiring this thermalization temperature

to be above  $\sim 100$  GeV puts a constraint on the mixing angle,  $\theta \gtrsim 10^{-7}$ . Below the electroweak scale,  $\phi$  will continue to interact with SM fermions in the thermal bath. For instance, thermal  $\phi$  particles can scatter off fermions (e.g. quarks) in the plasma with a rate [201],  $\Gamma_{\phi q \rightarrow qg} \sim \theta^2 y_f^2 T$ , where  $y_f$  is the largest fermion Yukawa coupling still in the SM bath. For this to be above the mass of the fermion requires  $\theta \gtrsim 10^{-8}/\sqrt{y_f}$ . This ensures  $\phi$  has a thermal abundance and thus dumps its energy to the SM bath when  $T \lesssim m_\phi$ . If, e.g.,  $m_\phi = 10$  GeV, this process is in thermal equilibrium with bottom quarks by the time the temperature drops to  $T \sim m_b$  as long as  $\theta \gtrsim 10^{-7}$ .

Next we consider the implications the Higgs portal coupling on the PR mechanism. As long as the coupling is not fine-tuned  $\theta < m_\phi/m_h$ , the SM Higgs mass correction at the time of PR is less than the expected thermal mass. Therefore, the Higgs portal coupling gives a mass correction  $\delta m_\phi^2 \sim y^2 T_{\text{osc}}^2$  to the dark Higgs at the onset of oscillations. If this is larger than the assumed effective mass-squared  $m_{\text{eff}}^2 \sim \lambda^2 \phi_0^2$ , the dark Higgs would have oscillated earlier with a large frequency (set by the size of  $y^2$ ), thus rendering the PR production of vector modes narrow and relatively inefficient. Requiring this thermal contribution to be sufficiently small  $\delta m_\phi^2 \lesssim \lambda^2 \phi_0^2$  translates into an upper bound on the mixing angle,

$$\theta \lesssim 10^{-2} \left( \frac{m_\phi}{\text{GeV}} \right) \left( \frac{\phi_0}{10^{-1} M_{\text{pl}}} \right) \quad (\text{C.3})$$

For Fig. 3.2 where we fix  $m_\phi \sim 10$  GeV, this is the dominant upper bound on the mixing angle.

A second possible effect of the Higgs portal coupling is PR production of the SM Higgs. For thermalization we generically require  $y \gg \lambda$  which would suggest that PR may be efficient in producing the SM Higgs; this is ultimately not the case due to the large thermal mass of the Higgs. We can verify this by computing the adiabatic parameter  $R = |\dot{\omega}|/\omega^2$  for the SM Higgs with a time-dependent frequency  $\omega(t) \sim \sqrt{k^2 + m_H(T)^2 + \frac{1}{2}y^2\phi(t)^2}$ . Since the thermal mass is strictly larger than the mass contribution from the oscillating field at the time of PR ( $y^2\phi_0^2 \ll T_{\text{osc}}^2$ ), the adiabatic parameter is always less than unity. We conclude that there is no significant non-perturbative production of the SM Higgs.

There are a number of phenomenological constraints on a Higgs-portal scalar. These constraints depend on whether the scalar decays visibly or appears invisible (at least on detector scales.) For detailed review see, e.g., [202]. For low masses  $m_\phi \lesssim \text{MeV}$ , we find stellar cooling constraints [203] are in tension with the requirements of thermalization. For intermediate masses,  $\text{MeV} \lesssim m_\phi \lesssim 300$  MeV constraints from Supernova 1987A and rare Kaon decays are powerful, but it may be possible to have a scalar in this mass range with a sufficiently large  $\theta$  consistent with thermalization if it sits in the small gap between these constraints. For masses  $\text{GeV} \lesssim m_\phi \lesssim 5$  GeV, rare B meson decays roughly constrain  $\theta \lesssim 10^{-3}$ . Above this scale, scalar production at LEP constrains  $\theta \lesssim 10^{-1}$  although this is weaker than the condition (C.3). Interestingly, if  $\phi$  decays visibly then lower values of  $\theta$  in this mass range could also be probed by future experiments designed to look for long-lived particles [204, 205, 206, 207, 208].

Lastly one may wonder if the dark Higgs ever dominates the energy density of the universe. Dark Higgs domination will take place if the temperature of thermalization is less than  $\lesssim T_{\text{eq}}(m_\phi/m_X)$ , or in terms of the mixing angle:

$$\theta \lesssim \left( \frac{T_{\text{eq}}^3}{v_{\text{EW}}^2 M_{\text{pl}}} \right)^{1/2} \left( \frac{m_\phi}{m_X} \right)^{3/2} \sim 5 \cdot 10^{-6} \left( \frac{m_\phi}{\text{GeV}} \right)^{3/2} \left( \frac{10^{-4} \text{ eV}}{m_X} \right)^{3/2}. \quad (\text{C.4})$$

We see that for  $m_\phi \sim 10 \text{ GeV}$  and the relevant vector mass range  $m_X \gtrsim 10^{-4}$  in Fig. 3.2, this is never the case as long as we satisfy the condition of thermalization.

# Appendix D

## Particle Stopping in a White Dwarf

Here we provide a more detailed analysis of the stopping power (energy loss per distance traveled) of high-energy SM particles in a carbon-oxygen WD due to strong and electromagnetic interactions. We consider incident electrons, photons, pions, and nucleons with kinetic energy greater than an MeV.

### D.1 WD Medium

For the WD masses that we consider, the stellar medium consists of electrons and fully-ionized carbon nuclei with central number densities in the range  $n_e = Zn_{\text{ion}} \sim 10^{31} - 10^{33} \text{ cm}^{-3}$  where  $Z = 6$ . The internal temperature is  $T \sim \text{keV}$  [125]. The electrons are a degenerate and predominantly relativistic free gas, with Fermi energy

$$E_F = (3\pi^2 n_e)^{1/3} \sim 1 - 10 \text{ MeV}. \quad (\text{D.1})$$

The carbon ions, however, are non-degenerate and do not form a free gas. The plasma frequency due to ion-ion Coulomb interactions is given by

$$\Omega_p = \left( \frac{4\pi n_{\text{ion}} Z^2 \alpha}{m_{\text{ion}}} \right)^{1/2} \sim 1 - 10 \text{ keV}, \quad (\text{D.2})$$

where  $m_{\text{ion}}$  is the ion mass. Finally, the medium also contains thermal photons, though these are never significant for stopping particles as the photon number density  $n_\gamma \sim T^3$  is much smaller than that of electrons or ions.

### D.2 Nuclear Interactions

**Elastic Scattering of Hadrons.** Hadrons with energy less than the nuclear binding energy  $E_{\text{nuc}} \sim 10 \text{ MeV}$  will predominantly stop due to elastic nuclear scatters with ions. These

are hard scatters, resulting in a stopping power

$$\frac{dE}{dx} \sim n_{\text{ion}} \sigma_{\text{el}} \left( \frac{m}{m_{\text{ion}}} \right) E \quad (\text{D.3})$$

for a hadron of mass  $m \ll m_{\text{ion}}$  and kinetic energy  $E$ .  $\sigma_{\text{el}}$  is the elastic nuclear scattering cross section, which is of order  $\sigma_{\text{el}} \approx \text{b}$  at these energies and drops to  $\sigma_{\text{el}} \approx 0.1 \text{ b}$  above 10 MeV [209], ignoring the nontrivial effect of nuclear resonances in the intermediate regime 1 – 10 MeV.

**Inelastic Scattering of Hadrons.** For energies above  $E_{\text{nuc}}$ , the stopping of hadrons is dominated by inelastic nuclear scatters. In such a collision, an incoming hadron interacts with one or more nucleons to produce a  $\mathcal{O}(1)$  number of additional hadrons which approximately split the initial energy. At incident energy greater than  $\sim \text{GeV}$ , the majority of secondary hadrons are pions with transverse momenta  $\sim 100 \text{ MeV}$  [209]. Below  $\sim \text{GeV}$ , it is found that roughly equal fractions of protons, neutrons, and pions are produced in each collision [210]. We will thus have a roughly collinear shower terminating at an energy  $\sim 10 \text{ MeV}$  which consists of pions for most of the shower's development and converts to a mix of pions and nucleons in the final decade of energy. This cascade is described by a radiative stopping power

$$\frac{dE}{dx} \sim n_{\text{ion}} \sigma_{\text{inel}} E, \quad (\text{D.4})$$

where the inelastic nuclear cross section is given by  $\sigma_{\text{inel}} \approx 100 \text{ mb}$  and roughly constant in energy [209]. The total length of the shower is only logarithmically dependent on the initial hadron energy  $E$ ,

$$X_{\text{had}} \sim \frac{1}{n_{\text{ion}} \sigma_{\text{inel}}} \log \left( \frac{E}{E_{\text{nuc}}} \right). \quad (\text{D.5})$$

**Photonuclear Interactions.** Photons of energy greater than 10 MeV can also strongly interact with nuclei through the production of virtual quark-antiquark pairs. This is the dominant mode of photon energy loss at high energy. The photonuclear scatter destroys the photon and fragments the nucleus, producing secondary hadrons in a shower analogous to that described above. The photonuclear cross section  $\sigma_{\gamma A}$  is roughly given by  $\sigma_{\gamma A} \approx \alpha \sigma_{\text{inel}}$ , again ignoring the nuclear resonances that occur for  $E \lesssim \text{GeV}$  [209]. For  $E \gtrsim \text{GeV}$ ,  $\sigma_{\gamma A}$  is likely a slowly increasing function of energy due to the coherent interaction of the photon over multiple nucleons [211], however, instead of extrapolating this behavior we conservatively take a constant photonuclear cross section  $\sigma_{\gamma A} \approx 1 \text{ mb}$ .

**Electronuclear Interactions.** Electrons can similarly lose energy to nuclei by radiating a virtual photon that undergoes a photonuclear scatter, which indeed provides the dominant energy loss for high energy electrons. The cross section for this process is roughly given by

the photonuclear cross section, scaled by a factor representing the probability to radiate such a photon. This can be estimated with the Weizsacker-Williams approximation, which gives a stopping power that is suppressed from the photonuclear result by  $\alpha$  but enhanced by an  $\mathcal{O}(10)$  logarithmic phase space factor [211]:

$$\frac{dE}{dx} \sim \alpha n_{\text{ion}} \sigma_{\gamma A} E \log \left( \frac{E}{m_e} \right). \quad (\text{D.6})$$

Unlike the photonuclear interaction, the electronuclear event is a radiative process that preserves the original electron while leaving hadronic showers in its wake.

### D.3 Radiative Processes

Electromagnetic showers due to successive bremsstrahlung and pair production events off carbon ions are the dominant stopping mechanisms for intermediate-energy electrons and photons. Both of these processes result in radiative stopping powers, derived semi-classically as [212]

$$\frac{dE}{dx} \sim \frac{E}{X_0}, \quad X_0^{-1} = 4n_{\text{ion}} Z^2 \frac{\alpha^3}{m_e^2} \log \Lambda. \quad (\text{D.7})$$

$X_0$  is the well-known radiation length, and  $\log \Lambda$  is a Coulomb form factor given by the range of effective impact parameters  $b$ :

$$\Lambda = \frac{b_{\text{max}}}{b_{\text{min}}}. \quad (\text{D.8})$$

The maximal impact parameter is set by the plasma screening length (see D.4) and the minimum by the electron mass, below which the semi-classical description breaks down. Note that for the highest WD densities  $\Lambda \lesssim 1$ , in which case (D.7) ought to be replaced by a fully quantum mechanical result as in [213]. This still results in a radiative stopping power, and so for simplicity we employ (D.7) with  $\log \Lambda \sim \mathcal{O}(1)$  for all WD densities.

**LPM Suppression** A radiative event involving momentum transfer  $q$  to an ion must, quantum mechanically, occur over a length  $\sim q^{-1}$ . All ions within this region contribute to the scattering of the incident particle, and for sufficiently small  $q$  this results in a decoherence that suppresses the formation of photons or electron-positron pairs. This is the “Landau-Pomeranchuk-Midgal” (LPM) effect. The momentum transfer  $q$  in a given event decreases with increasing incident particle energy, and so the LPM effect will suppress radiative processes for energies greater than some scale  $E_{\text{LPM}}$ . This can be calculated semi-classically [212],

$$E_{\text{LPM}} = \frac{m_e^2 X_0 \alpha}{4\pi} \approx 1 \text{ MeV} \left( \frac{10^{32} \text{ cm}^{-3}}{n_{\text{ion}}} \right). \quad (\text{D.9})$$

which is quite small due to the high ion density in the WD. The stopping power for bremsstrahlung and pair production in the regime of LPM suppression  $E > E_{\text{LPM}}$  is

$$\frac{dE}{dx} \sim \frac{E}{X_0} \left( \frac{E_{\text{LPM}}}{E} \right)^{1/2} \quad E > E_{\text{LPM}}. \quad (\text{D.10})$$

In addition to the LPM effect, soft bremsstrahlung may be suppressed in a medium as the emitted photon acquires an effective mass of order the plasma frequency  $\Omega_p$ . However, for high-energy electrons this dielectric suppression only introduces a minor correction to (D.10), in which soft radiation is already suppressed [212].

## D.4 Elastic EM Scattering

**Electron Coulomb Scattering off Ions.** Coulomb collisions with ions are the mechanism by which electrons of energy 1 – 10 MeV ultimately thermalize ions. In this scenario we may treat the ions as stationary and ignore their recoil during collisions. The nuclear charge will be screened by the mobile electrons of the medium, so incident particles scatter via a potential

$$V(\mathbf{r}) = \frac{Z\alpha}{r} e^{-r/\lambda_{\text{TF}}}. \quad (\text{D.11})$$

The screening length  $\lambda_{\text{TF}}$  is given in the Thomas-Fermi approximation by [190]:

$$\lambda_{\text{TF}}^2 = \frac{E_F}{6\pi\alpha n_e} \sim \frac{1}{\alpha E_F^2}. \quad (\text{D.12})$$

This plasma screening suppresses scatters with momentum transfers below  $\sim \lambda_{\text{TF}}^{-1}$ , corresponding to a minimal energy transfer of  $\omega_{\text{min}} = \lambda_{\text{TF}}^{-2}/2m_{\text{ion}}$ . Ions may in principle also cause screening through lattice distortion, however this may be ignored as the sound speed of the lattice  $c_s \sim 10^{-2}$  is much smaller than the speed of an incident relativistic electron. From the Born approximation, the cross section for energy transfer  $\omega$  is

$$\frac{d\sigma}{d\omega} = \frac{2\pi Z^2 \alpha^2}{m_{\text{ion}} v_{\text{in}}^2} \frac{1}{(\omega + \omega_{\text{min}})^2}, \quad (\text{D.13})$$

where  $v_{\text{in}}$  is the incident velocity. Thus the stopping power is

$$\frac{dE}{dx} = \int_0^{\omega_{\text{max}}} d\omega n_{\text{ion}} \frac{d\sigma}{d\omega} \omega \approx \frac{2\pi n_{\text{ion}} Z^2 \alpha^2}{m_{\text{ion}} v_{\text{in}}^2} \log \left( \frac{\omega_{\text{max}}}{\omega_{\text{min}}} \right), \quad (\text{D.14})$$

where the second line is valid if  $\omega_{\text{max}} \gg \omega_{\text{min}}$ .  $\omega_{\text{max}}$  is the maximum possible energy transfer. This may be due to 4-momentum conservation, or in the case of incident electrons, the



impossibility of scattering to a final energy less than  $E_F$ . 4-momentum conservation sets an upper bound  $\omega_{\text{kin}}$ , which for a stationary target is

$$\omega_{\text{kin}} = \frac{2m_{\text{ion}}p^2}{m_{\text{ion}}^2 + m^2 + 2Em_{\text{ion}}}, \quad (\text{D.15})$$

with  $p$ ,  $E$  the incoming momentum and energy. The Fermi upper bound is  $\omega_F = E - E_F$  so for incident electrons we take  $\omega_{\text{max}} = \min\{\omega_{\text{kin}}, \omega_F\}$ .

For scatters that transfer energy less than the plasma frequency  $\Omega_p$ , one may be concerned about phonon excitations. This occurs for incident electrons with energy below  $\sim 10$  MeV. We estimate this stopping power treating each ion as an independent oscillator with frequency  $\Omega_p$  (an Einstein solid approximation) and compute the stopping power due to scatters which excite a single oscillator quanta. There are two key differences between this and the free ion case: incident particles must transfer an energy  $\Omega_p$ , and the cross section to transfer momentum  $q$  is suppressed by a factor  $q^2/2m_{\text{ion}}\Omega_p = \omega_{\text{free}}/\Omega_p$ .  $\omega_{\text{free}}$  is the energy transfer that would accompany a free ion scatter with momentum transfer  $q$ . The resulting stopping power is unchanged from the free case (D.14), as the increased energy transfer compensates for the suppressed cross section.

As electrons transfer their energy at the rate (D.14), they occasionally experience a hard scatter with mean free path

$$\lambda_{\text{hard}} \approx \frac{p^2 v_{\text{in}}^2}{\pi n_{\text{ion}} Z^2 \alpha^2}. \quad (\text{D.16})$$

For sufficiently small incident energies, the electron experiences several hard scatters before it has deposited its energy by elastic scatters, and the stopping length is reduced by the resulting random walk. This effect is not significant for incident pions due to their larger mass.

Finally, we note that for highly energetic incident particles the cross section (D.13) should be modified to account for the recoil of the ion. However, at such energies the dominant stopping power will be from hadronic or electromagnetic showers anyway, so we do not include these recoil effects.

**Relativistic Coulomb Scattering off Electrons.** The scattering of incident electrons off degenerate electrons determines the termination energy of electromagnetic showers. This calculation demands two considerations not present when scattering off ions: the targets are not stationary and they require a threshold energy transfer in order to be scattered out of the Fermi sea. However for relativistic incident particle, with momentum  $p \gg p_F$ , the stopping power off electrons is ultimately of the same form as the stopping power off ions (D.14). In this limit, all particle velocities and the relative velocity is  $\mathcal{O}(1)$ , and the deflection of the incident particle will generally be small. It is reasonable then that scattering proceeds, up to  $\mathcal{O}(1)$  factors, as though a heavy incident particle is striking a light, stationary target. The

cross section is given by the usual result,

$$\frac{d\sigma}{d\omega} \approx \frac{2\pi\alpha^2}{E_F} \frac{1}{\omega^2}, \quad (\text{D.17})$$

where we have accounted for the target's motion by replacing its mass with its relativistic inertia  $\approx E_F$ . This is equivalent to a boost of the cross section from the rest frame of the target into the WD frame. Note that plasma screening can be ignored in this case, as Pauli-blocking will provide a more stringent cutoff on soft scatters. Scatters which transfer an energy  $\omega \leq E_F$  will have a suppressed contribution to the stopping power as they can only access a fraction of the Fermi sea. In this limit it is sufficient to ignore these suppressed scatters:

$$\frac{dE}{dx} = \int_{E_F}^{\omega_{\max}} d\omega n_e \frac{d\sigma}{d\omega} \omega \approx \frac{2\pi n_e \alpha^2}{E_F} \log \left( \frac{\omega_{\max}}{E_F} \right) \quad (\text{D.18})$$

where, as described above,  $\omega_{\max} = \min\{\omega_{\text{kin}}, \omega_F\}$ . This derivation is admittedly quite heuristic, and so it has been checked with a detailed numerical calculation accounting fully for the target's motion and degeneracy. Equation (D.18) is indeed a good approximation to the stopping power for incident energies larger than the Fermi energy.

**Non-Relativistic Coulomb Scattering off Electrons** For non-relativistic incident particles, the Coulomb stopping off electrons becomes strongly suppressed due to degeneracy. Stopping in this limit appears qualitatively different than in the typical case—the slow incident particle is now bombarded by relativistic electrons from all directions. Note that only those scatters which slow the incident particle are allowed by Pauli-blocking.

As the electron speeds are much faster than the incident, a WD electron with momentum  $p_F$  will scatter to leading order with only a change in direction, so the momentum transfer is  $|\vec{q}| \sim p_F$ . We again take the incident momentum  $p \gtrsim p_F$ , which is valid for all incident particles we consider. This results in an energy transfer

$$\omega = \left| \frac{p^2}{2m} - \frac{(\vec{p} - \vec{q})^2}{2m} \right| \sim v_{\text{in}} E_F. \quad (\text{D.19})$$

For  $v_{\text{in}} \ll 1$  the energy transfer is less than Fermi energy, so Pauli-blocking will be important. The incident particle is only be able to scatter from an effective electron number density

$$n_{\text{eff}} = \int_{E_F - \omega}^{E_F} g(E) dE \approx 3n_e \frac{\omega}{E_F}, \quad (\text{D.20})$$

where  $g(E)$  is the Fermi density of states. At leading order the electron is not aware of the small incident velocity, so the cross section is given by relativistic Coulomb scattering off a stationary target  $\sigma \sim \alpha^2/q^2$  [214]. The incident particle thus loses energy to degenerate electrons at a rate:

$$\frac{dE}{dt} \sim n_{\text{eff}} \sigma \omega \sim n_e \frac{\alpha^2}{E_F} v_{\text{in}}^2. \quad (\text{D.21})$$

Note that this includes a factor of the relative velocity which is  $\mathcal{O}(1)$ . As a result, the stopping power is parametrically

$$\frac{dE}{dx} = \frac{1}{v_{\text{in}}} \frac{dE}{dt} \sim n_e \frac{\alpha^2}{E_F} v_{\text{in}}. \quad (\text{D.22})$$

As above, this heuristic result has been verified with a full integration of the relativistic cross section.

We can compare (D.22) to the stopping power of non-relativistic, heavy particles off roughly stationary, non-degenerate electrons  $\frac{dE}{dx} \sim n_e \frac{\alpha^2}{m_e v_{\text{in}}^2}$ , which is the familiar setting of stopping charged particles in a solid due to ionization [215]. Evidently, the analogous stopping in a WD is parametrically suppressed by  $v_{\text{in}}^3 m_e / E_F$ . One factor of  $v_{\text{in}}$  is due to Pauli blocking, while the other factors are kinematic, due to the relativistic motion of the targets.

**Compton Scattering** Compton scattering off degenerate electrons is the dominant interaction for photons of incident energy  $k \leq E_F$ . As we will show, this stopping power is parametrically different from that of high-energy photons due to Pauli-blocking and the motion of the electron. For  $k > E_F$ , the effect of Pauli-blocking is negligible and the stopping power is simply:

$$\frac{dk}{dx} \sim \frac{\pi \alpha^2 n_e}{E_F} \log \left( \frac{k}{m_e} \right), \quad (\text{D.23})$$

where again we have (partially) applied the heuristic  $m_e \rightarrow E_F$  replacement to boost the usual result for stationary electrons while avoiding divergence at the Fermi energy. This, along with the low-energy estimate below, matches a full integration of the relativistic cross section well.

We now turn to the regime of interest,  $k < E_F$ . Only those electrons near the top of the Fermi sea are available to scatter, so the photon interacts with only the effective electron density (D.20). In addition, Compton scatters will only occur off electrons moving roughly collinear with the photon momentum - a head-on collision would result in an energy loss for the electron, which is forbidden by Pauli exclusion. In the electron rest frame these collinear scatters are Thompson-like, and the photon energy loss is dominated by backward scatters. For relativistic electrons near the Fermi surface, these scatters transfer an energy

$$\omega \sim k \left( 1 - \frac{m_e^2}{4E_F^2} \right) \approx k. \quad (\text{D.24})$$

The cross section can be taken in the electron rest frame  $\sigma \sim \alpha^2 / m_e^2$ , along with an ‘aiming’ factor  $1/4\pi$  to account for the restriction to initially parallel trajectories. This gives a stopping power

$$\frac{dk}{dx} \approx \frac{\alpha^2 n_e k^2}{4\pi m_e^2 E_F}. \quad (\text{D.25})$$

# Appendix E

## Dark Matter Capture

Here we give a more detailed discussion of DM capture in a WD and its subsequent evolution. For the remainder of this section all numerical quantities are evaluated at a central WD density  $\rho_{\text{WD}} \sim 3 \times 10^8 \frac{\text{g}}{\text{cm}^3}$  ( $n_{\text{ion}} \sim 10^{31} \text{ cm}^{-3}$ ), for which the relevant WD parameters are [120]:  $M_{\text{WD}} \approx 1.25 M_{\odot}$ ,  $R_{\text{WD}} \approx 4000 \text{ km}$ , and  $v_{\text{esc}} \approx 2 \times 10^{-2}$ . Depending on the context, the relevant density may be the average value which we take to be  $\sim 10^{30} \text{ cm}^{-3}$ . We also assume an average value of the WD temperature  $T_{\text{WD}} \sim \text{keV}$ .

### E.1 Capture Rate

Consider spin-independent DM elastic scattering off ions with cross section  $\sigma_{\chi A}$ . This is related to the per-nucleon cross section

$$\sigma_{\chi A} = A^2 \left( \frac{\mu_{\chi A}}{\mu_{\chi n}} \right)^2 F^2(q) \sigma_{\chi n} = A^4 F^2(q) \sigma_{\chi n}, \quad (\text{E.1})$$

where  $F^2(q)$  is the Helm form factor [179]. If the DM is at the WD escape velocity, the typical momentum transfer to ions is  $q \sim \mu_{\chi A} v_{\text{esc}} \sim 200 \text{ MeV}$ . As this  $q$  is less than or of order the inverse nuclear size, DM scattering off nuclei will be coherently enhanced. We find  $F^2(q) \approx 0.1$  for  $q \sim 200 \text{ MeV}$ .

For the DM to ultimately be captured, it must lose energy  $\sim m_{\chi} v^2$ , where  $v$  is the DM velocity (in the rest frame of the WD) asymptotically far away. Since typically  $v \ll v_{\text{esc}}$ , the DM has velocity  $v_{\text{esc}}$  while in the star and must lose a fraction  $(v/v_{\text{esc}})^2$  of its kinetic energy to become captured. Properly, the DM velocity is described by a boosted Maxwell distribution peaked at the galactic virial velocity  $v_{\text{halo}} \sim 10^{-3}$ . However, this differs from the ordinary Maxwell distribution by only  $\mathcal{O}(1)$  factors [124], and we can approximate it by (ignoring the exponential Boltzmann tail):

$$\frac{dn_{\chi}}{dv} \approx \begin{cases} \frac{\rho_{\chi}}{m_{\chi}} \left( \frac{v^2}{v_{\text{halo}}^3} \right) & v \leq v_{\text{halo}} \\ 0 & v > v_{\text{halo}} \end{cases}. \quad (\text{E.2})$$

The DM capture rate is given by an integral of the DM transit rate weighted by a probability for capture  $P_{\text{cap}}$

$$\Gamma_{\text{cap}} \sim \int dv \frac{d\Gamma_{\text{trans}}}{dv} P_{\text{cap}}(v), \quad (\text{E.3})$$

where the (differential) transit rate is

$$\frac{d\Gamma_{\text{trans}}}{dv} \sim \frac{dn_{\chi}}{dv} R_{\text{WD}}^2 \left( \frac{v_{\text{esc}}}{v} \right)^2 v. \quad (\text{E.4})$$

$P_{\text{cap}}$  depends on both the *average* number of scatters in a WD

$$\bar{N}_{\text{scat}} \sim n_{\text{ion}} \sigma_{\chi A} R_{\text{WD}}, \quad (\text{E.5})$$

and the number of scatters *needed* for capture

$$N_{\text{cap}} \sim \max \left\{ 1, \frac{m_{\chi} v^2}{m_{\text{ion}} v_{\text{esc}}^2} \right\}, \quad (\text{E.6})$$

and is most generally expressed as a Poisson sum

$$P_{\text{cap}} = 1 - \sum_{n=0}^{N_{\text{cap}}-1} \exp(-\bar{N}_{\text{scat}}) \frac{(\bar{N}_{\text{scat}})^n}{n!}. \quad (\text{E.7})$$

For our purposes we will approximate the sum as follows:

$$P_{\text{cap}} \approx \begin{cases} 1 & \bar{N}_{\text{scat}} > N_{\text{cap}} \\ \bar{N}_{\text{scat}} & \bar{N}_{\text{scat}} < N_{\text{cap}} \text{ and } N_{\text{cap}} = 1 \\ 0 & \text{else} \end{cases} \quad (\text{E.8})$$

Here we ignore the possibility of capture if  $\bar{N}_{\text{scat}} < N_{\text{cap}}$  except in the special case that only one scatter is needed for capture. If  $\bar{N}_{\text{scat}} > N_{\text{cap}}$ , we assume all DM is captured. Most accurately, this capture rate should be computed numerically, e.g. see [181]. However with the above simplifications we find that the capture rate is of order

$$\Gamma_{\text{cap}} \sim \Gamma_{\text{trans}} \cdot \min \left\{ 1, \bar{N}_{\text{scat}} \min \{ B, 1 \} \right\}, \quad B \equiv \frac{m_{\text{ion}} v_{\text{esc}}^2}{m_{\chi} v_{\text{halo}}^2}. \quad (\text{E.9})$$

$B$  here encodes the necessity of multiple scattering for capture. For ultra-heavy DM  $m_{\chi} > 10^{15}$  GeV,  $B \ll 1$  and essentially multiple scatters are always needed.

## E.2 Thermalization and Collapse

Once DM is captured, it thermalizes to an average velocity

$$v_{\text{th}} \sim \sqrt{\frac{T_{\text{WD}}}{m_\chi}} \approx 10^{-11} \left( \frac{m_\chi}{10^{16} \text{ GeV}} \right)^{-1/2}, \quad (\text{E.10})$$

and settles to the thermal radius

$$R_{\text{th}} \sim \left( \frac{T_{\text{WD}}}{G m_\chi \rho_{\text{WD}}} \right)^{1/2} \approx 0.1 \text{ cm} \left( \frac{m_\chi}{10^{16} \text{ GeV}} \right)^{-1/2},$$

where its kinetic energy balances against the gravitational potential energy of the (enclosed) WD mass. This thermalization time can be explicitly calculated for elastic nuclear scatters [156]. The stopping power due to such scatters is

$$\frac{dE}{dx} \sim \rho_{\text{WD}} \sigma_{\chi A} v \max\{v, v_{\text{ion}}\}, \quad (\text{E.11})$$

where  $v_{\text{ion}} \sim \sqrt{T_{\text{WD}}/m_{\text{ion}}}$  is the thermal ion velocity. The max function indicates the transition between “inertial” and “viscous” drag, as the DM velocity  $v$  slows to below  $v_{\text{ion}}$ . DM first passes through the WD many times on a wide orbit until the size of its orbit decays to become contained in the star. The timescale for this process is

$$\begin{aligned} t_1 &\sim \left( \frac{m_\chi}{m_{\text{ion}}} \right)^{3/2} \frac{R_{\text{WD}}}{v_{\text{esc}}} \frac{1}{\bar{N}_{\text{scat}}} \frac{1}{\max\{\bar{N}_{\text{scat}}, 1\}^{1/2}} \\ &\approx 7 \times 10^{16} \text{ s} \left( \frac{m_\chi}{10^{16} \text{ GeV}} \right)^{3/2} \left( \frac{\sigma_{\chi A}}{10^{-35} \text{ cm}^2} \right)^{-3/2}. \end{aligned} \quad (\text{E.12})$$

Subsequently, the DM completes many orbits within the star until dissipation further reduces the orbital size to the thermal radius. The timescale for this process is

$$\begin{aligned} t_2 &\sim \left( \frac{m_\chi}{m_{\text{ion}}} \right) \frac{1}{n_{\text{ion}} \sigma_{\chi A}} \frac{1}{v_{\text{ion}}} \\ &\approx 10^{14} \text{ s} \left( \frac{m_\chi}{10^{16} \text{ GeV}} \right) \left( \frac{\sigma_{\chi A}}{10^{-35} \text{ cm}^2} \right)^{-1}. \end{aligned} \quad (\text{E.13})$$

There is an additional  $\mathcal{O}(10)$  logarithmic enhancement of the timescale once the DM velocity has slowed below  $v_{\text{ion}}$ . Note that time to complete a single orbit is set by the gravitational free-fall timescale:

$$t_{\text{ff}} \sim \sqrt{\frac{1}{G \rho_{\text{WD}}}} \approx 0.5 \text{ s}. \quad (\text{E.14})$$

In the above description, we have assumed that the DM loses a negligible amount of energy during a single transit:

$$\frac{\sigma_{\chi A}}{m_\chi} \ll \frac{1}{\rho_{\text{WD}} R_{\text{WD}}}. \quad (\text{E.15})$$

This also ensures that the dynamics of DM within the star is that of Newtonian gravity along with a small drag force. In the opposite regime, the qualitative evolution of captured DM differs from the picture presented in detail below. In this case there is no stage of external orbital motion corresponding to  $t_1$ —DM will instead rapidly thermalize to a speed  $v_{\text{th}}$  after entering the star. The internal motion now proceeds as a gravitationally-biased random walk, with a net drift of DM towards the center of the star. For sufficiently large  $\sigma_{\chi A}$ , DM will collect at a radius  $r_c$  which is larger than  $r_{\text{th}}$  given above, due to a balance of gravity with outward Brownian diffusion. This may delay the onset of self-gravitation, possibly beyond  $\tau_{\text{WD}}$ , as we now require the collection of a larger mass  $\rho_{\text{WD}} r_c^3$ . It is important to note that the differences between the Brownian and orbital regimes are immaterial for constraints on the decay of captured DM (e.g., Fig. 4.11), which cares only about the quantity of DM present in the star. For annihilation constraints, however, the internal evolution of DM is quite important. For the largest unconstrained cross sections  $\sigma_{\chi A}$  (see Fig. 4.9), one can check that captured DM is distributed across a large fraction of the star due to Brownian motion and does not collapse. This DM population still yields a strong constraint on  $\sigma_{\chi\chi}$ , similar to but somewhat weaker than the constraints which can be placed on DM that undergoes self-gravitational collapse after capture (e.g., Fig. 4.10).

When Brownian motion is insignificant, the DM will begin steadily accumulating at  $R_{\text{th}}$  after a time  $t_1 + t_2$ . Once the collected mass of DM at the thermal radius exceeds the WD mass within this volume, there is the possibility of self-gravitational collapse. The time to collect a critical number  $N_{\text{sg}}$  of DM particles is

$$t_{\text{sg}} \sim \frac{N_{\text{sg}}}{\Gamma_{\text{cap}}} \sim \frac{\rho_{\text{WD}} R_{\text{th}}^3}{m_{\chi} \Gamma_{\text{cap}}} \approx 10^{10} \text{ s} \left( \frac{m_{\chi}}{10^{16} \text{ GeV}} \right)^{-1/2} \left( \frac{\sigma_{\chi A}}{10^{-35} \text{ cm}^2} \right)^{-1} \quad (\text{E.16})$$

Typically, the timescale for collapse is then set by the DM sphere's ability to cool and shed gravitational potential energy. This is initially just  $t_2$ , while the time to collapse at any given radius  $r$  decreases once the DM velocity rises again above  $v_{\text{ion}}$ :

$$t_{\text{cool}} \sim t_2 \min\{v_{\text{ion}}/v_{\chi}, 1\}, \quad v_{\chi} \sim \sqrt{\frac{GNm_{\chi}}{r}}, \quad (\text{E.17})$$

where  $N$  is the number of collapsing DM particles. Note that when  $m_{\chi} > 10^{21} \text{ GeV}$ , the number of particles necessary for self-gravitation  $N_{\text{sg}}$  as defined in (E.16) is less than 2. In this case we should formally take  $N_{\text{sg}} = 2$ .

Finally, there is a further subtlety that arises in the growing of DM cores for the large DM masses  $m_{\chi}$  of interest to us. The time  $t_{\text{sg}}$  to collect a self-gravitating number of particles decreases for larger DM masses. However, the dynamics of the collapse are set by the cooling time, which is initially  $t_{\text{cool}} \propto m_{\chi}$ . For  $m_{\chi} > 10^{15} \text{ GeV}$ , the collection time may be shorter than the cooling time  $t_{\text{sg}} < t_{\text{cool}}$  (depending on the cross section). In fact, the collection time may even be shorter than the dynamical time  $t_{\text{ff}}$ . If  $t_{\text{ff}} < t_{\text{sg}} < t_{\text{cool}}$ , the DM core will be driven to shrink because of the gravitational potential of the over-collecting DM. The timescale for the shrinking is set by the capture rate of DM. Ultimately, the collapsing DM

core will consist of  $N_{\text{sg}}$  enveloped in a “halo” of  $\Gamma_{\text{cap}} t_{\text{cool}} \gg N_{\text{sg}}$  particles, which will also proceed to collapse. If instead  $t_{\text{sg}} < t_{\text{ff}} < t_{\text{cool}}$ , the DM core will rapidly accumulate to this large number before dynamically adjusting. For the purpose of the collapse constraints on DM annihilation, if  $t_{\text{sg}} < t_{\text{cool}}$  we will simply assume a number of collapsing particles  $N = \Gamma_{\text{cap}} t_{\text{cool}}$ . This is the case for the constraints plotted in Fig. 4.10.